DTIC FILE COPY

AD-A219 503

NUSC Technical Report 8579
August 1989

Ambient Vertical Directional Spectra at a TOTO Near-Reef Site

R.M. Kennedy
Test and Evaluation Department
West Palm Beach, Florida

T.V. Goodnow
Sawgrass Technical Services, Inc.
Davie, Florida

Naval Underwater Systems Center
Newport, Rhode Island / New London, Connecticut

DTIC
ELECTE
MAR 19 1990
S D
E

*Original contains color plates: All DTIC reproductions will be in black and white.

Approved for public release; distribution is unlimited.

90 03 19 070

PREFACE

This report was prepared under project B64838 and 638V11, Principal Investigator Dr. R.M. Kennedy (Code 3802). The work reported herein was performed as part of the Naval Underwater Systems Center program of Independent Research and Independent Exploratory Development (IR/IED), Program Manager Dr. K.M. Lima (Code 10X), and the Test and Evaluation Department Acoustic Range Initiative, Program Manager J.H. Keegan (Code 38).

The Technical Reviewer for this report was Dr. W.M. Carey (Code 302).

Reviewed and Approved: August 1989

J.H. Keegan, Code 38
Head, Test and Evaluation Department

UNCLASSIFIED
SECURITY CLASSIFICATION OF THIS PAGE

REPORT DOCUMENTATION PAGE

1a. REPORT SECURITY CLASSIFICATION: Unclassified	1b. RESTRICTIVE MARKINGS
2a. SECURITY CLASSIFICATION AUTHORITY	3. DISTRIBUTION / AVAILABILITY OF REPORT: Approved for public release, distribution is unlimited.
2b. DECLASSIFICATION / DOWNGRADING SCHEDULE	
4. PERFORMING ORGANIZATION REPORT NUMBER(S): TR 8579	5. MONITORING ORGANIZATION REPORT NUMBER(S)
6a. NAME OF PERFORMING ORGANIZATION: Naval Underwater Systems Center Detachment; 6b. OFFICE SYMBOL (If applicable): 3802	7a. NAME OF MONITORING ORGANIZATION
6c. ADDRESS (City, State, and ZIP Code): West Palm Beach, FL 33402	7b. ADDRESS (City, State, and ZIP Code)
8a. NAME OF FUNDING / SPONSORING ORGANIZATION: Naval Underwater Systems Center; 8b. OFFICE SYMBOL (If applicable): 38	9. PROCUREMENT INSTRUMENT IDENTIFICATION NUMBER
8c. ADDRESS (City, State, and ZIP Code): Newport, RI 02841	10. SOURCE OF FUNDING NUMBERS: PROGRAM ELEMENT NO. / PROJECT NO. 638V11 / TASK NO. / WORK UNIT ACCESSION NO

11. TITLE (Include Security Classification): Ambient Vertical Directional Spectra at a TOTO Near-Reef Site

12. PERSONAL AUTHOR(S): Kennedy, R.M., Goodnow, T.V.

13a. TYPE OF REPORT	13b. TIME COVERED	14. DATE OF REPORT (Year, Month, Day)	15. PAGE COUNT
Final	FROM _____ TO _____	1989 August	92

16. SUPPLEMENTARY NOTATION

17. COSATI CODES		
FIELD	GROUP	SUB-GROUP
17	01	

18. SUBJECT TERMS (Continue on reverse if necessary and identify by block number): Underwater Acoustics, Acoustic [illegible], Vibration [illegible], Models, [illegible]

19. ABSTRACT (Continue on reverse if necessary and identify by block number)

See reverse side.

20. DISTRIBUTION / AVAILABILITY OF ABSTRACT: ☒ UNCLASSIFIED/UNLIMITED ☐ SAME AS RPT ☐ DTIC USERS	21. ABSTRACT SECURITY CLASSIFICATION: Unclassified
22a. NAME OF RESPONSIBLE INDIVIDUAL: R.M. Kennedy	22b. TELEPHONE (Include Area Code): (407) 832-8566; 22c. OFFICE SYMBOL: 3802

DD FORM 1473, 84 MAR — 83 APR edition may be used until exhausted. All other editions are obsolete.

SECURITY CLASSIFICATION OF THIS PAGE
UNCLASSIFIED

19. ABSTRACT

This report documents the data processing techniques and the results of the initial deployment of a wideband (40 to 4000 Hz) vertical acoustic antenna system in the The Tongue of the Ocean, The Bahamas, at a site adjacent to the Andros Island eastern escarpment. The instrumentation system consisted of seven octavely nested four-wavelength acoustic antennas covering the above frequency range and a VCR-based subsurface recording system that carried out a programmed sequence of recordings. This report documents a description of the experiment and its results. The purpose of the experiment was the initial field test of a deployable acoustic monitoring system (DAMS). The success of the experiment made available a data set that allowed the examination of the vertical spatial structure of the acoustic ambient of the location. While there were aspects of the data unique to the location, the bulk of the information appears to apply to the more-generic problem of characterizing the directional spectra resulting from a sea surface sound source structure.

TABLE OF CONTENTS

Accession For
NTIS GRA&I
DTIC TAB
Unannounced
Justification
By
Distribution/
Availability Codes
Avail and/or
Dist Special
A-1

Original contains color plates: All DTIC reproductions will be in black and white.

QUALITY INSPECTED 4

LIST OF ILLUSTRATIONS

LIST OF ILLUSTRATIONS (Cont'd)

LIST OF ILLUSTRATIONS (Cont'd)

LIST OF TABLES

1.0 INTRODUCTION

This report documents the findings of an experiment which placed a wide-band (40 to 4000 Hz) set of vertical acoustic antennas in The Tongue of the Ocean (TOTO) at a site adjacent to the Andros Island eastern escarpment. This report details the instrumentation and data processing procedures and documents the findings of a general analysis. The purpose of the experiment was the initial field test of a deployable acoustic monitoring system (DAMS) capable of autonomous remote operation. The success of the experiment made available a data set that allowed the examination of the vertical space-time second-order statistics of the underwater acoustic ambient in an area of interest to the Navy. The range of wind speeds (2 to 16 m/s) was large enough during the experiment period (September-October 1988) to draw statistical conclusions relative to the acoustic ambient of the area with particular emphasis on the "sea surface sound" that dominates the data. The 25 data sets examined represent approximately semidiurnal samples of the environment. The primary objectives of this report are (1) to document the wind speed dependence of the sound pressure level autospectral density and the acoustic vertical directional spectra, (2) to identify the lower bounds for the anisotropic gains that would be realized by vertical acoustic antennas operating in the area, and (3) to report on the industry-caused acoustic radiation monitored during the experiment. A secondary objective is to document some system aspects of the initial deployment of the DAMS.

The next section of the report provides all of the fundamental hardware, software, and environmental data required to interpret the results. That is followed by a section that notes some specific system self-noise limitations to the end product noted on the first deployment of the system. The fourth section covers the results of the measurement, and the final section summarizes the entire project.

2.0 EXPERIMENT DESCRIPTION

2.1 IN-WATER HARDWARE

A figure describing the deployable acoustic monitoring system is given in figure 1 which illustrates the components of the DAMS. The heart of the system is the acoustic module; it houses the seven acoustic antennas that cover a frequency range of 40 to 4000 Hz. Directly above the acoustic module is an engineering module that houses signal processing units and two array tilt sensors. Above and below these two units are vibration isolation modules (VIMs) that isolate the acoustic module from longitudinal vibrations induced into the system. A 30-m double-armored steel cable above the upper VIM serves as an electrical channel for the acoustic signals, array power, and array tilt signals to the instrumented pressure vessel (IPV) which is inside a syntactic foam collar that keeps the entire system oriented vertically. A depth sensor is located in the IPV. The cable below the system is connected to a variable-depth, bottom-moored system.

The acoustic sensor system consists of seven octavely coalesced four-wavelength acoustic line antennas covering the frequency range of 40 to 4000 Hz. The 14-bit hydrophone signals from each antenna section are transmitted, one antenna at a time, to a subsurface data logger (IPV) that synchronously records them digitally on video cassette recorders (VCRs) along with array tilt and depth information as well as the date and time. A system controller is programmed for a wide selection of on/off times. There is enough VCR tape and battery life for a 60-day deployment of alternate-day samples.

Acoustic antenna details pertinent to this report are given in table 1. In all cases the apertures are four wavelengths wide at the design frequency.

The array is bottom moored and maintained at nearly a constant depth. Two depths were used in the measurement period: 156 m and 140 m, as measured at the IPV. Currents would tilt the system and thus increase this depth. The

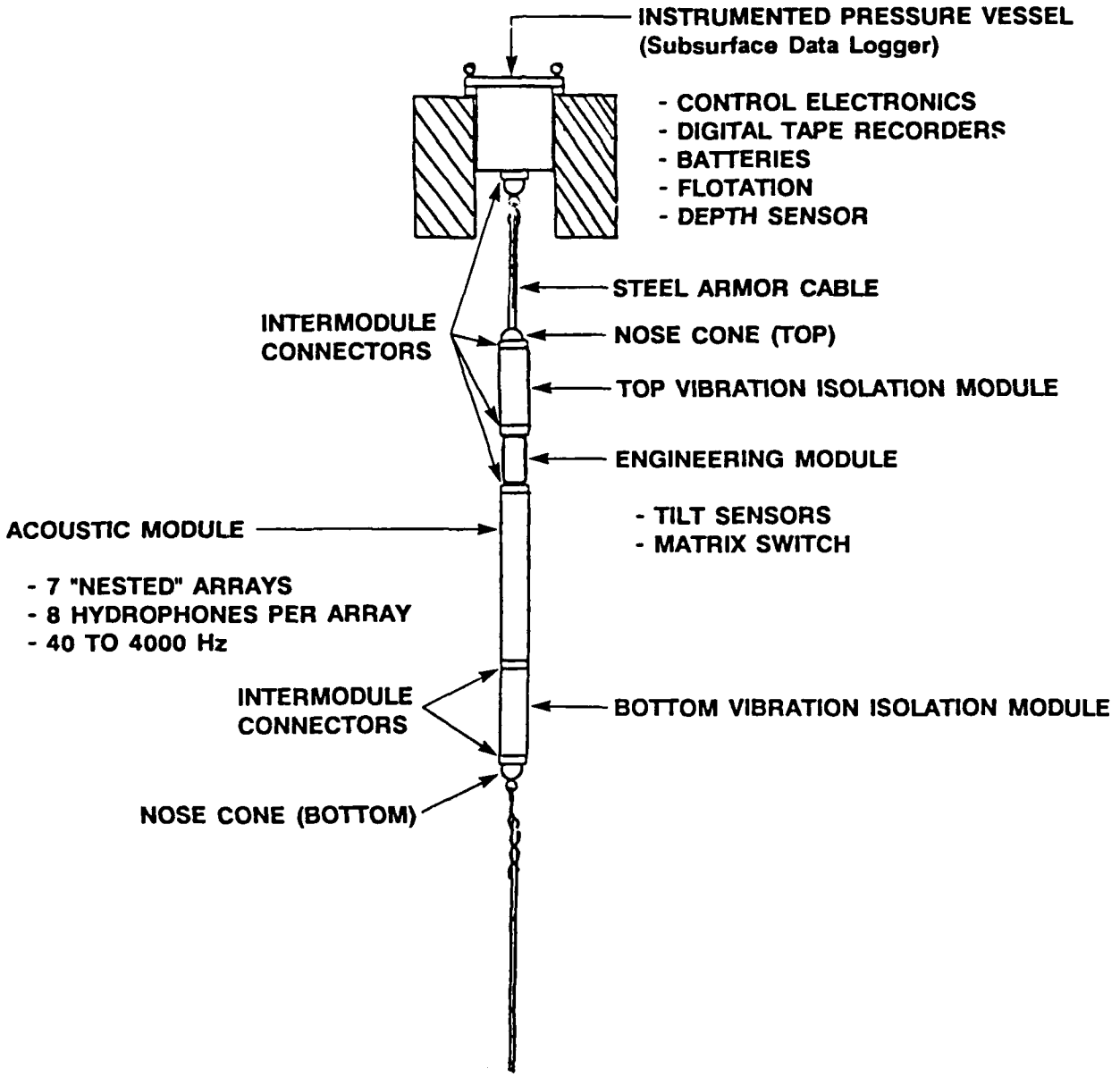

Figure 1. Components of the Deployable Acoustic Monitor System

Table 1. Acoustic Antenna Details

Acoustic Array Section	Design Frequency (Hz)	Line Array Length (m)	Hydrophone Uniform Separation (m)	Number of Hydrophones
1	5624*	0.93	0.133	8
2	2812	1.8	0.267	8
3	1406	3.73	0.533	8
4	703	7.47	1.067	8
5	351	14.94	2.134	8
6	176	29.87	4.267	8
7	88	59.74	8.534	8

*Note that the data recording system limited the upper frequency to 4000 Hz.

typical ranges of depths were 156 to 159 m and 139 to 147 m. The center of the acoustic aperture was 60 m deeper than these depths. The array tilt frequency of occurrence, i.e., histogram, is presented in figure 2. The figure illustrates that while tilt angles were as high as 8 degrees the much more probable occurrence was for the array to be within 3 degrees of vertical. A vertically uniform current can be inferred from these results using the methods developed for the hydrodynamics of cables. For example, see reference 1. The relation between current and array tilt is also shown in figure 2, indicating that the current rarely exceeded 0.5 knots.

2.2 DATA PROCESSING

The data processing system is shown as a data flow diagram in figure 3. The typical 3-minute, eight-hydrophone (32 Mbyte) space-time series coming from the VCR tape playback in real time is acquired by an array processor in

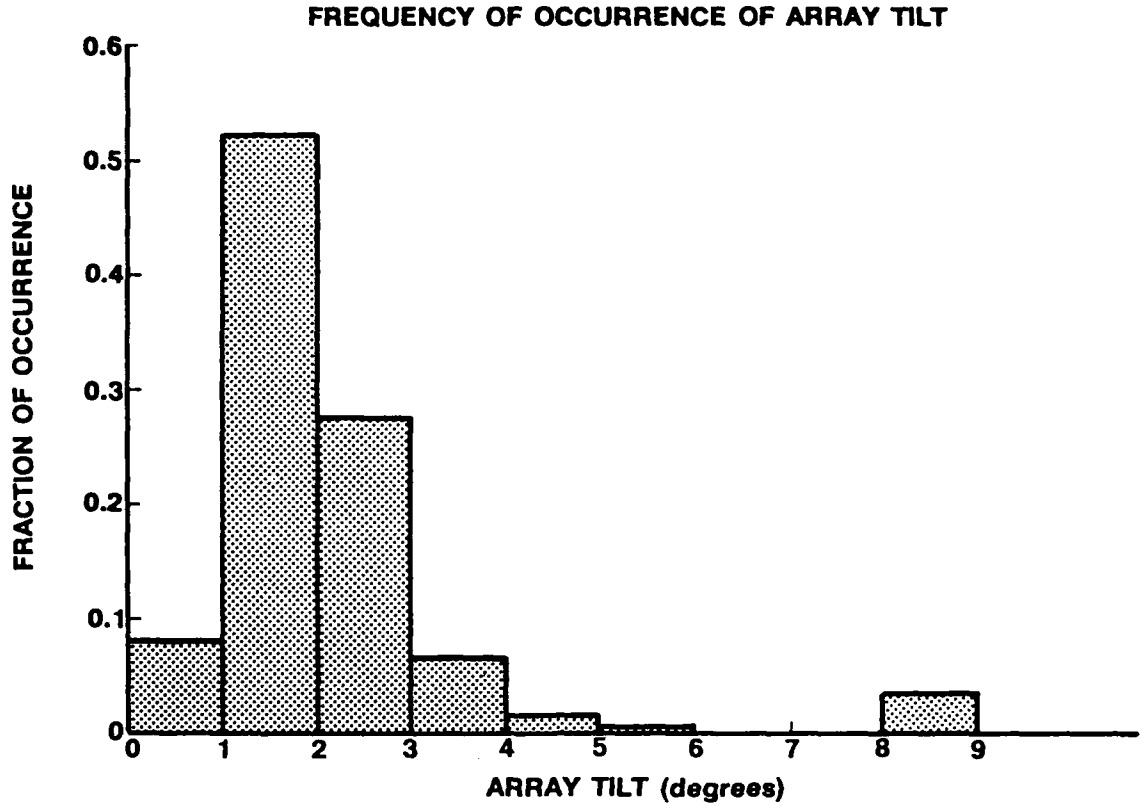

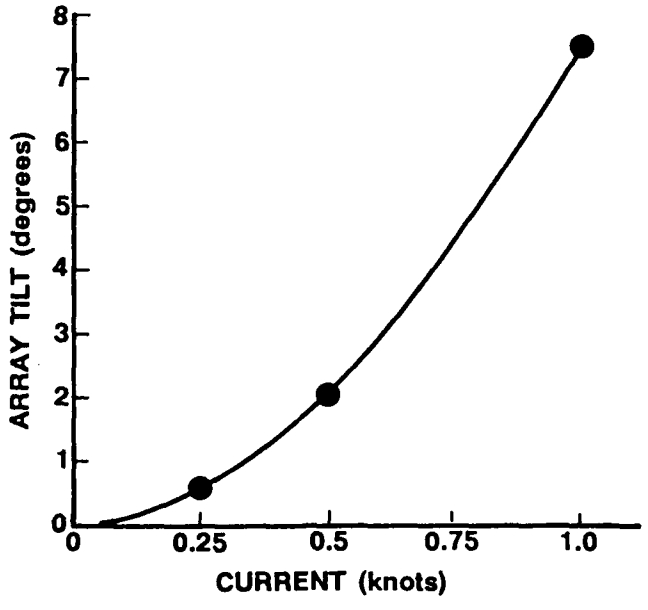

Figure 2. Array Tilt Measurements

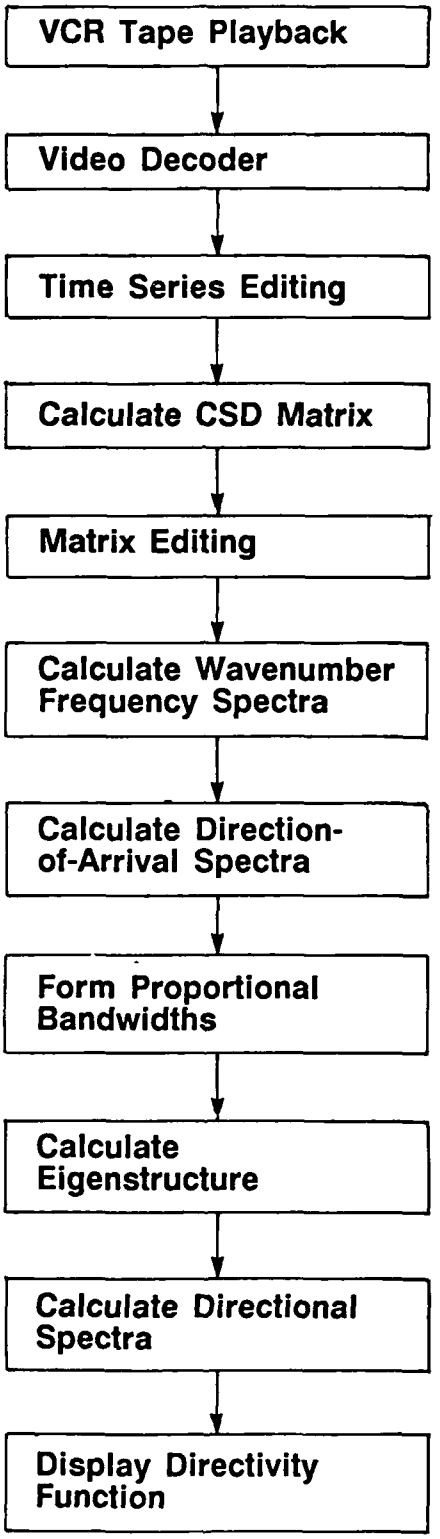

Figure 3. Data Processing Flow Diagram

"real" time. The individual time series resident in the array processor are checked for nonstationarities, i.e., trends and "wild" points, and edited as appropriate. The cross-spectral density function is estimated for each possible hydrophone pair. We refer to this ensemble of cross-spectral density functions as the cross-spectral density (csd) matrix. The csd matrix is the measurement's fundamental statistical description. The data acquisition system records all time series using a 9790.2 Hz sampling frequency, independent of the acoustic aperture. The spectral analysis system digitally low-pass filters and decimates each of the space-time series according to its aperture so as to optimize the spectral resolution for the fixed-point (1024) fast Fourier transform (FFT) size. Table 2 lists the filter cutoff frequency (at 3 dB) and the frequency resolution for each acoustic antenna. The spectral resolution accounts for the 1.63 spreading factor associated with the "Hann" temporal window used with all the data. The cross-spectral density function between the nth and mth hydrophone is estimated by using the relation

$$S_p\left(\xi_{nm},\omega\right) = \frac{\Delta t}{M} \sum_{j=1}^{M} X_{nj}(\omega) X_{mj}(\omega) \quad , \tag{1}$$

where $X_{nj}(\omega)$ and $X_{mj}(\omega)$ are the jth realization of the Fourier transforms of the nth and mth hydrophones, ω is the angular frequency, M is the number of transforms averaged, and ξ_{nm} is the spatial separation between the nth and mth hydrophones. Only nonoverlapping transforms are used. The actual number of FFTs used in each average varies with the acoustic aperture, the length of the time series, and the VCR tape operations. The typical number of transforms for the 3-minute recording time for each of the apertures is listed in table 3. This table also summarizes the 95% confidence interval for the spectral estimates in each of the acoustic apertures. From a statistical sampling perspective the estimates are quite good.

Table 2. Spectral Analysis Details

Acoustic Aperture Number	Design Frequency (Hz)	Cutoff Frequency (Hz)	Frequency Resolution (Hz)
1	5624	4000*	9.6
2	2812	3944	9.6
3	1406	1972	4.8
4	703	1000	2.4
5	352	500	1.2
6	176	250	0.6
7	88	140	0.3

*Limitation imposed by data recording system.

Table 3. Spectral Analysis 95% Confidence Interval Summary (based on a typical 3-minute data acquire)

Acoustic Aperture Number	Typical Number of FFTs	Effective Degrees of Freedom	Total Confidence Interval (dB)
1	1540	4928	0.4
2	1710	5472	0.4
3	850	2720	0.4
4	430	1376	0.6
5	210	672	1.0
6	100	320	1.4
7	50	160	1.8

After the csd matrix is calculated, the spatial homogeneity of the measurements is verified by checking that the csd values along any diagonal of the matrix are not different from each other in a statistical sense. The statistical uniformity of the matrix diagonals is a result of the acoustic antennas having uniformly spaced hydrophones in a homogeneous pressure field. A matrix with this property is termed a Toeplitz matrix. All csd matrices calculated from a real field variable have complex symmetry about the major diagonal. A matrix having this symmetry is called a Hermetian matrix. Occasionally in the experiment the Toeplitz property was not found to be true in aperture 7, the low frequency aperture, and in those cases the offending hydrophones were omitted from the analysis. This point will be discussed in more detail in the next section. Missing elements of the matrix caused by omitted hydrophone data are filled using the Toeplitz property when the offending hydrophone is "within" the matrix. If the hydrophone is an "end" hydrophone, calculations are made with the aperture shortened by a single hydrophone spacing rather than by attempting extrapolation. Throughout the experiment the seventh hydrophone (hydrophone 31) in the lowest frequency antenna (aperture 7) was nonfunctioning and its csd locations were filled as discussed above. This process is identified in figure 3 as "matrix editing."

The next step in figure 3 is the calculation of a wavenumber-frequency spectra from the measured csd matrix. The wavenumber-frequency spectra is estimated using a modified form of the Blackman-Tukey algorithm,[2] which implements the wavenumber spectra by taking a Fourier transform of the spatial correlation function present in the csd matrix. The modification accounts for the complex-number nature of the csd matrix elements in place of the real-valued time series samples of reference 2. The algorithm, which uses the Hermetian symmetry of the csd matrix and employs Hamming spatial weighting, is

$$S_p(k_q,\omega) = 0.23\ V(k_{q-1},\omega) + 0.54\ V(k_q,\omega) + 0.23\ V(k_{q+1},\omega) \quad , \tag{2}$$

where

$$V(k_q,\omega) = d\left\{\overline{S_p^2(o,\omega)} + 2\sum_{r=1}^{N-2} \mathrm{Re}\left[\overline{S_p^2(rd,\omega)}\cos\left(\frac{rq\pi}{N}\right)\right] + \mathrm{Re}\left[\overline{S_p^2\left[(N-1)d,\omega\right]}\cos(r\pi)\right]\right\} ,$$

$k_q = \frac{2\pi}{Nd} q$ (wavenumber),

d is the interhydrophone spacing, and

$\overline{S_p^2(\ )}$ is the diagonally averaged csd element.

Note that the wavenumber is the line array longitudinal wavenumber. Results of these calculations are discussed in the next section.

The next step in figure 3 is the calculation of the direction of arrival spectra (DOAS), which is the standard beamformer output autospectral density. While the csd matrix calculation is the fundamental statistical quantity of the experiment, the DOAS is the fundamental observation of the experiment because there is no illuminating way to view a csd matrix. The DOAS on the other hand is a familiar and intuitive quantity in the study of underwater acoustics. It is calculated by finding the weighted quadratic form of the csd matrix as follows

$$S_b\left(\omega;\phi_s\right) = \frac{\underset{\sim}{D}^T\left(\phi_s\right)\ \underset{\sim}{S}_p(\omega)\underset{\sim}{D}^*\left(\phi_s\right)}{Q} , \qquad (3)$$

where

$$\underset{\sim}{D}\left(\phi_s\right) = \begin{bmatrix} w_1 \\ w_2 \exp\left[i\frac{\omega}{c}d\cos\phi_s\right] \\ . \\ . \\ . \\ w_N \exp\left[i\frac{\omega}{c}(N-1)d\cos\phi_s\right] \end{bmatrix}$$

$\underset{\sim}{S}_p(\omega)$ is the N×N csd matrix,

ϕ_s is the "steered" elevation angle with zero degrees being straight up, and

w_N is the real spatial weight applied to the nth hydrophone.

$$Q = \left(\sum_{n=1}^{N} w_n\right)^2$$

A Taylor pattern function was designed for the experiment.[3,4] The spatial weights for the eight-element hydrophone array are given in table 4. The beam pattern functions are shown in figures 4 and 5 for antenna nondimensional apertures of 2 and 4, with the latter being the "design" frequency. The half-power beamwidths for the steering angles in the figures are given in table 5. Note from the figures that the Taylor pattern has nearly equal side lobes 19 dB below the mainlobe.

Table 4. Taylor Spatial Weights

Hydrophone Number	Spatial Weight
1	0.7274
2	0.9086
3	1.1147
4	1.2493
5	1.2493
6	1.1147
7	0.9086
8	0.7274

Table 5. Taylor Pattern Half-Power Beamwidths

Steering Direction (Degrees)	Nondimensional Aperture (Degrees)	
	"2"	"4"
0	83.8	58.0
45	46.0	20.5
90	28.7	14.2

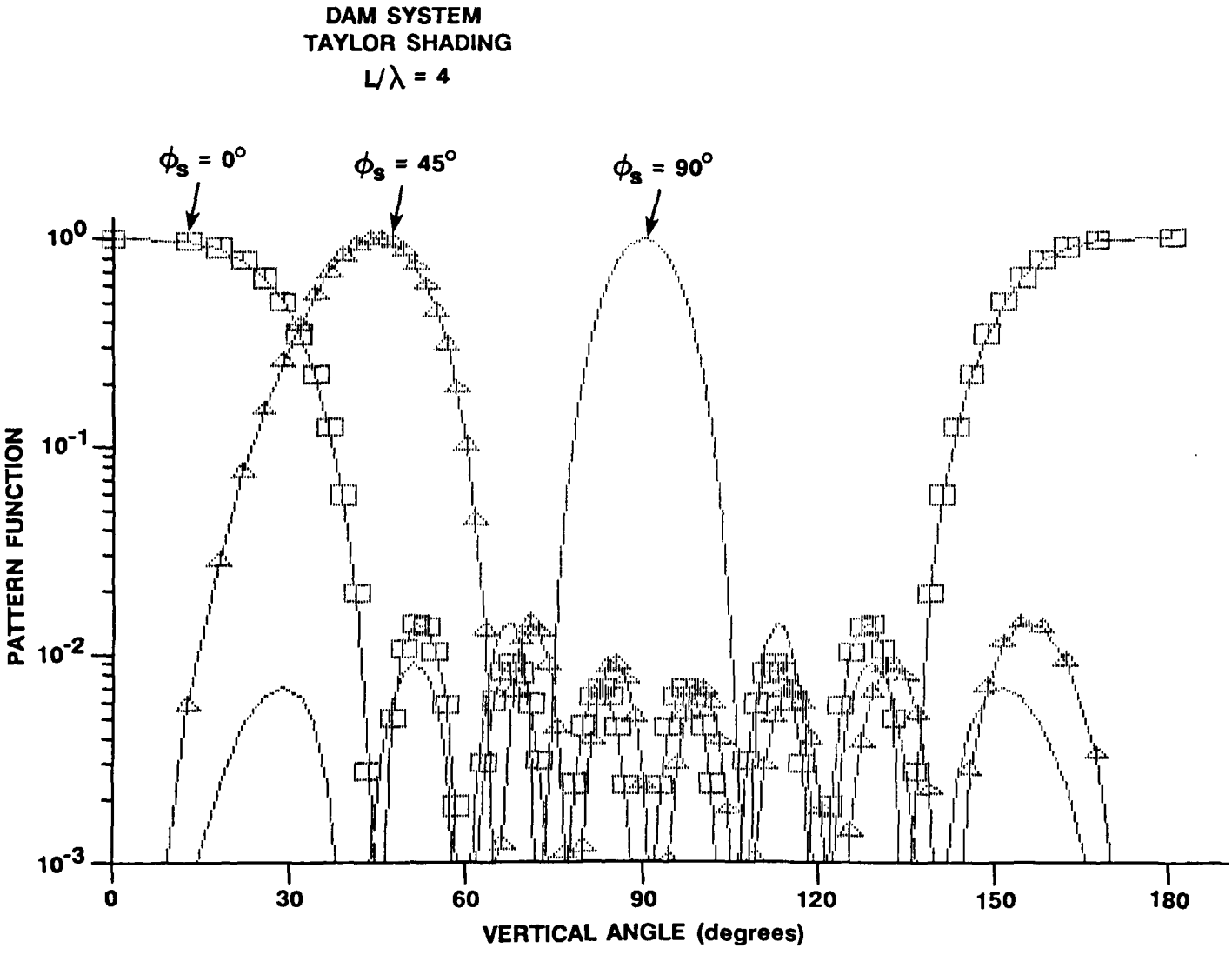

Figure 4. Beam Patterns at the Design Frequency

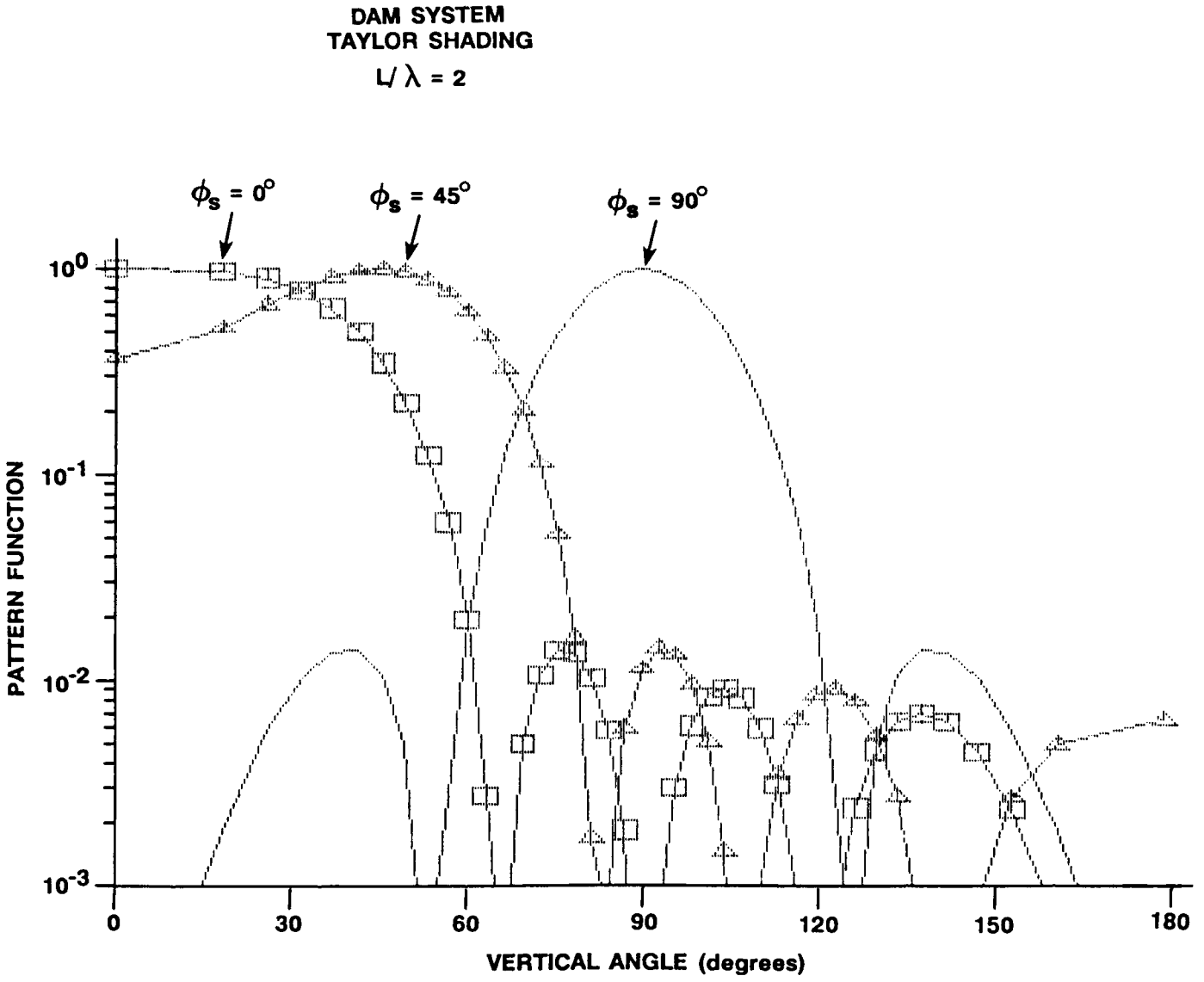

Figure 5. Beam Patterns at Half the Design Frequency

The next step in the data flow of figure 3 is the formation of proportional bandwidth spectra. There are two reasons for wanting to form proportional bandwidths. First is a reduction in data. Second is an increase in the statistical stability of the csd estimates. The first reason is the more compelling one. There are over 2×10^5 complex words resulting from a single acquire of all seven antennas. Much of the data is redundant because the physical mechanisms governing the process do not change rapidly with frequency. The relatively high-resolution constant-bandwidth analysis oversamples the process when this is the case. Thus the csd matrix can be averaged over blocks of frequency with large reductions in the amount of data storage required and with an improvement in the quality of the statistical estimates. Because the data need to be archived and sorted with respect to environmental parameters, principally wind speed, there is significant motivation to reduce the amount of data that must be sorted. Thus we formed proportional-bandwidth csd matrices. The bandwidth choice was arbitrary because these bandwidths are synthesized from the raw data. One-third-octave bandwidths were synthesized for both historical reasons, i.e., the prevalence of one-third-octave analysis in the acoustic industry, and because the one-third-octave analysis still appears to over-sample the process we are measuring.

The next step in figure 3 is the eigenstructure decomposition of the csd matrix.[5] This analysis was undertaken with two objectives in mind. First, this approach readily leads to the identification of plane-wave interference in the ambient data.[6] The next section of this report discusses an extension to this whereby the technique is used to remove a contaminating interference source. Second, the results of the decomposition are useful in interpreting certain aspects of the data.

The "solution" to the eigenstructure problem is well known[7] and requires solving the linear algebraic equation

$$\underset{\sim}{S}_p(\omega)\underset{\sim}{H}(\omega) = \underset{\sim}{H}(\omega)\underset{\sim}{\Lambda}(\omega) \quad , \tag{4}$$

where

$\underset{\sim}{H}(\omega)$ is the 1×N matrix of column (N-element) eigenvectors of $\underset{\sim}{S}_p(\omega)$, and

$\underset{\sim}{\Lambda}(\omega)$ is the N×N diagonal matrix of eigenvalues $[\lambda(\omega)]$ of $S_p(\omega)$.

The reason for finding the eigenvectors and eigenvalues is that they represent a decomposition of the csd matrix into a complete set of linearly independent components.[8] The decomposition is explicitly expressed as

$$\underset{\sim}{S}_p(\omega) = \sum_{n=1}^{N} \lambda_n(\omega) \underset{\sim}{H}_n \overset{*T}{\underset{\sim}{H}}_n(\omega) \quad , \tag{5}$$

where λ_n is the nth scalar eigenvalue and $H_n(\omega)$ is the nth N-element eigenvector. It will be instructive to take the DOAS of both sides of equation (5) by applying equation (3). This leads to a decomposition of equation (3) into "eigenbeams", which are defined as

$$E_n(\omega) = \lambda_n \frac{\underset{\sim}{D}^T(\phi_s) \underset{\sim}{H}_n \overset{*T}{\underset{\sim}{H}}_n(\omega) \underset{\sim}{D}^*(\phi_s)}{Q} \quad . \tag{6}$$

The final step shown in figure 3 is the calculation of the vertical directional spectra from the measured csd matrix. Much has been written about estimating the directivity spectra from measurements made on linear hydrophone arrays. The difficulty is that both the beamformer outputs and the cross-spectral densities are related to the directivity spectra by an integral equation in which the directivity spectra is in the integrand. Inverting this integral equation has basic uniqueness difficulties when using beamformer output autospectral density.[5,10] In the case of making the estimate directly from the csd matrix, an assumption that the field is composed of statistically independent plane waves is necessary.[11,12] This assumption may not be a good

one when significant energy is being reflected from the ocean bottom. Deep-ocean application of these techniques has been made.[11,13,14] A first-order approximation to the directivity function can be obtained by normalizing each beamformer output by its solid-angle coverage.[6,15,16] More specifically, the DOAS may be expressed in terms of the beamformer pattern function and the desired directional spectra as

$$S_b\left(\omega;\phi_s\right) = 2\pi \int_0^{\pi} d\phi \sin\phi \; B^2\left(\phi;\phi_s\right) N^2(\phi) \quad , \tag{7}$$

where $B^2(\phi;\phi_s$ is the beamformer pattern function, assuming azimuthal symmetry, and $N^2(\phi)$ is the vertical directional spectra.

If the directional spectra varies slowly relative to the beam pattern mainlobe width, equation (7) can be approximated by

$$S_b\left(\omega;\phi_s\right) \simeq B^2\left(\phi;\phi_s\right) N^2\left(\phi_s\right) \Delta\psi\left(\phi_s\right) \quad , \tag{8}$$

where $\Delta\psi(\phi_s)$ is the solid-angle coverage of the beamformer mainlobe, which is evaluated using

$$\Delta\psi\left(\phi_s\right) = 2\pi \int_{\phi_s-\phi_-}^{\phi_s+\phi_+} d\phi \sin\phi \quad , \tag{9}$$

where ϕ_- and ϕ_+ are the half-power angles associated with steering angle ϕ_s. The first-order approximation is realized by solving for $N^2(\phi)$ in equation (8).

This first-order approach yields reasonably accurate results for most values of the elevation angle when the acoustic field results from a spatially diffuse source structure. The exception to this is near the horizontal direction where significant curvature is possible.

2.3 EXPERIMENT ENVIRONMENT

Figure 6 illustrates the measurement location relative to the adjacent escarpment, including the local bathymetry.[17] The measurement site is on the eastern shore of Andros Island in The Bahamas just south of Fresh Creek, as shown in figure 7. The depth at the measurement site is 700 meters (383 fathoms), which is on the sloping bottom shown in figure 7.

The experiment took place in September and October 1988. The near-surface sound velocity-depth profiles, typical of that location and season, are shown in figure 8. The two profiles were measured coincident with acoustic measurements. The important acoustic characteristics of the profiles are (1) the sound velocity at the measurement depth is always less than the surface velocity, and (2) the measurement depth is always below the seasonal thermocline depth, which varied from 30 to 73 meters. There are two consequences to the first characteristic. First, near-surface sound sources contribute no energy to the directional spectra at angles of less than 9 degrees from the horizontal. Second, the near-surface sound sources that contribute to the measured sound field are limited to a circular area with an approximate radius of 1300 meters. This limited area of influence is shown in figure 6. The second characteristic indicates that the measurements never include "surface duct" effects.

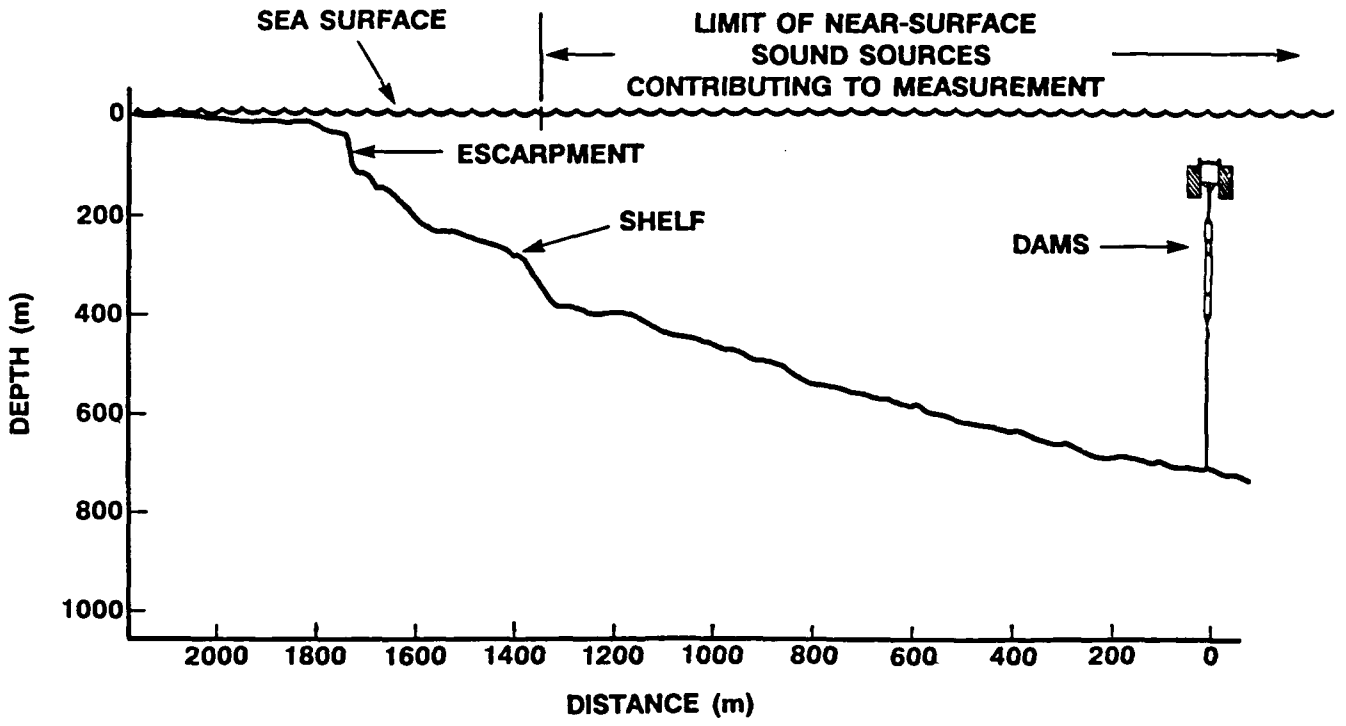

Figure 6. Measurement Location

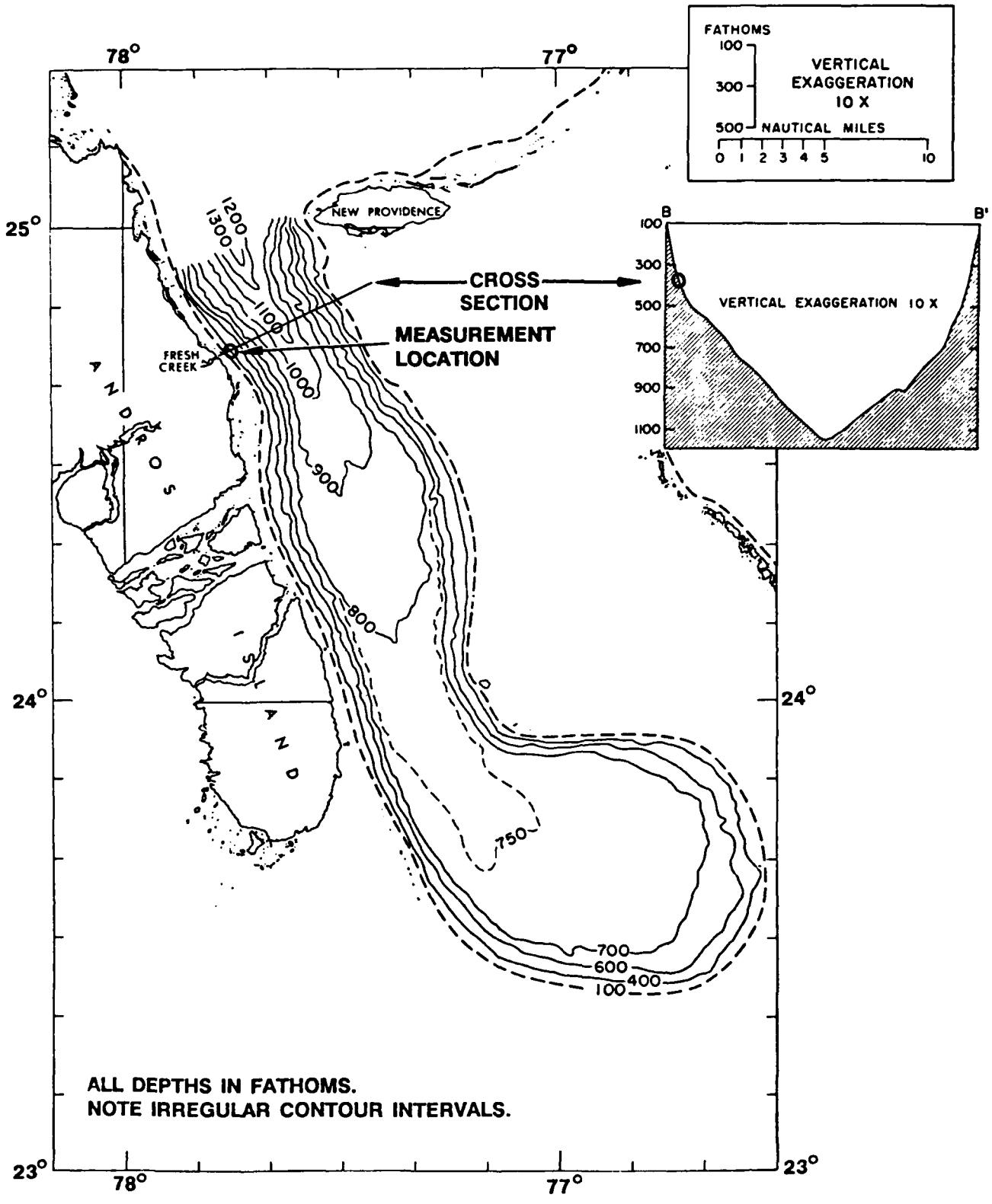

Figure 7. Measurement Location Bathymetry

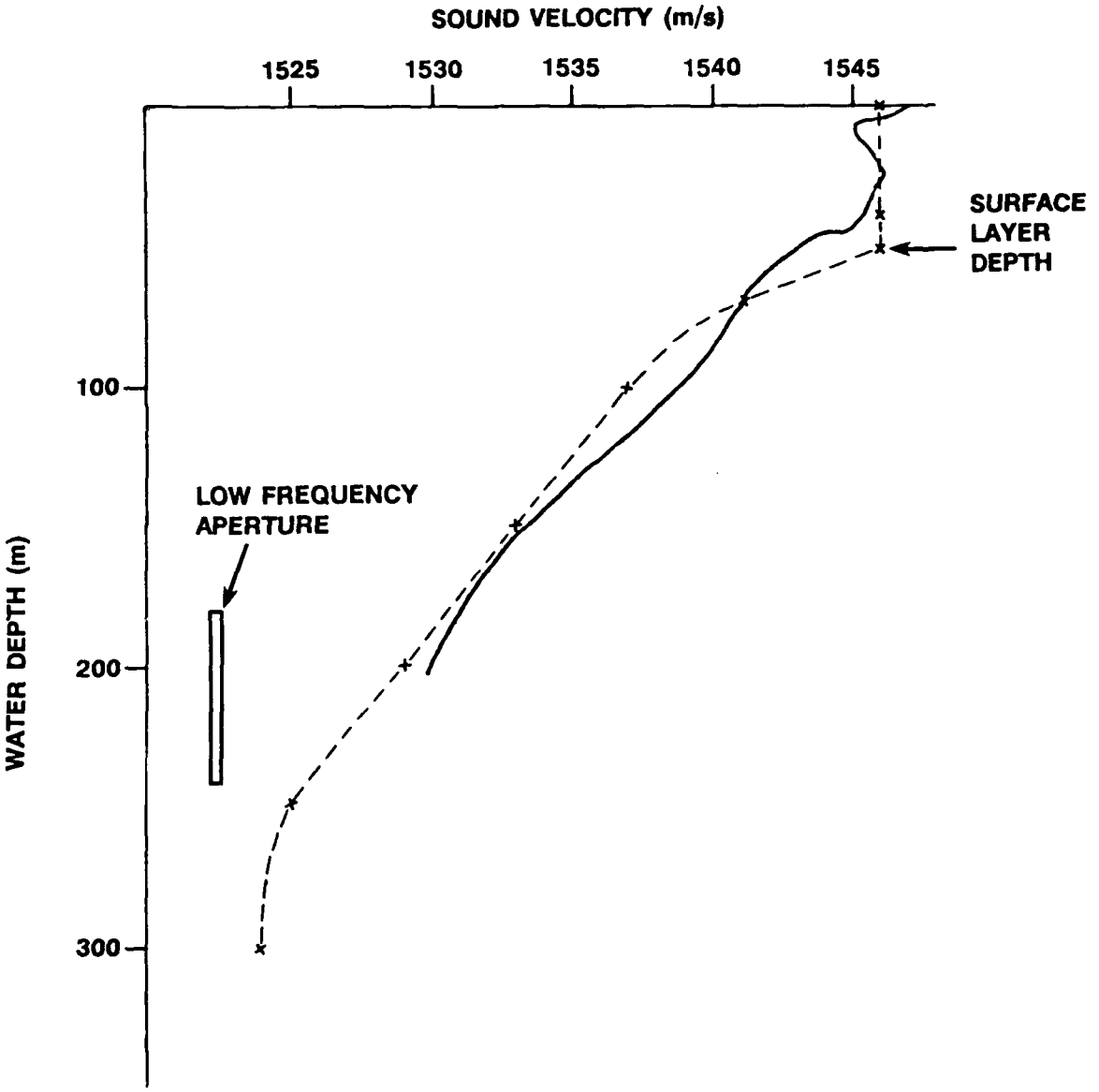

Figure 8. Sound Velocity-Depth Profiles

3.0 SYSTEM SELF-NOISE

This report documents the initial deployment of the DAMS. NUSC experience with such vertical hydrophone array structures is limited. The purpose of this section is to document structural and electronic problems found in this deployment. The analysis of the data indicated three sources of system self-noise, i.e., hydrophone response due to nonacoustic signals caused by the measurement system. These three sources of contamination are (1) common-mode electronic noise generated by the IPV, (2) hydroacoustic noise caused by the antenna structure interacting with ocean currents, and (3) preamplifier electronic noise.

The term "common-mode noise" is used to describe a system electronic noise that occurs in all hydrophone channels with no difference in phase. When such a noise enters a beamforming algorithm it adds coherently in the "broadside" steered direction, which in this case is an elevation angle of 90°. Figure 9, which shows the direction-of-arrival spectra for the quietest acoustic ambient condition observed, illustrates the common-mode noise problem. The 2 m/s wind speed condition shown in figure 9 contains the lowest acoustic levels of the experiment and thus best illustrates the self-noise problem. At higher wind speeds the acoustic signal increases and partially masks the self-noise. Figure 9 depicts, in an elevation angle-frequency space, the portion of the direction-of-arrival spectra contaminated by the noise. Figure 10, which shows the autospectral density of the beamformer output steered to an elevation angle of 90°, gives another view of the problem.

The common-mode noise problem was found to originate in the instrumented pressure vessel (IPV) electronics. The battery supply voltage was used as an input to a dc-to-dc converter and voltage regulation subsystem. One of the outputs of the voltage regulation system was a 12-volt line that drove the VCRs as well as the the hydrophone array and matrix switch electronics. The recorders periodically "pulled down" this supply voltage. This periodic signal, or more exactly a harmonic of that signal which occurred in the passband of the system, appeared on the hydrophone output signals. This problem has

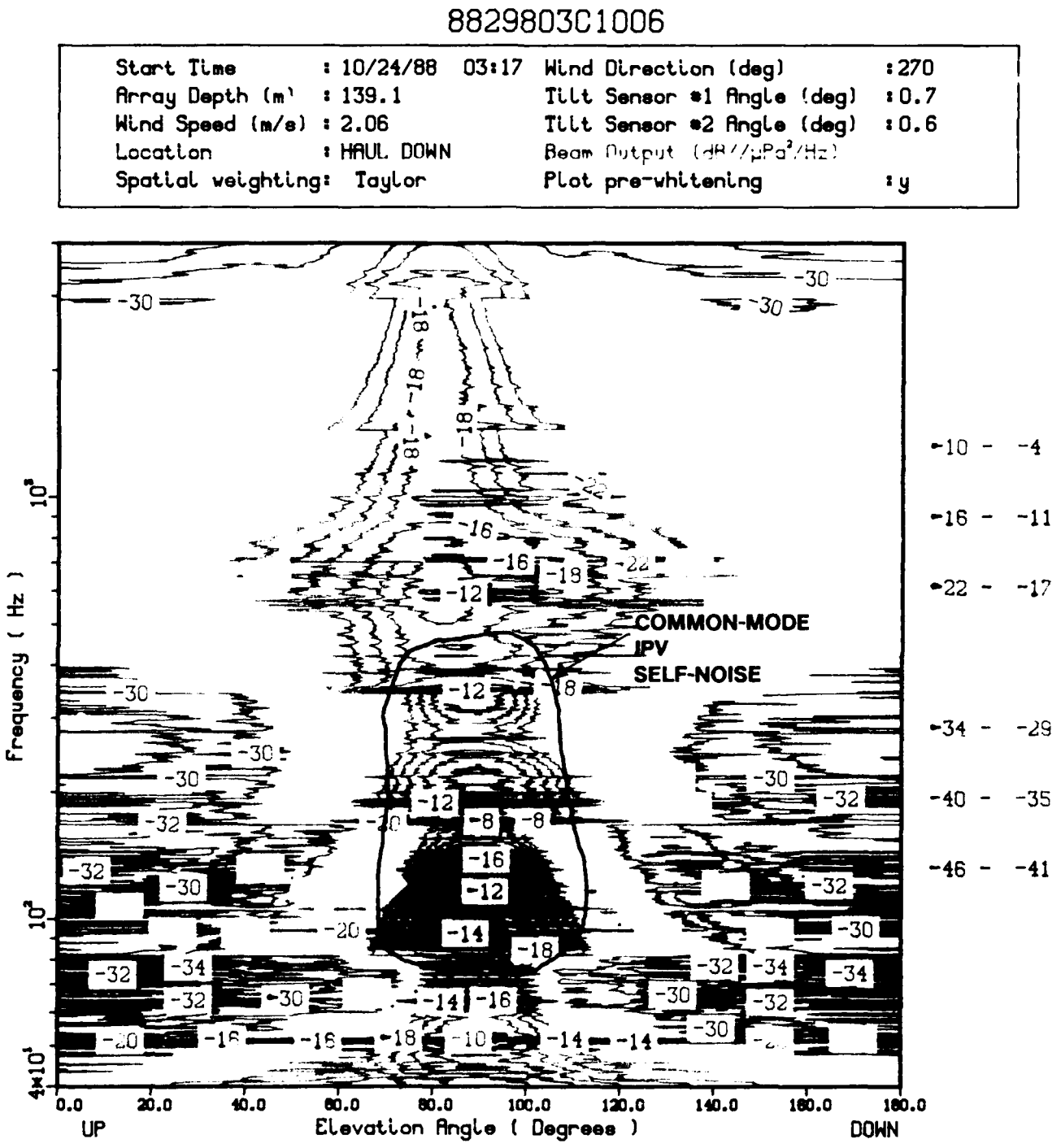

Figure 9. Direction-of-Arrival Spectra Illustrating Common-Mode Noise Problem

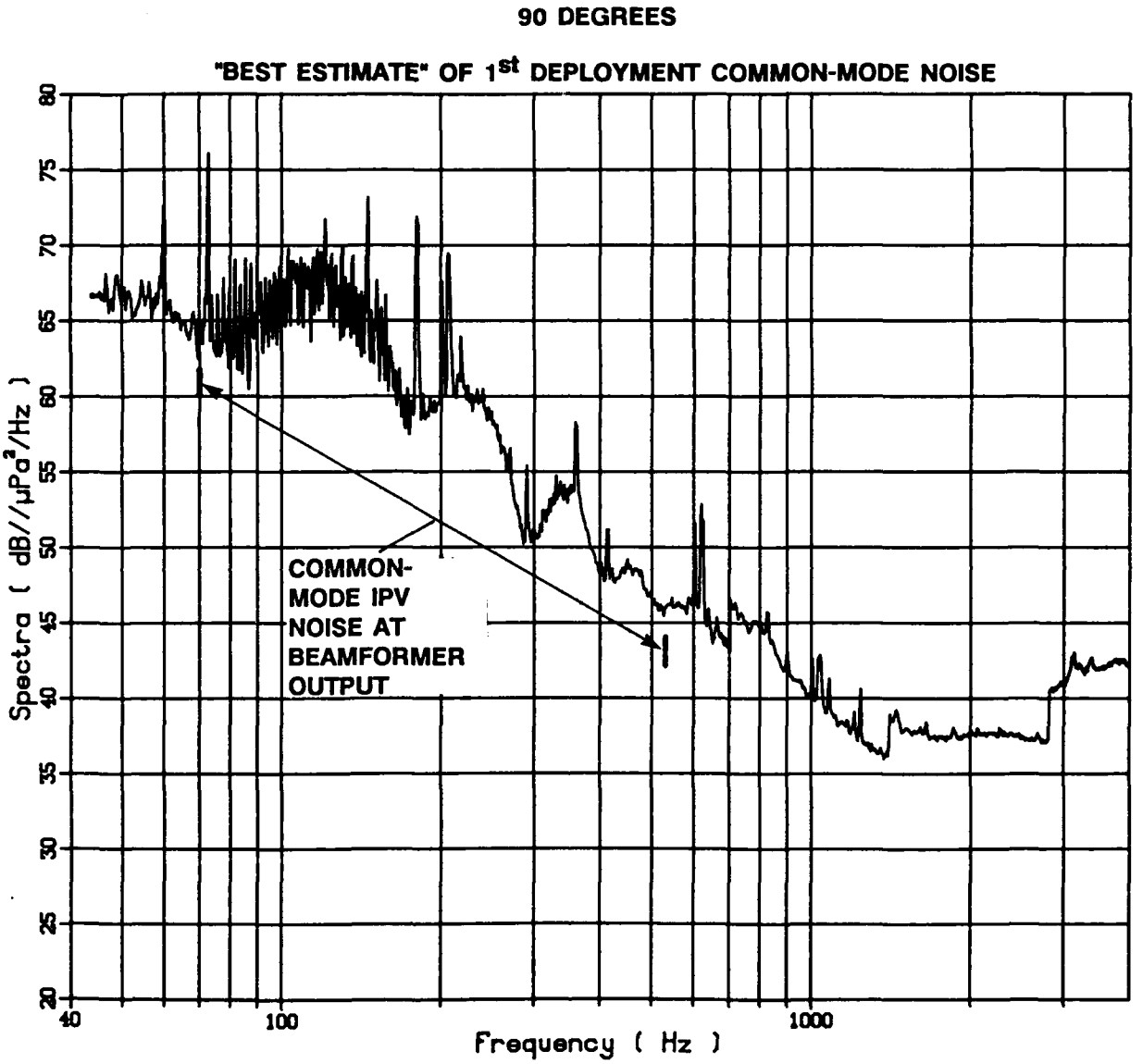

Figure 10. Broadside Beam Output Illustrating Common-Mode Noise Problem

since been corrected by including a second dc-to-dc converter in the IPV to service just the VCRs.

It is clear from the data that the structure was undergoing forced vibration at certain times. Those vibrations manifested themselves as very low frequency signals. Typically those signals were limited to the two end hydrophones, i.e., hydrophones number 1 and 32, which are 46 cm from the acoustic module end terminations. Those low frequency signals normally were not observed on hydrophones 2 through 30, which are hydrophones removed from the module end terminations. (Hydrophone 31 was nonfunctional.) Each of those hydrophones is in excess of 9 meters from a module end termination. It is known that this type of structure has a resonant axisymmetric transverse wave that propagates longitudinally along the structure at about 35 m/s. The hydrophones nearest to the module ends are thus less than one-half wavelength away from the ends at frequencies less than 40 Hz while at the same frequency the next hydrophones are several wavelengths away. This structural wave is damped by the hosewall material loss tangent and is significantly damped within a couple of wavelengths. Furthermore, those waves are efficiently generated by impedance discontinuities in the hosewall such as occur at module end terminations. We thus surmise that such structural waves are generated at the acoustic module ends and are observed in the end hydrophones but are not seen on the next hydrophones because of structural damping. This cannot be directly measured because the same wave must be measured by at least one hydrophone pair. There were other times when all of the hydrophones in the array appeared to have significant low frequency signals that were presumably vibration induced. Unfortunately, when this condition was present the signals were large enough that an electronic overload in the IPV occurred and definitive analysis of the characteristic of the vibration could not be made.

Overload protection in the form of spectral equalization incorporated in the original design took the form of a single-pole high-pass filter section in the IPV with a "corner" frequency of 40 Hz.[1] In nearly all of the data obtained from this deployment it was seen that this protection was inadequate. Figure 11 is a contour plot of the wavenumber-frequency spectra (equation (2)) of a typical experimental trial at low frequency. The wavenumber-frequency

882542170002

Start Time	: 09/10/88 21:50	Wind Direction (deg)	:081
Array Depth (m)	: 156.0	Tilt Sensor #1 Angle (deg)	:0.2
Wind Speed (m/s)	: 8.0	Tilt Sensor #2 Angle (deg)	:0.2
Location	: HAUL DOWN	Sensor Spacing (m)	: 8.534
Spatial weighting:	Hamming	Plot pre-whitening	:y

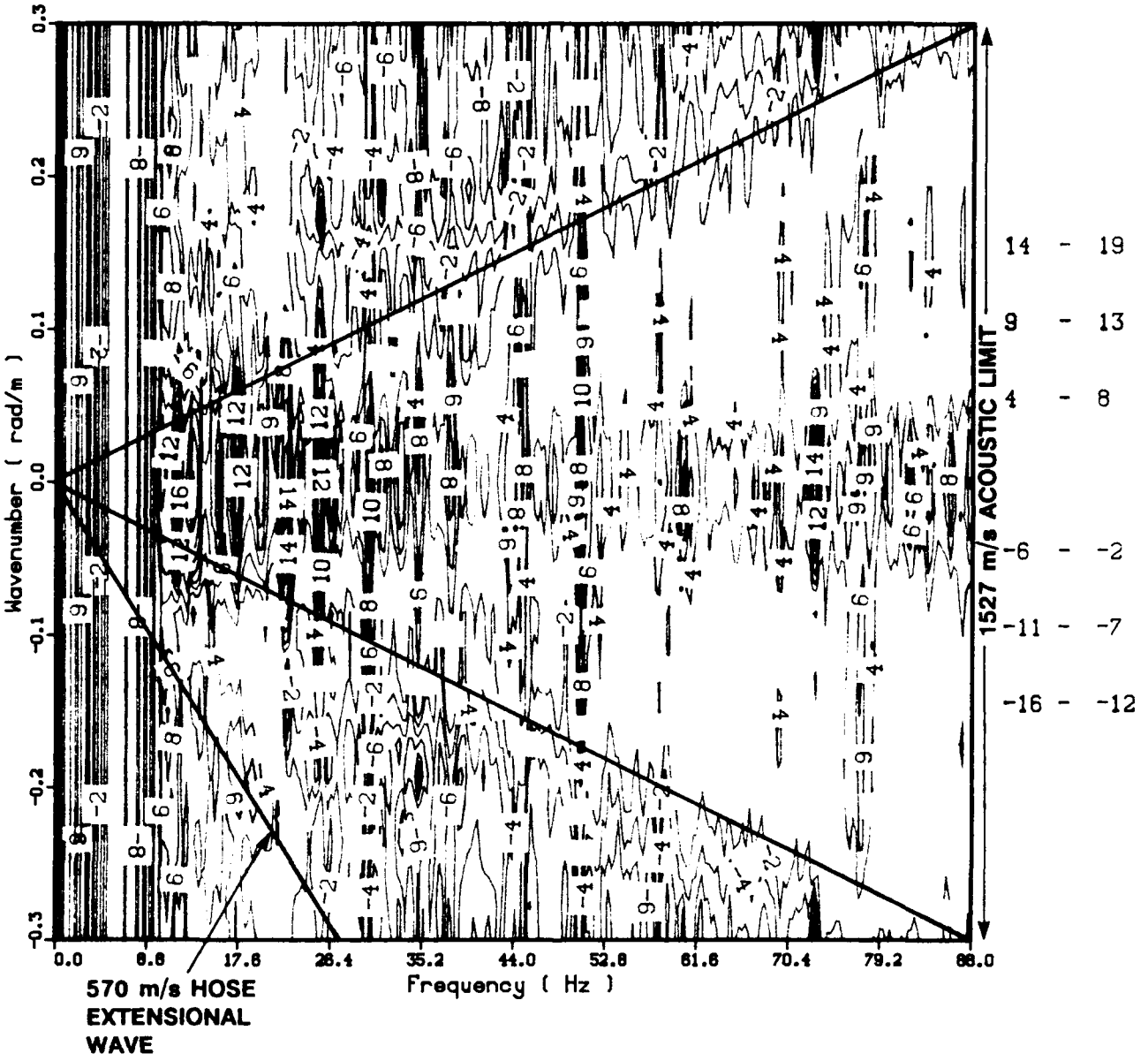

Figure 11. Aperture 7 Wavenumber-Frequency Spectra Illustrating Subsonic Data Contamination

spectra is used to separate the sonic and subsonic contributions to the hydrophone outputs. The limits of the "sonic cone" are shown as lines superimposed on the figure using the velocity at the face of the array from figure 8. The figure shows that all of the energy above 25 Hz is acoustic. Below 25 Hz significant subsonic energy appears although the sonic levels are higher than the subsonic levels. The character of the subsonic energy is further discussed below.

One can only speculate on the source of the structural vibration, but a likely candidate is vortex/wake-induced strumming of the structure caused by ocean currents.[1] Using the ocean current values inferred from figure 2, one can note that the vibration signals were infrequently present when the current was less than 1 to 3 knots. A particular value of array tilt was not a perfect predictor of the existence of a vibration-induced signal with a current less than 1 to 2 knots. However, if the current exceeded 1 to 2 knots, then vibration signals were always present, and all of the data were overloaded if the current exceeded 2 to 3 knots.

It is useful in the design of a vertical array to know whether structural strumming outside the actual acoustic aperture is contributing nonacoustic signals. In this discussion "outside the acoustic aperture" refers to the structure above and below the upper and lower VIMs shown in figure 1. If that portion of the structure is generating significant vibration, it would be necessary for the system to propagate that energy as a longitudinal extensional wave because transverse vibrational waves in water are rather highly damped by the fluid. The passage of longitudinal waves through the acoustic structure would be observed by the hydrophones because with the longitudinal strength member in the wall, the hosewall would couple a pressure wave to the hydrophones by the hosewall Poisson effects.[1] This is probably the source of the 570 m/s wave (marked on figure 11) observed at 17 Hz, which is the frequency for which the module is two extensional waves long. The frequency resonance seen in the figure is thus the modal response of the structure to the extensional wave. The existence of a well-defined wave speed was not typical, but the increase in subsonic energy below 20 to 25 Hz was always the case. In reference 1 the role of VIMs as a low-pass filter to longitudinal vibration was

discussed and the "corner" frequency of that passband was calculated to be 23 Hz. A better design would have had the extensional two-wavelength resonance above the VIM cutoff. The conclusions drawn from these observations are that (1) no significant nonacoustic energy is present in the measurement band of 40 to 4000 Hz, (2) there is measurable subsonic energy below the passband of the VIMs, i.e., 25 Hz, (3) the data indicate quite significant sonic levels at least down to 5 Hz, and (4) the single-pole high-pass filter in the IPV is not adequate, by itself, to prevent low frequency sonic and subsonic energy from occasionally overloading the IPV electronics. Additional equalization is available and is recommended.

A complete discussion of the preamplifier noise contribution is found in reference 1. It was anticipated that preamplifier noise could be a limiting factor for wind speeds near 0 knots. In the present data the lowest wind speed case was 4 knots, which produced recording levels approximately 6 dB above the preamplifier noise contribution. The beamformer output data at angles below the horizontal are shown, in this report, to have relatively low acoustic sound pressure levels as a consequence of the source being near the surface which required a bottom reflection to arrive at angles below the horizontal. Figure 12 illustrates the beamformer output steered "straight down" for the lowest wind speed data recorded, i.e., 4 knots. Superimposed on the measured data are calculations of the preamplifier noise contribution to the beamformer output. As pointed out in reference 1, these values can be considered an upper bound as the measured points typically fell about 3 dB lower than the calculated values. A measured point is also shown in the figure. Comparison of these two curves at high frequency shows that preamplifier noise is contaminating the data.

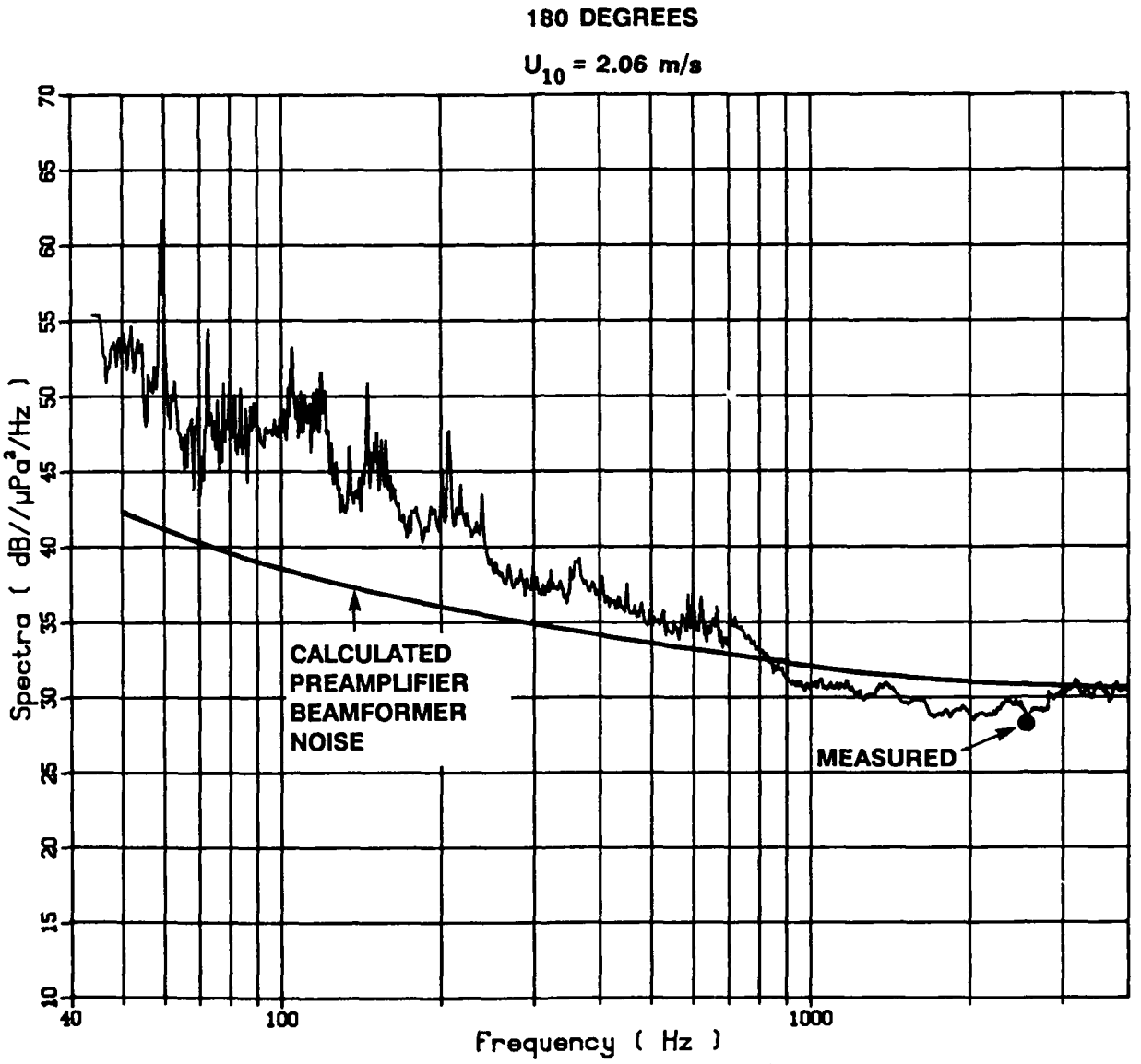

Figure 12. Lowes+ Beamformer Output Levels Measured Compared With Calculatec Preamplifier Noise at Beamformer Output

4.0 EXPERIMENT RESULTS

4.1 TOTAL SOUND PRESSURE LEVEL

While the intent of this experiment was to measure the directional spectra, the omnidirectional sound pressure level was found and compared with historical results. The hydrophones used had no significant directional pattern at the highest frequency of the measurements, so the major diagonal terms of the csd matrix were the autospectral density of the total field sound pressure level. The average of the major diagonal terms was found at each frequency of interest. The results for a selection of frequencies are shown in figure 13, displayed as functions of the logarithm of wind speed. The lowest frequency shown is 634 Hz because the data at lower frequencies than that were frequently contaminated by acoustic sources, to be discussed, that are not related to wind speed. Superimposed on this plot are data points taken from the Caron-Sheffield memorandum[18] which is an extensive data base of total acoustic sound pressure levels for the area. As expected, the agreement with the Caron-Sheffield data is good.

In figure 14 the hydrophone sound pressure level data are replotted as functions of nondimensional friction velocity, i.e., surface friction velocity nondimensionalized by the minimum phase speed of the capillary-gravity wave. This approach is identical to that discussed by Kerman, 1984, and the algorithms used here are the same as found in reference 19. The traditional wisdom is that a value of 1 for this nondimensional variable represents incipient whitecapping. Each of the data sets is partitioned into "whitecaps present" (wp) and "whitecaps not present" (wnp) according to whether the nondimensional friction velocity is greater or less than 1, respectively. A regression line is fit to each partition. The data base is quite limited for the wp case and no power law exponent can be reliably reported. Qualitatively one can only report that the wp case appears to have a much lower dependence on the friction velocity, as has previously been reported.[19] The wnp case has a larger data representation, and a power law exponent was found for each frequency. The values of the exponents found varied randomly from 1.4 to 2.2,

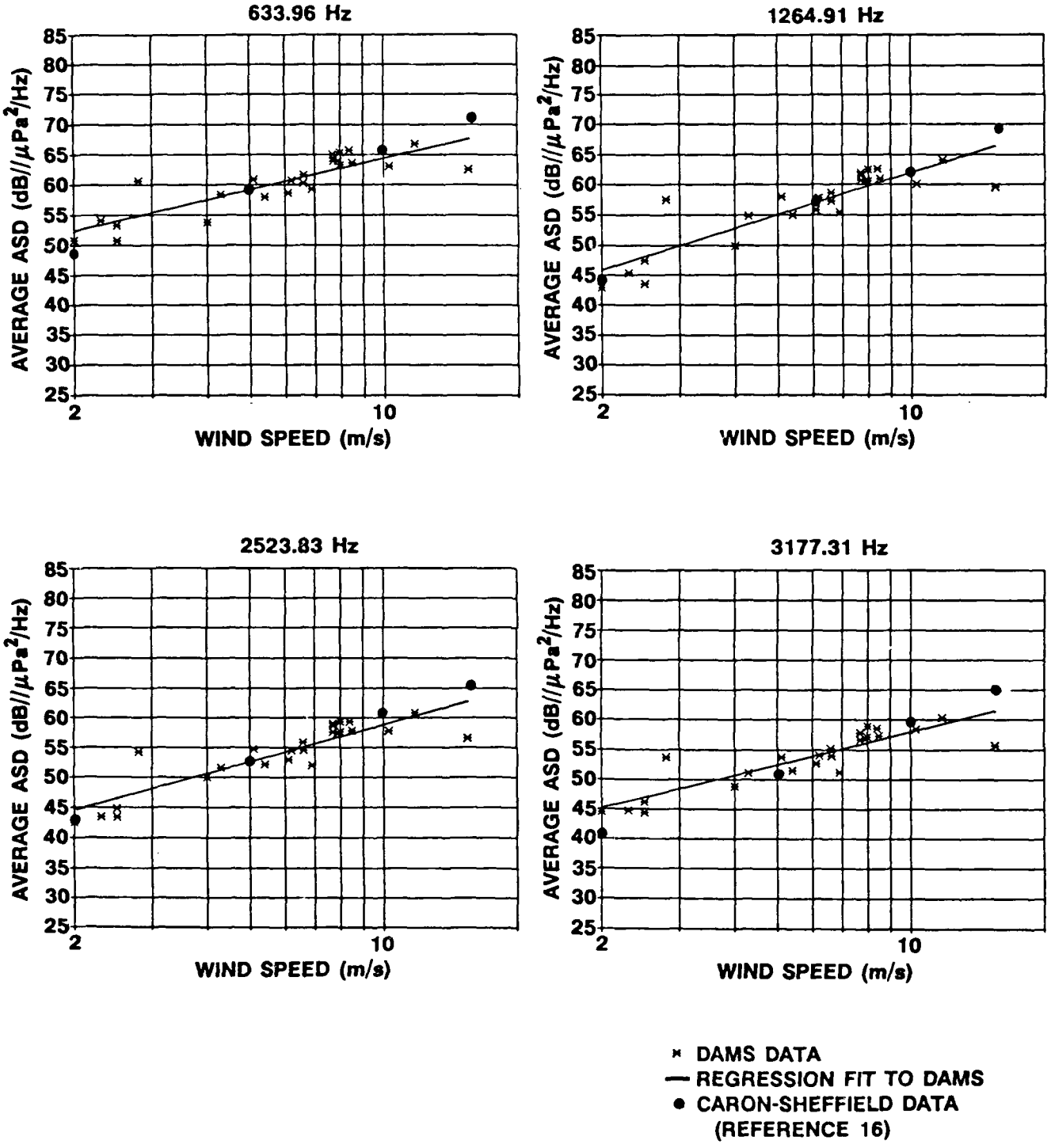

Figure 13. Comparison of Autospectral Density With Historical Data

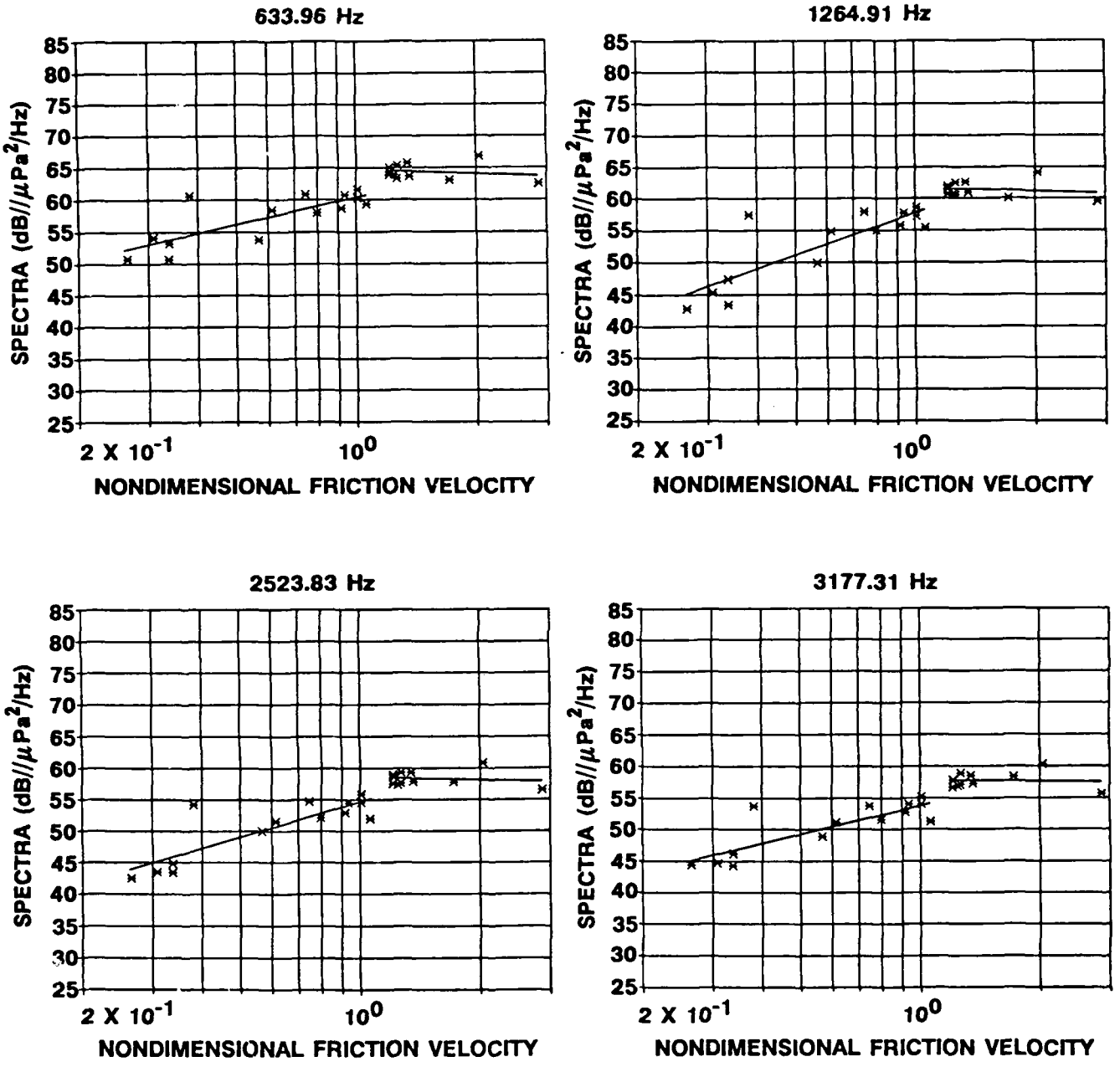

Figure 14. Hydrophone Autospectral Density Dependence on Nondimensional Friction Velocity

with an average value of 1.7. This is lower than the 3.0 value reported by Kerman,[19] for reasons to be discussed.

4.2 DIRECTION-OF-ARRIVAL SPECTRA (DOAS)

The most complete view of the results of a particular trial is the elevation angle-frequency DOAS. The frequency range of 40 to 4000 Hz is covered with seven nested antennas. Thus the multidimensional spectra consists of a composite of the results of the seven apertures. An example of such a surface is shown in figure 15. Only the upper octave of each acoustic aperture is included in the presentation. The figure contains both a surface plot of the spectra and a pseudo-colored contour plot of the spectra. Comprehending the numerous details of the data set requires comparing both views of the three-dimensional spectra surface. The latter is frequency "prewhitened" to reduce the dynamic range of the plot. The "prewhitening" is accomplished by integrating the surface with respect to the elevation angle at each frequency. A third-order regression curve is fit to the results of the integral, and the resulting polynomial is then used to "whiten" the surface.

A spectra similar to figure 15 is available for each of the 25 data sets. While each multidimensional spectra has certain unique characteristics, they all fall into a couple of categories, examples of which are shown in figures 15 through 18. Figure 15 illustrates three characteristics common to all data. First, the six peaks occurring in the downward-looking direction, i.e., 180°, are the aliasing lobes occurring whenever the hydrophone spacing is exactly one-half wavelength. Second, the "hump" of energy centered on 90° around 100 Hz is the common-mode noise discussed in section 3. Third, at the frequencies at which aliasing first occurs there is a discontinuity in the spectral level associated with the change in aperture. When the distribution of energy in an angular direction is larger than the spatial resolution of the beamformer, the spectra level of the beamformer will increase as the frequency decreases because the beamwidth of the aperture increases. At the demarcation between apertures the beamwidth changes abruptly from a four-wavelength antenna to a two-wavelength antenna with a subsequent 3 dB drop in spectra level. This phenomena is better observed in figure 19, which is an elevation

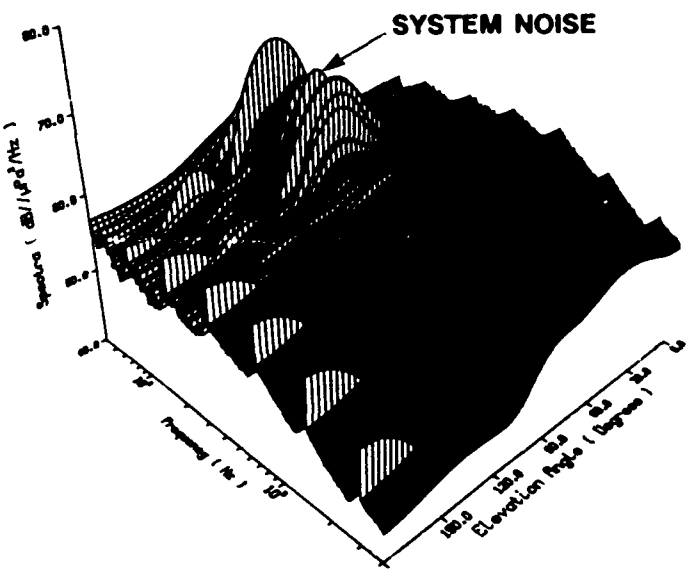

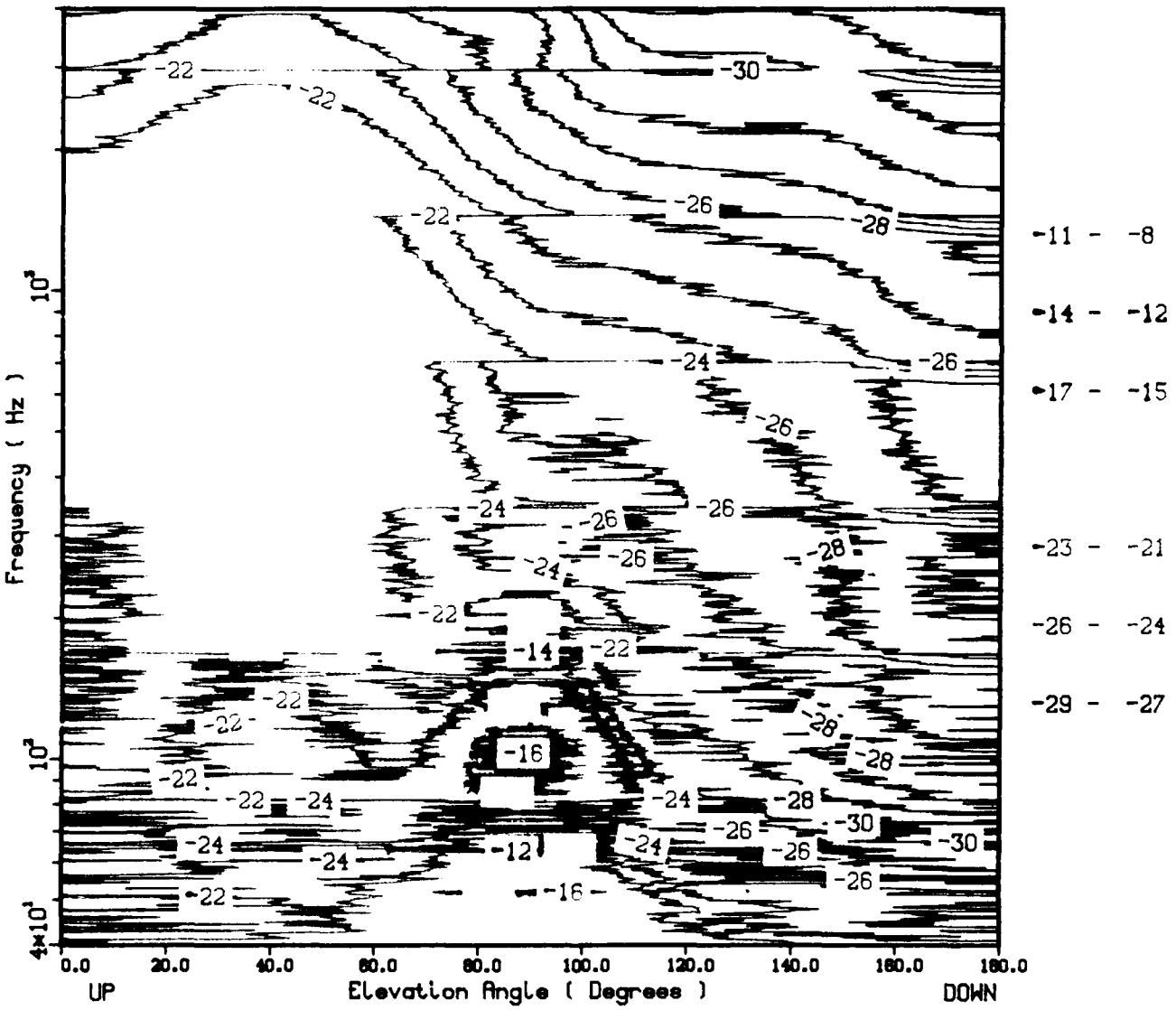

Figure 15. Composite Narrowband Elevation Angle-Frequency Spectra, 11.83 m/s Wind Speed

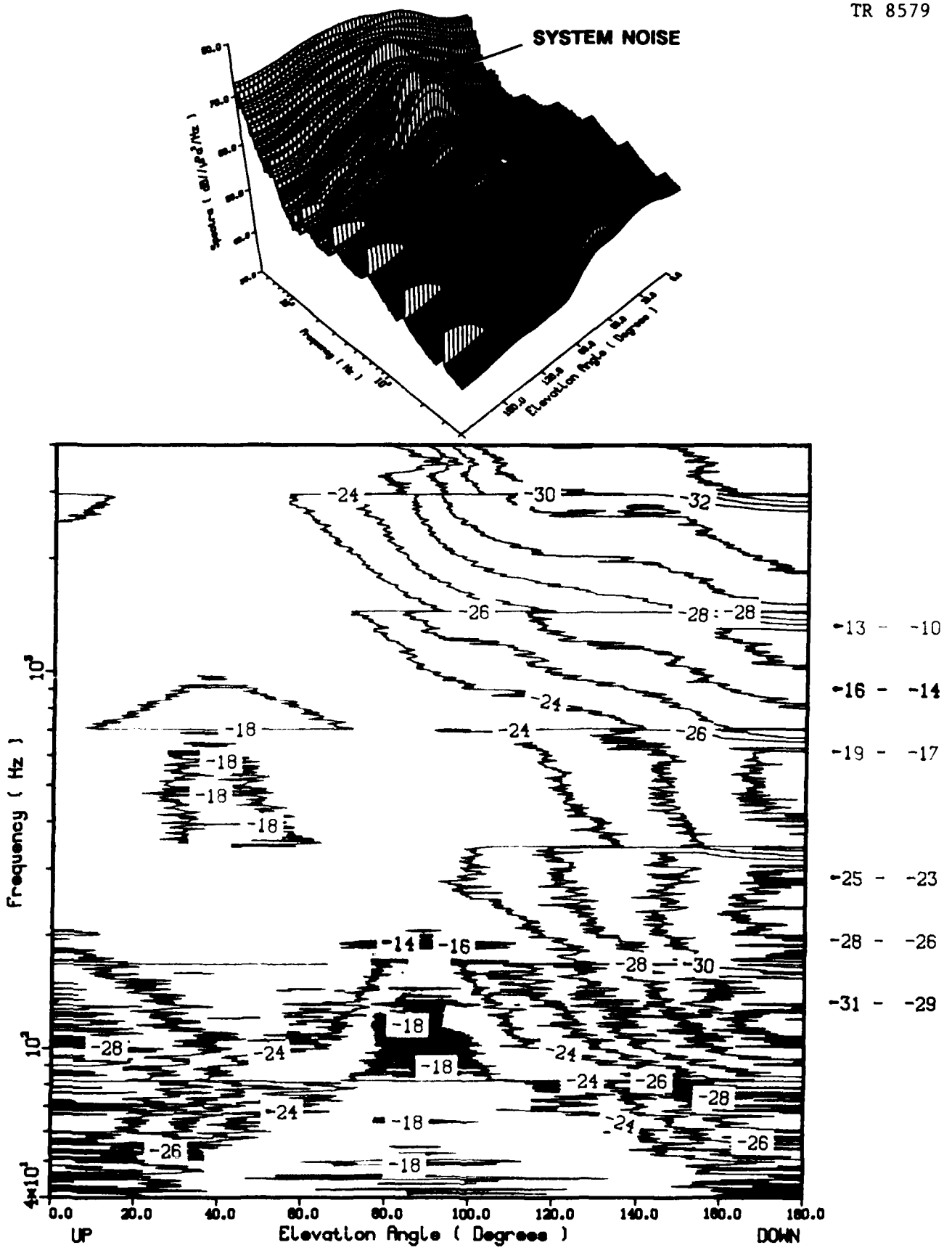

Figure 16. Composite Narrowband Elevation Angle-Frequency Spectra, 7.97 m/s Wind Speed

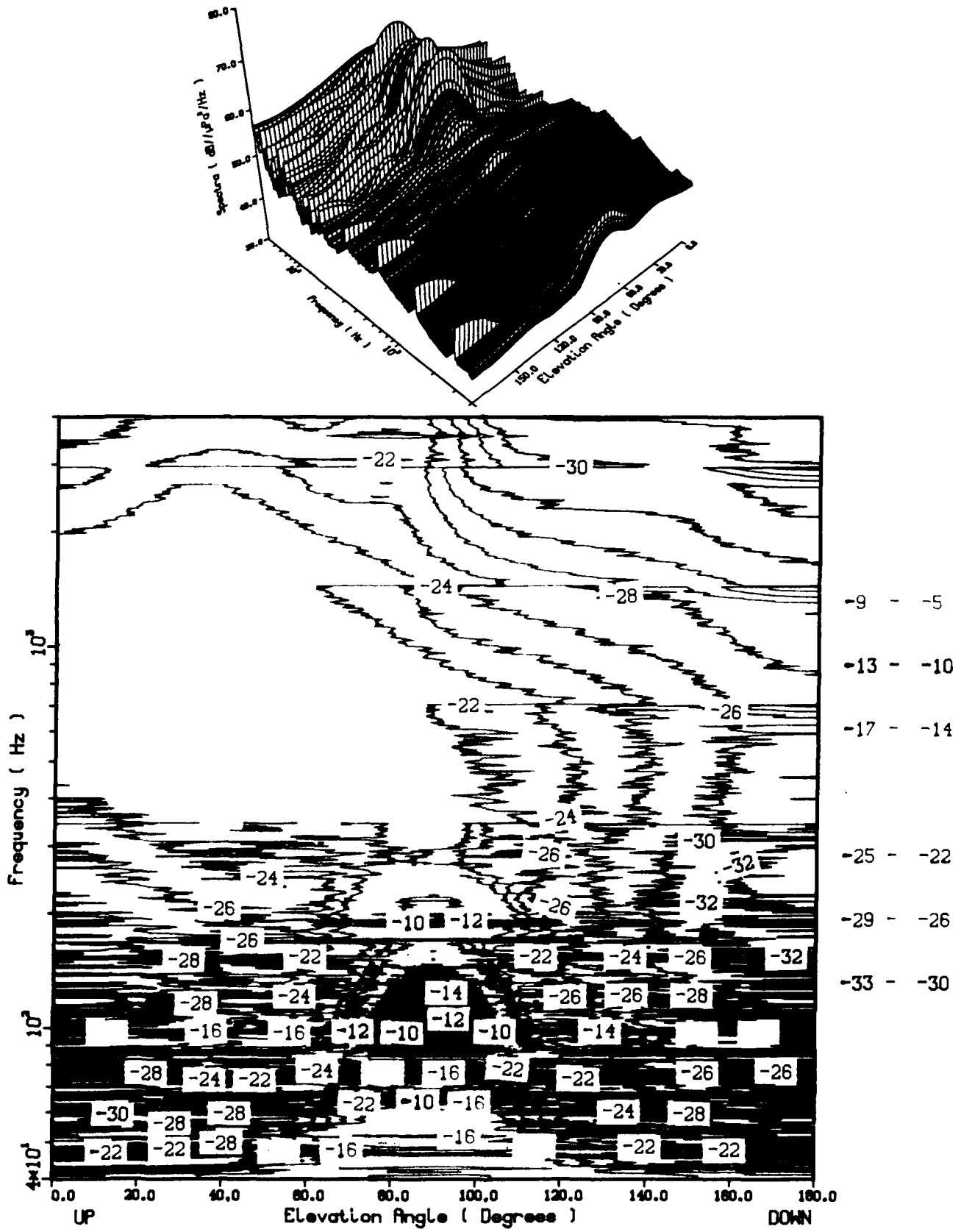

Figure 17. Composite Narrowband Elevation Angle-Frequency Spectra, 4.37 m/s Wind Speed

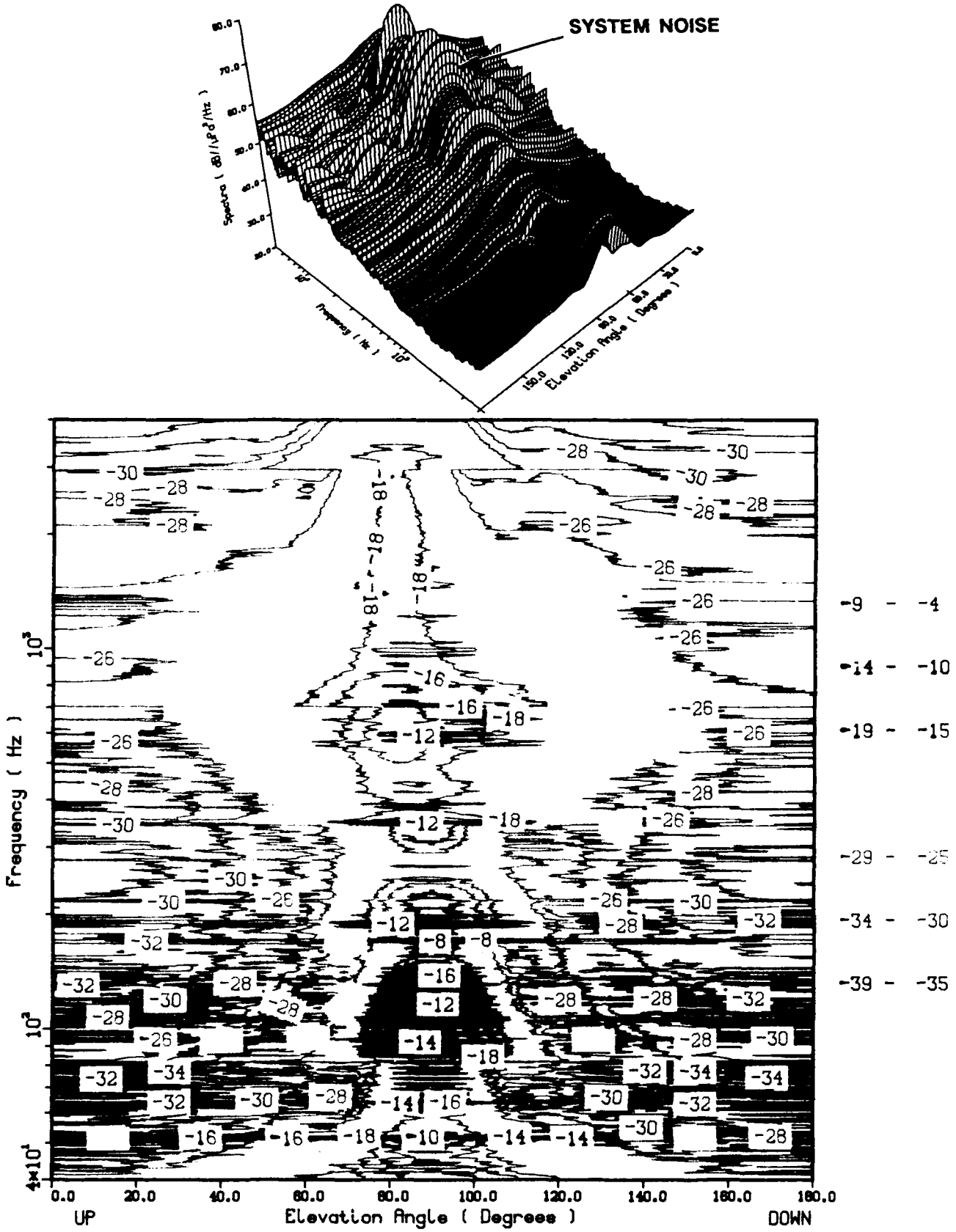

Figure 18. Composite Narrowband Elevation Angle-Frequency Spectra, 2.06 m/s Wind Speed

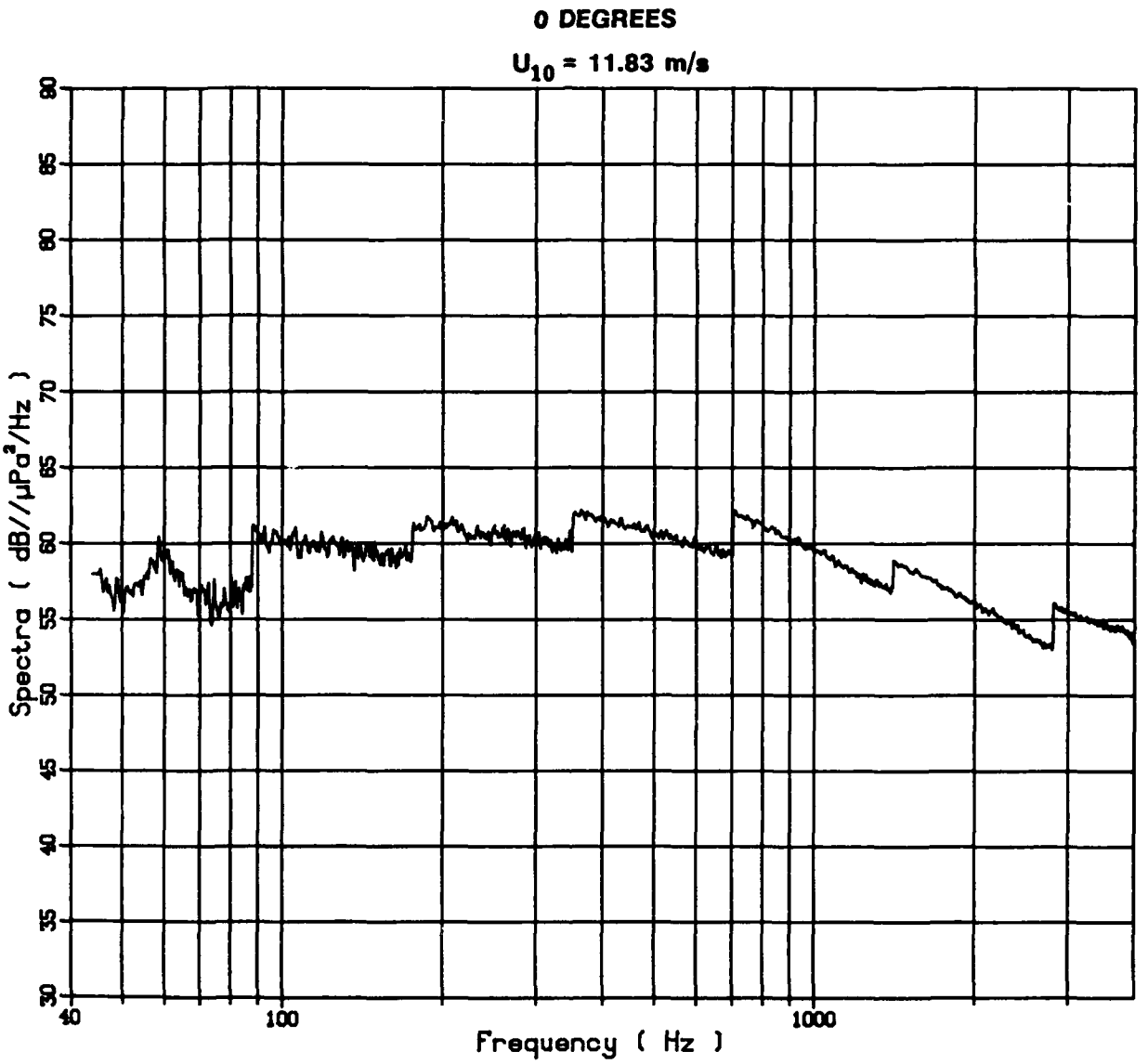

Figure 19. DOAS "Straight Up" Cut Illustrating a Diffuse Acoustic Source

angle "cut" through the surface at 0°, i.e., "straight up." These demarcations are not present if the spatial extent of the acoustic source is less than the spatial resolution of the antenna. This is illustrated in figure 20, which is an elevation angle "cut" at 82° of the DOAS shown figure 20. In figure 18 a broadband "target" is evident at that elevation angle. Because the "target" is spatially compact, the aperture demarcations are not present in figure 20. These three characteristics will be evident to some degree in all of the figures and are a detraction from the important features of the figures.

The important feature of figure 15, which is characteristic of all except the very low wind speed data, are the levels above the horizontal, i.e., 90°, are significantly higher than below it, with a broad peaking of the spectra at an elevation angle of about 40°. This is characteristic of a plane or a thin layer of sources, such as are present near the sea surface. The beamformer coverage of this acoustic source area increases as the elevation angle becomes larger, i.e., further from the zenith. However, the received source level is reduced by the larger source-to-receiver distance as the elevation angle becomes larger. These two opposing phenomena cause the maximum in the DOAS. In calculating the directional spectra, the received acoustic levels are normalized by the solid-angle coverage of the beamformer, which removes this peak. Figure 16 is quite similar to figure 15 except that significantly larger values of spatially diffuse energy are present below 100 Hz. This presumably local shipping- and industrial-source acoustic radiation is quite frequently observed contaminating much of the data taken below 100 Hz. Also note in this figure a narrowband target at 80° elevation angle and 3500 Hz. Figure 17 is an example of a low wind speed data set, i.e., no whitecaps present. The general pattern of the DOAS is not changed, only the levels are lower. However, note that at high frequency and at an elevation angle of 80° there is a broadband "target." In figure 18 this "target" is better defined. Figure 18 displays the lowest level data obtained. Here the aliasing lobes have completely disappeared because preamplifier noise that is contaminating the diffuse-source noise has the same value at 0° and 180°. A broadband discrete source is clearly evident at 82°. This shallow angle, 8° above the horizontal, is most likely a distant source arriving along a bottom bounce

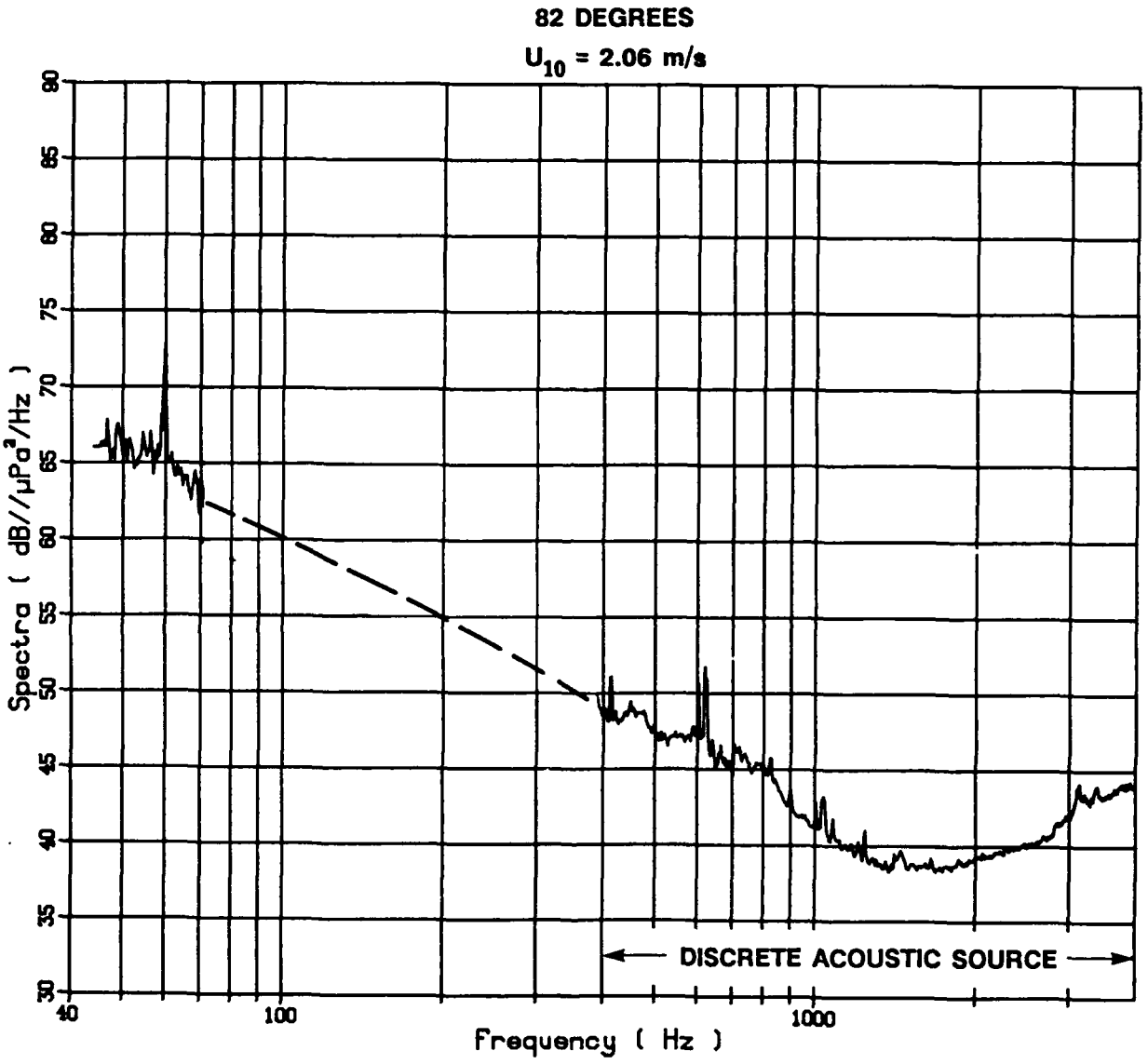

Figure 20. Low Wind Speed DOAS at 82° Elevation Angle Illustrating a Discrete Acoustic Source

path. This energy is nearly always present when the wind speed is low enough to observe it and probably should be considered as part of the acoustic ambient at this location. There are two possible explanations for this energy. This elevation angle corresponds almost exactly with the direction from which sounds of biological, industrial, or shallow-water wave action origin coming from the top of the escarpment would reach the measurement site. An alternative source is acoustic energy in the TOTO basin that is efficiently coupling to the measurement antenna by the waveguide selection process of the propagation. The TOTO long-distance propagation is characterized by a bottom-surface reflected path which efficiently propagates at only a narrow selection of angles. The permanent refractive character of the media limits the small grazing angle bottom reflections, and the bottom reflection loss, which increases with increasing grazing angle, limits the high-angle arrivals to relatively short range. Thus the channel selectively limits the propagation mode, i.e., angles, to a relatively narrow angular window. A calculation was made of the received vertical angle of all eigenrays between a specific source and a receiver in TOTO. Figure 21 shows the received angle of all multipaths, i.e., eigenrays, between a near-surface source and a 213-meter-deep receiver separated by 38 km. The peak of the structure is 7° from the horizontal, which closely matches the 8° shown in figures 17 and 18. The lack of symmetry about the horizontal in the current data relative to figure 22 is presumably a result of a multipath being "stripped" by the sloping approach to the measurement site. Additional support for this argument is seen in figure 17, which shows an easily identified narrowband target at 82° and 3500 Hz. This is a known source located some 30 to 40 miles from the measurement location. This identifies the preferred propagation path as being identical to the above argument. The frequency spectra of the beamformer steered to the energy being discussed, figure 23, shows a frequency spectral shape quite similar to that of the familiar "snapping shrimp" described by Albers.[20] Albers documented sound pressure levels in the vicinity of the shrimp "beds" of 68 dB/μpa in a 50 Hz band, although there is some ambiguity in the description with regard to the measurement bandwidth This means a spectral level in excess of 65 dB//μPa^2/Hz relative to our measured value of 44 dB//μPa^2/Hz at 4000 Hz. This level difference implies that the source is local because the propagation loss in a typical 18 km bottom, surface/bottom propagation cycle in the 2 kHz to

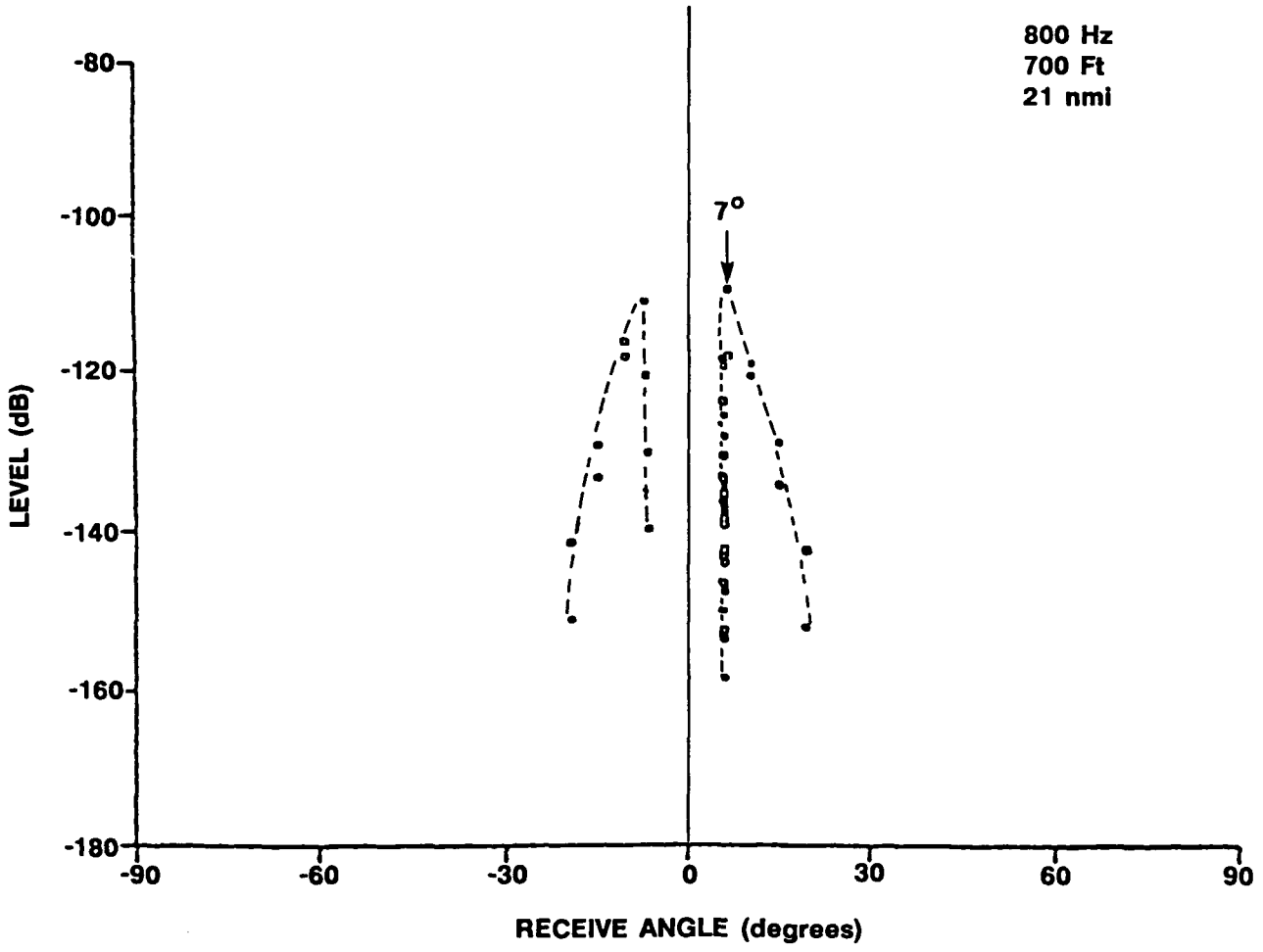

Figure 21. TOTO Preferred Angular Window for Efficient Propagation

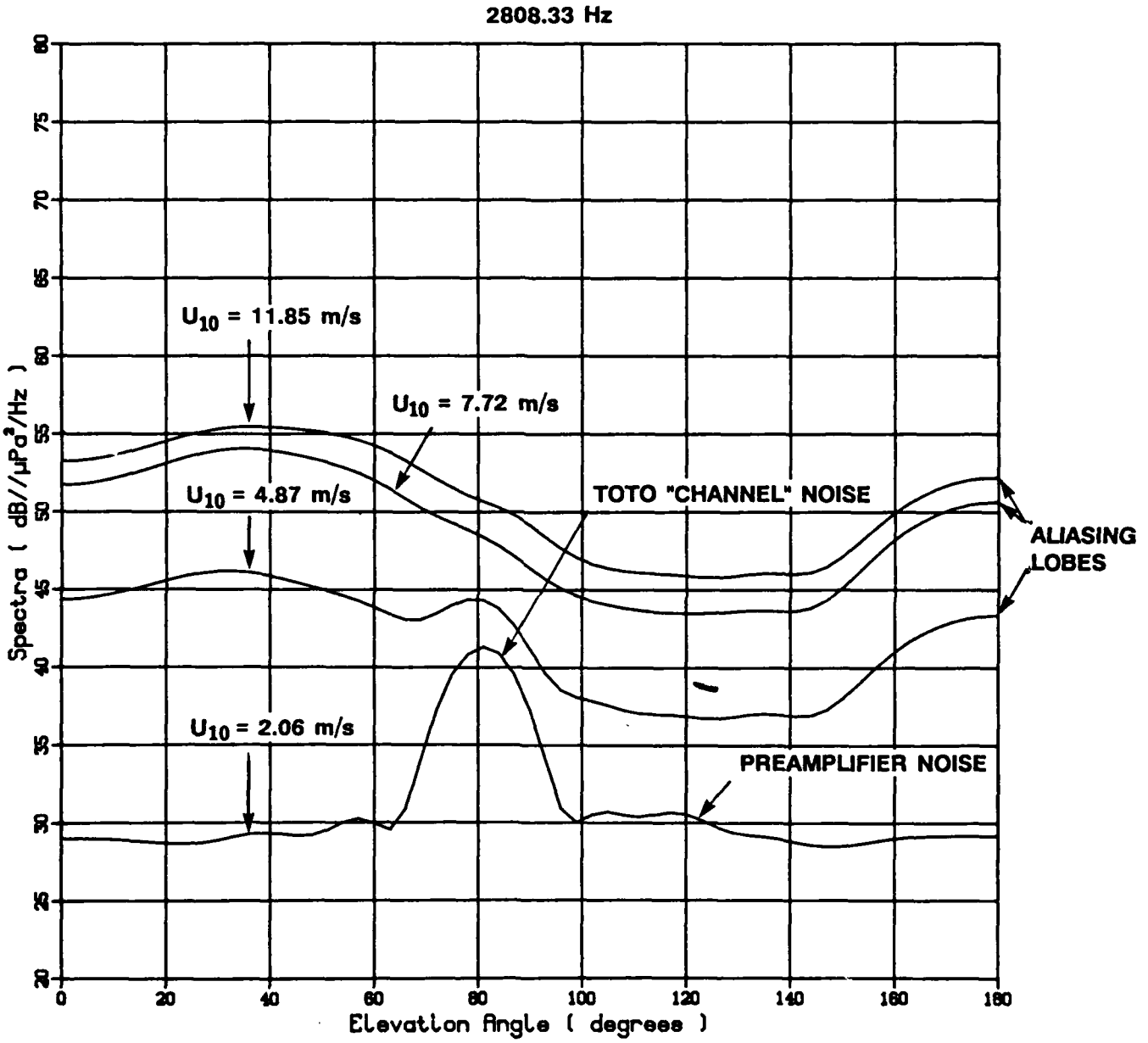

Figure 22. DOAS Elevation Angle "Cuts" Illustrating TOTO "Channel" Noise

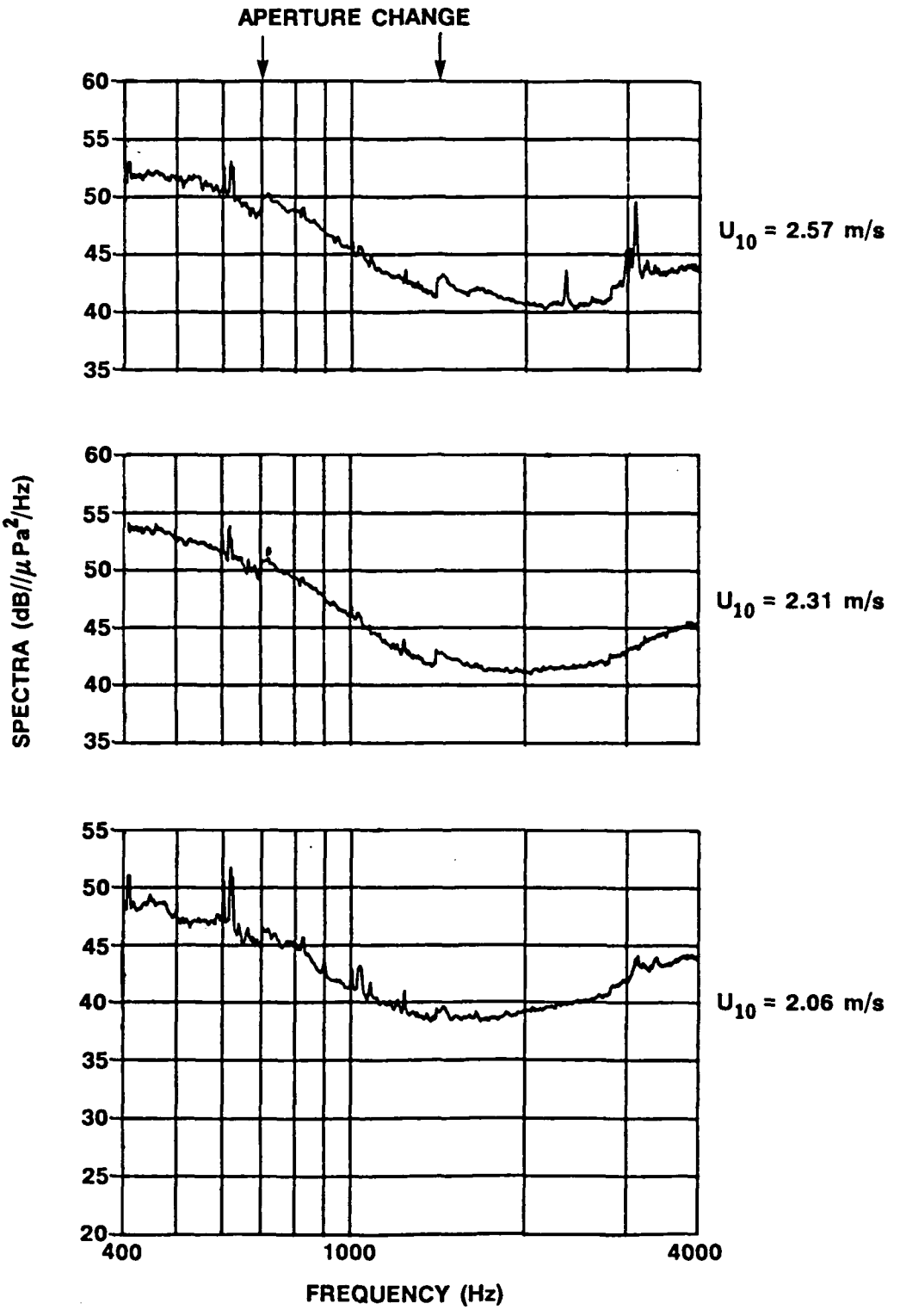

Figure 23. Measurements of the TOTO "Channel" Radiation

4 kHz range would be expected to be larger than this difference. The data are thus unable to choose between the two alternatives.

For either explanation we conclude that the acoustic energy arriving via this path forms a nearly stationary contribution. Figure 23 shows the DOAS at 82° for those cases in which the presumed "channel" radiation nearly dominates the frequency range shown. For the times in which measurement was possible, the level changed by less than 4 dB. The fact that some discontinuity is observed at the aperture changes, as noted in the figure, indicates that there is probably a spatially diffuse contribution, indicating that the range of values is even less than 4 dB. Figure 22 is a bearing "cut" of a selection of measurements chosen to illustrate a range of wind speeds. As seen in the figure, the acoustic data will be affected by this source of energy below a 4 m/s wind speed. This character of the data will be discussed again when we present the directional spectra data. The local maxima in the data at 180° is a result of the aliasing lobes.

4.3 EIGENVECTOR DECOMPOSITION

As discussed in section 3, there are two products of the eigenstructure decomposition, i.e., eigenvalues and eigenbeams. When the eigenvalues, which are positive scalars for a Hermetian matrix, are found they are sorted by magnitude. The convention we will use is that the largest eigenvalue is always numbered 1. Following reference 6, the eigenvalues are scaled so that their Pythagorean sum equals the average of the major diagonal terms in the csd matrix, i.e., the total acoustic sound pressure level. This approach follows from the orthogonality of each of the terms in the eigenstructure decomposition. Four examples of the eigenstructure decomposition of the data are displayed in figure 24. Each block in that figure shows the distribution of the acoustic autospectral density by eigenvector for seven frequencies. Recall that each eigenvector represents the spectral density contribution of a particular statistically independent component of the vertical ambient pressure field. There are three characteristics of these plots that should be noted. First, and most important, there is an underlying regularity to the distribution. Second, the regularity is broken in several cases by the appearance of

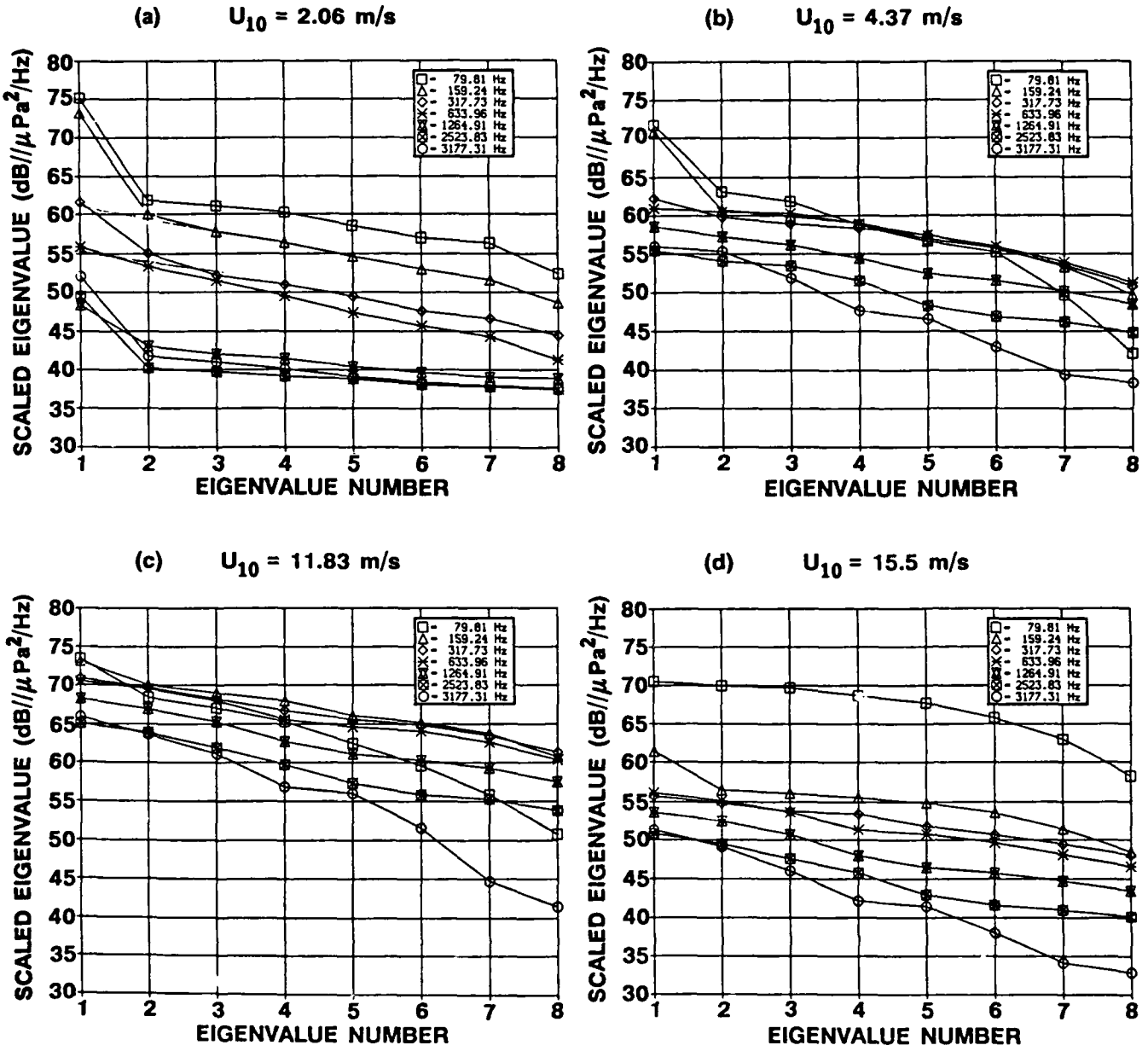

Figure 24. Examples of Eigenvalue Decomposition

an anomalously large value in the first or second eigenvalue. When the eigenbeams of these particular eigenvalues are examined we find that they are associated with acoustic plane waves or contamination, such as common-mode noise, which masks as a plane wave. These two characteristics illustrate how the eigenvector decomposition partitions the acoustic field into discrete sources (plane waves) having a discontinuous eigenvalue spectra and diffuse sources (a spatially uniform distribution of energy) which have a continuous eigenvalue spectra. The third characteristic of the figures that needs to be pointed out is that the 79.81 and 3177.31 Hz curves "fall off" faster with increasing eigenvalue number than the other frequencies. This is caused by the reduction in the number of independent eigenvectors caused by a reduced nondimensional acoustic aperture. The number of independent plane waves that can be resolved by an antenna is twice the nondimensional aperture, i.e., the ratio of the physical aperture divided by the wavelength. At 80 Hz the aperture was reduced, relative to the other apertures, because of the loss of the two end hydrophones caused by the hydroacoustic-induced voltage overload discussed in section 3. The 80 Hz aperture was further reduced by the failure of hydrophone number 31, so this low frequency aperture only had five hydrophones. Thus there are only five independent eigenvectors present. The same holds true for the 3200 Hz frequency, only for a different reason. In this case the aperture reduction is because the frequency is further below the design frequency of that aperture than is true at the other frequencies. This can be seen by comparing each analysis frequency with the design frequency of the antenna used (table 1). At 3200 Hz the nondimensional aperture is 2.3 compared with 3.6 for the other apertures, except for 80 Hz which is 2.5.

In figure 24(a) an obvious discrete source is present at six of the seven frequencies. This corresponds to the DOAS pictured in figure 18 which shows that the low frequency plane wave is the common-mode noise and at high frequency the discrete source appears as a broad bandwidth "target" at an 80° elevation angle. In figures 24(b) and 24(c) the only two discrete sources are due to the common-mode noise. In figure 24(d) the common-mode noise appears only at 159.24 Hz because an energetic low frequency diffuse source appears to be present at 80 Hz.

Next we describe the results of the eigenbeam analysis, where the eigenbeams are calculated according to equation (6) of section 2. Eigenbeams resulting from a purely diffuse acoustic field occurred in two distinctly different forms, as illustrated in figure 25, which shows a three-dimensional function with both elevation angle and eigenbeam number as independent variables. The dependent variable, i.e., the eigenbeam, is an arbitrary scale expressed in dB. As before, the eigenvectors and thus the eigenbeams are sorted according to the magnitude of the eigenvector, so the values of the peaks decrease monotonically from back to front of the plots. Figure 25(a) shows a pair of diverging, back-to-front ridges. Each eigenbeam appears as a pair of mainlobes except the first one in which the pair has merged into a single lobe. Because each eigenbeam represents a component which is statistically independent of all other eigenbeams, the pattern is consistent with a distributed sea surface source and its bottom reflection. As the sources become more distant from the antenna, both the direct and bottom bounce occur at shallower angles until the two merge into a single arrival, slightly shallower than 90°. This pattern is typical of the data at low frequencies although it was also observed at a high frequency and low wind speed condition. Of particular interest in this pattern is that the eigenbeam associated with the near-horizontal elevation angle has the largest amount of energy. If the sources are monopole in nature then the energy in the near-horizontal beams would be larger than at the steeper angles because of the larger source area contributing to those solid angles as long as there is sufficient source energy in that direction, as would be the case for a monopole source.[21] The second pattern is seen in figure 25(b). Here the acoustic field decomposes into eight statistically independent directions with the levels monotonically decreasing from "straight up" to "straight down," indicating no dependence between the direct arrivals from the surface and (presumably) the reflections off the bottom. Note, however, that now the maximum eigenvalues are associated with the energy coming from directly overhead and diminish monotonically as the elevation angle goes to 90°, as would be the case if the diffuse source were dipoles. The continual decrease in eigenvalue level as the angle continues through 180° is presumably caused by bottom reflection losses. This second pattern is typically observed above a couple hundred hertz, but it was occasionally seen at low frequency and high wind speeds. To the extent that a

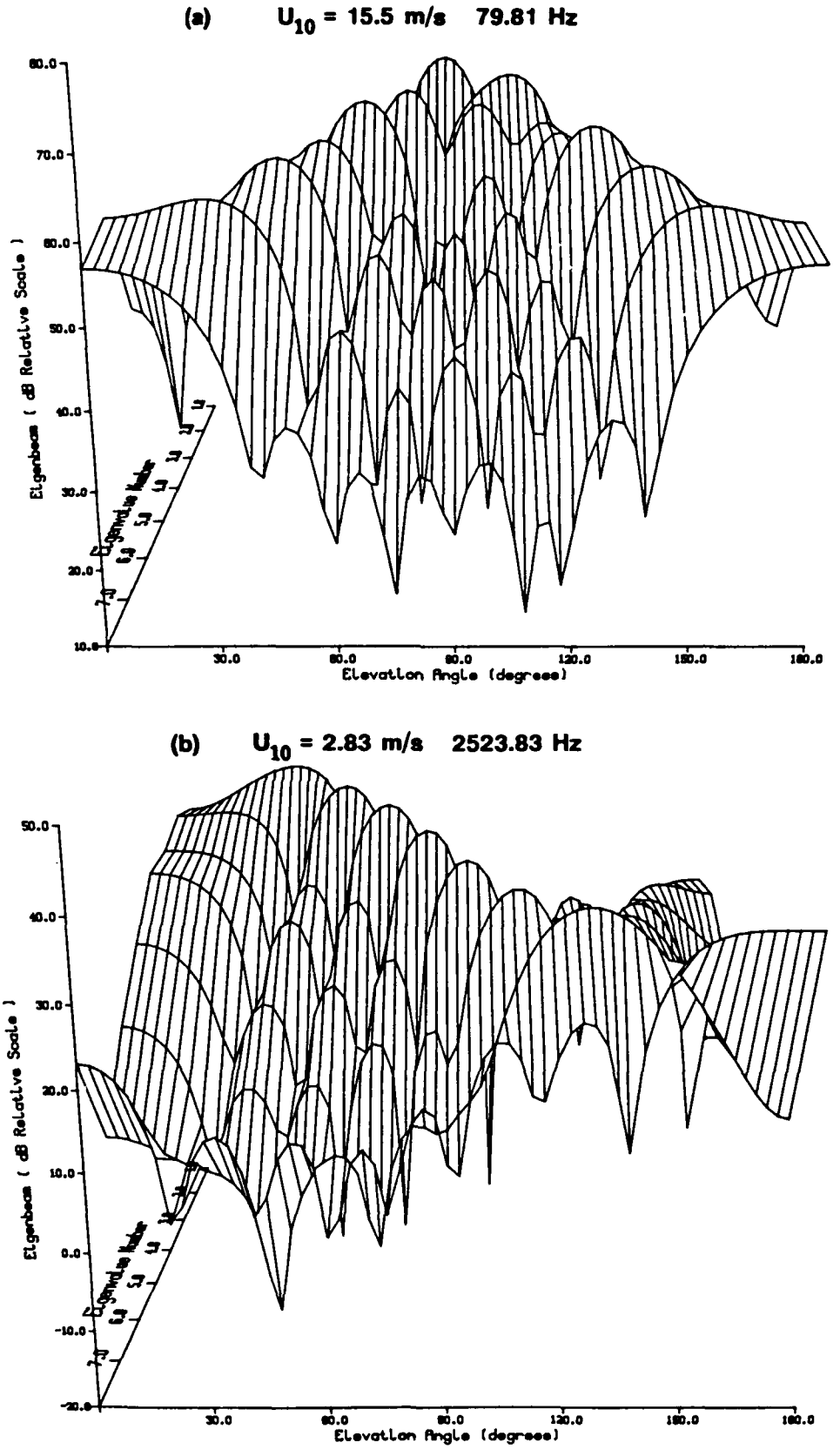

Figure 25. Typical Eigenbeam Types

general statement can be made, the low frequency eigenbeams were like figure 25(a) and a conversion to the figure 25(b) pattern occurred above 500 Hz.

As we saw in figure 24, a plane-wave-like component was identified in the eigenvalues as an anomalous level for the first or second eigenvalue. Figure 26 illustrates the eigenbeams associated with the plane-wave-like components. There are two basic forms that these components take in the eigenbeam plots. The first kind, shown in figure 26(a), is when the plane wave, i.e., maximum eigenvalue, occurs in the same direction that the natural ambient maximum would occur. Thus the general pattern of the picture is an eigenbeam distribution resulting from a diffuse monopole source with an anomalously large value at 90°, which in this case is the common-mode noise. In figure 26(b) the plane-wave-like eigenbeam does not "fall in line." The "natural" maximum, i.e., first, eigenbeam is 0°, not 82° as seen in the figure. The energy of the eigenbeam at 82° contains two independent acoustic sources: (1) sea surface contribution from that angle, and (2) a plane wave from that angle, which in this case is the TOTO "channel" radiation discussed previously. It is the contribution from the second source that caused the anomalously large eigenvalue. There are two important points to be made from this analysis. First, in the absence of a plane wave acoustic source the magnitude-ranked eigenvalues form a smooth curve as noted in reference 6. The corollary to this is that discontinuities in the magnitude-ranked eigenvalue distribution mark the presence of an independent plane wave in the measured acoustic field. Second, the eigenbeam plot identifies the eigenvector that has been perturbed by the plane wave. These two points combine to form a simple procedure for removing the plane wave from the csd matrix. This procedure will be used in the next section.

4.4 VERTICAL DIRECTIONAL SPECTRA

A first-order approximation of the directional spectra was calculated from the DOAS as discussed in section 2. Figure 27 is an example of this calculation done for the narrowband composite DOAS shown in figure 15. One can see, by comparing with figure 15, that this is a better measure of the acoustic field for two reasons. First, because the calculation accounts for the

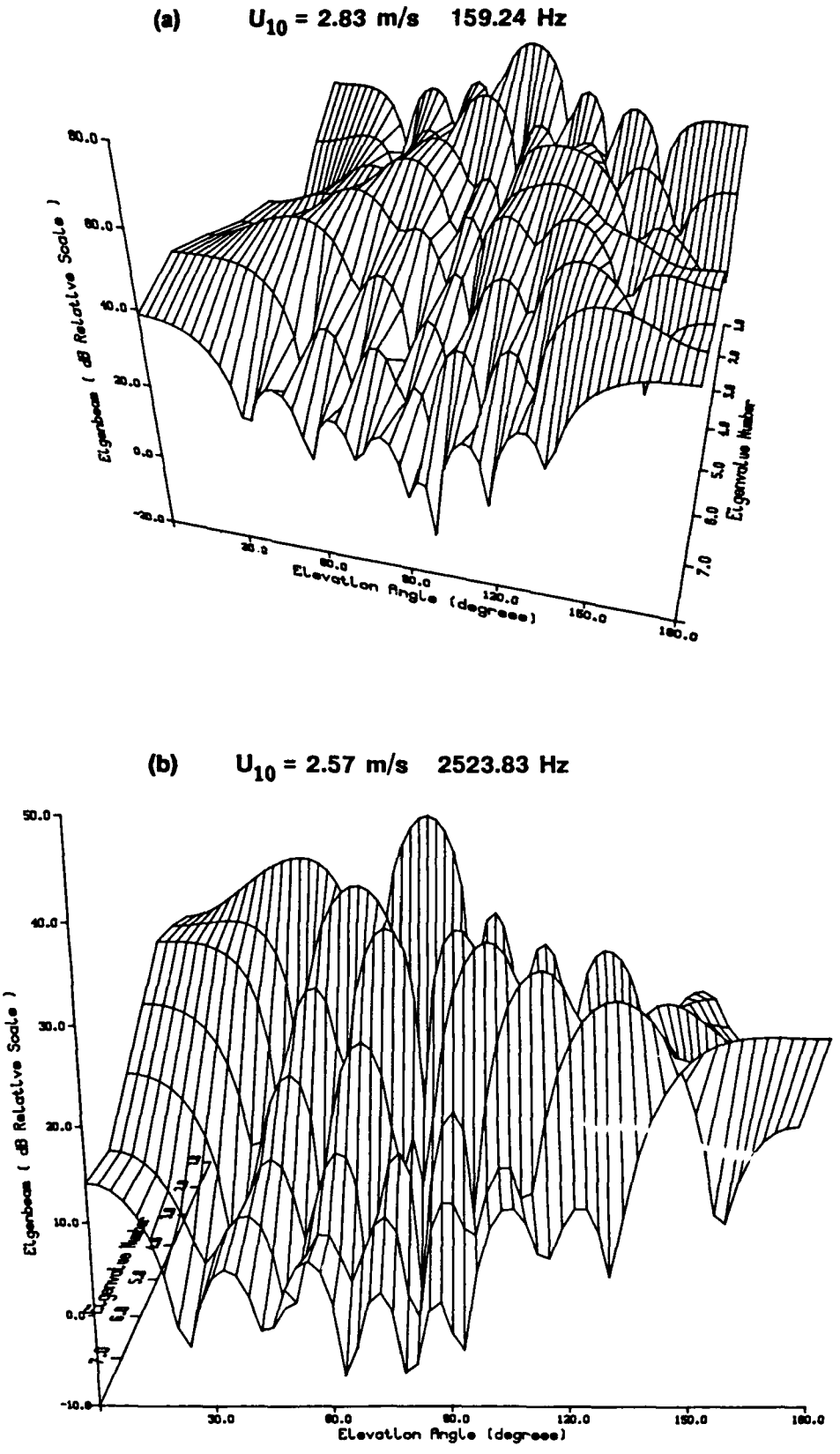

Figure 26. Examples of Plane Wave Contamination in Eigenvector Analysis

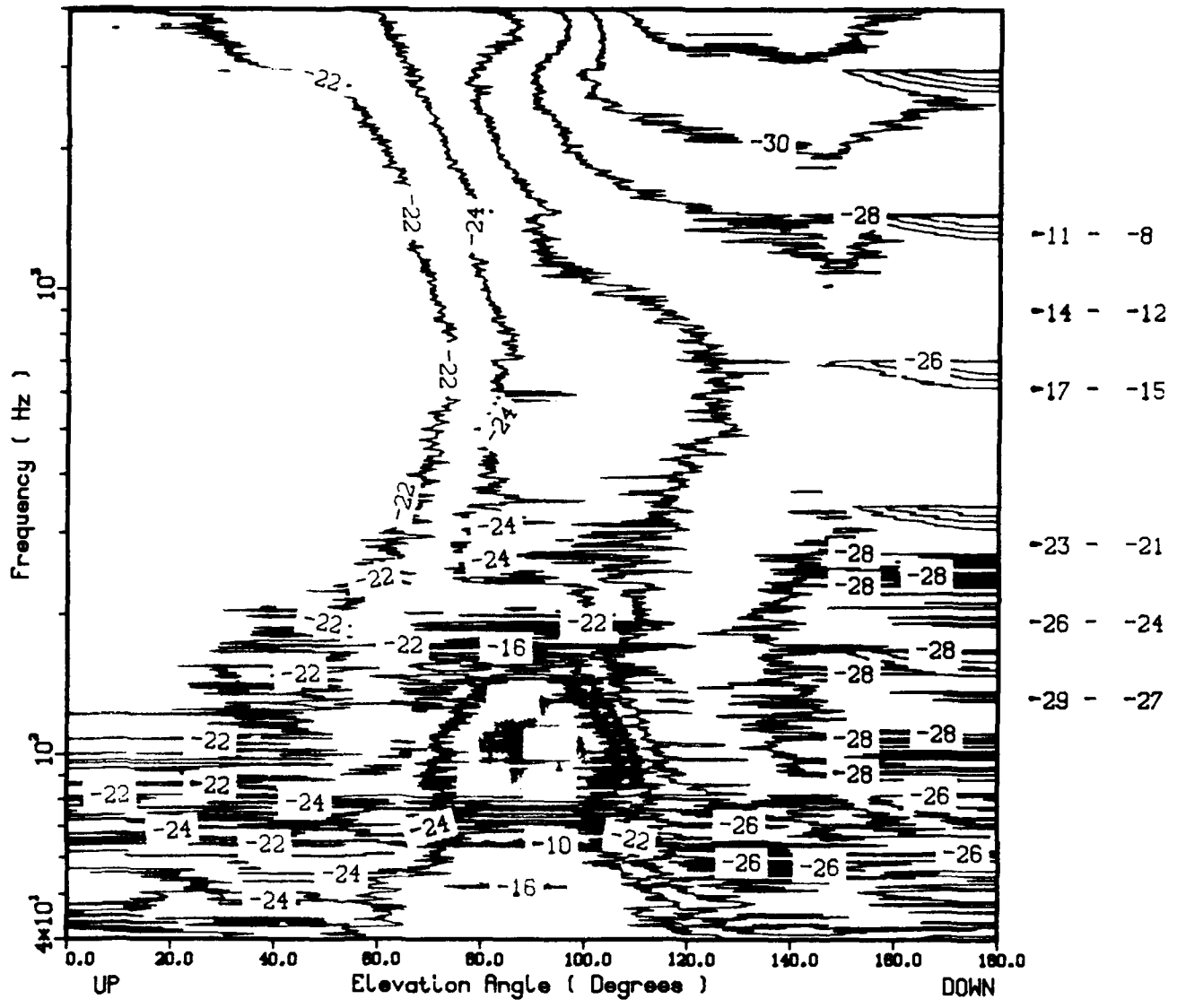

Figure 27. Composite Narrowband Elevation Angle-Frequency Directional Spectra, 11.83 m/s Wind Speed

change in solid-angle coverage of the beamformer, the discontinuities at the aperture changes are no longer present, although the aliasing errors remain. Second, for the same reason, the broad maxima near 40° elevation angle is moved to 0°, which represents the directional spectra for the anticipated dipole-like sea surface sound source structure.

As previously discussed, the frequency variation of the spectra is relatively smooth and thus there are advantages to synthesizing proportional bandwidth spectral estimates. Note that the dependent variable remains a spectral density function, not band levels, but the spectral estimates are now determined by all of the energy in the proportional bandwidth, which in the present case will be one-third-octave bands. This process significantly reduces the amount of data present in the data base. The uniformity of the data within a one-third-octave bandwidth with frequency was quite good above 200 Hz. It was not always as good below 200 Hz because the data often exhibited "tonal" components. In these cases the basic assumption is compromised. We will continue to draw attention to this fact as it affects our interpretation of the data. However, the rest of the data shown in this section employed the proportional bandwidth analysis.

We begin our examination of the directional spectra by viewing its wind speed dependence. This is done in the same manner that the wind speed dependence of the total sound pressure level was examined in section 4.1, i.e., by fitting a power law model to the nondimensional friction velocity separately for the "with" and "without" whitecaps present cases. However, in this case the dependent variable is the directional spectra, not the total sound pressure level. This process was repeated at eight logarithmically spaced frequencies and nine elevation angles. Figure 28 illustrates examples of this description. Common to all of the analysis was the result that the directional spectra was independent of the nondimensional friction velocity when whitecaps were present. Because of the meager amount of data for this case, the conclusion should not be considered quantitatively correct. However, the result is qualitatively consistent with the results found in reference 19 for the total sound pressure level and the results of reference 22 for the inferred directional spectra. When whitecaps were not present, the power law

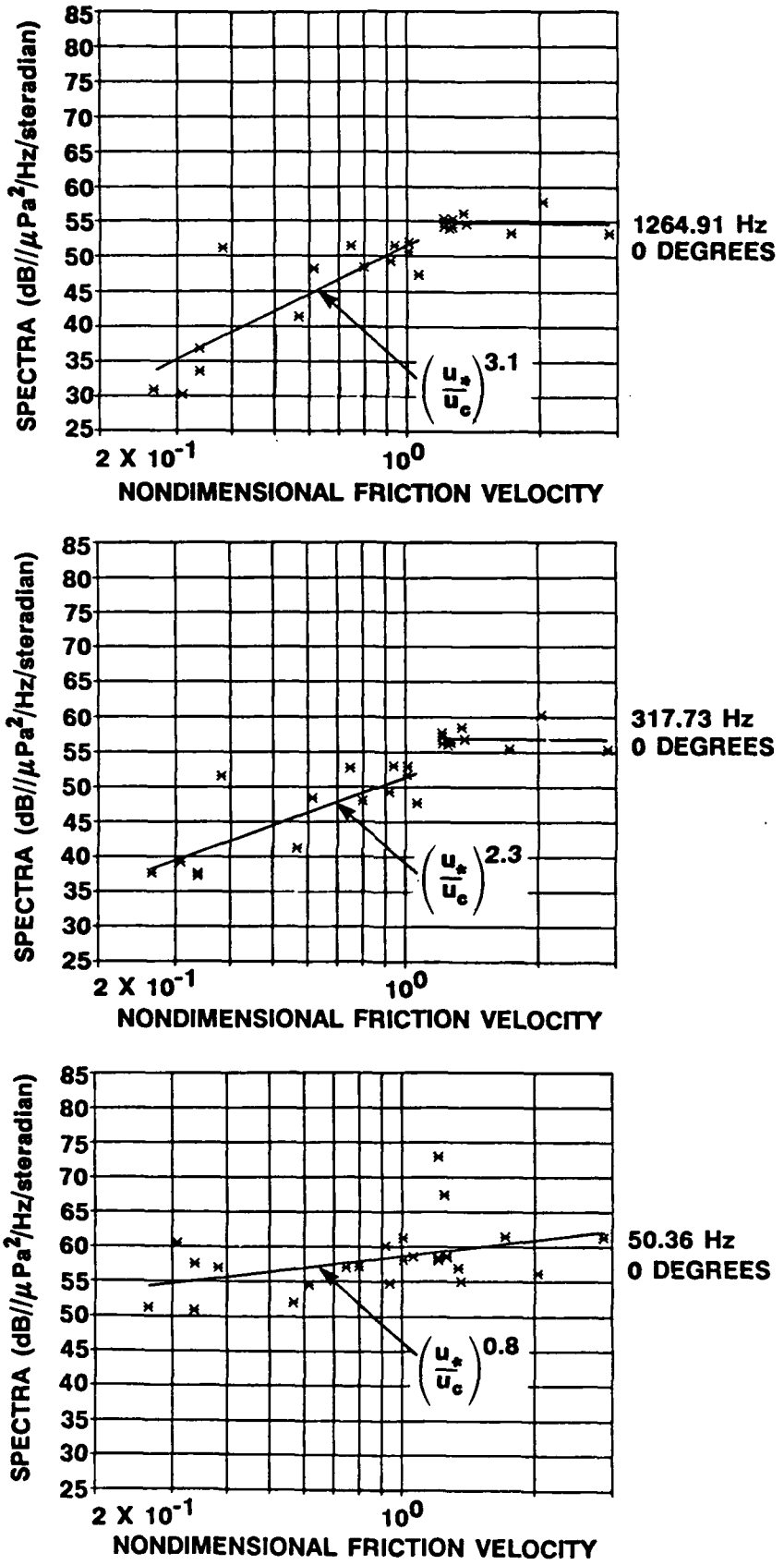

Figure 28. Examples of the Wind Speed Dependence of the Directional Spectra

is seen to vary significantly with frequency and elevation angle. By tabulating the power law fit to the data as a function of both elevation angle and frequency, one can view the relative wind speed dependence of the directional spectra as a function of frequency and elevation angle for the nonwhitecapping case. This construction is shown in figure 29. The system common-mode noise contamination is removed by substituting for the measured values at 90° elevation angle in the frequency range of 50 to 600 Hz with values consistent with the values in the vicinity of the contaminated region. There are two obvious features in the figure. First, the data above and below 300 Hz show significantly different wind-speed dependence. This is an important point that will be returned to. In the next paragraph we will discuss evidence that prior to the onset of whitecapping there appears to be a lack of wind-related noise sources below 300 Hz relative to above 300 Hz. The complex spatial and frequency content of the acoustic field below 300 Hz is evident in figures 16 through 18. Little more can be said than that the acoustic ambient below 300 Hz is importantly influenced by local human activity. The second dominant feature of figure 29 is the asymmetrical "saddle" shape in the elevation angle dependence above 300 Hz. The high side of the "saddle" is the zenith of the array. The power law exponent of 2.8 to 3 is consistent with past experience.[19,22] The other side of the "saddle," i.e., looking down at bottom reflections, has consistently smaller exponents, i.e., 1.5 to 2.0. This indicates that the pressure field coming from that direction is not simply the reflection of the sea surface sound but includes a non-sea surface generated component such as biological activity. The lowest wind speed dependence in the directional spectra above 300 Hz is seen to exist from approximately 70° to 100°. The likely explanation for this is the combination of escarpment radiation and "channel" radiation discussed in section 4.2. In summary, the acoustic ambient at all frequencies below approximately 300 Hz is importantly influenced by local human activity and low wind speed dependence without whitecaps present, and above 300 Hz the energy coming from the sea surface is dominated by a cubic wind speed-dependent mechanism. Near the horizontal direction and in downward looking directions the wind speed dependence is reduced by the bottom reflection and there is a clear non-wind speed component present.

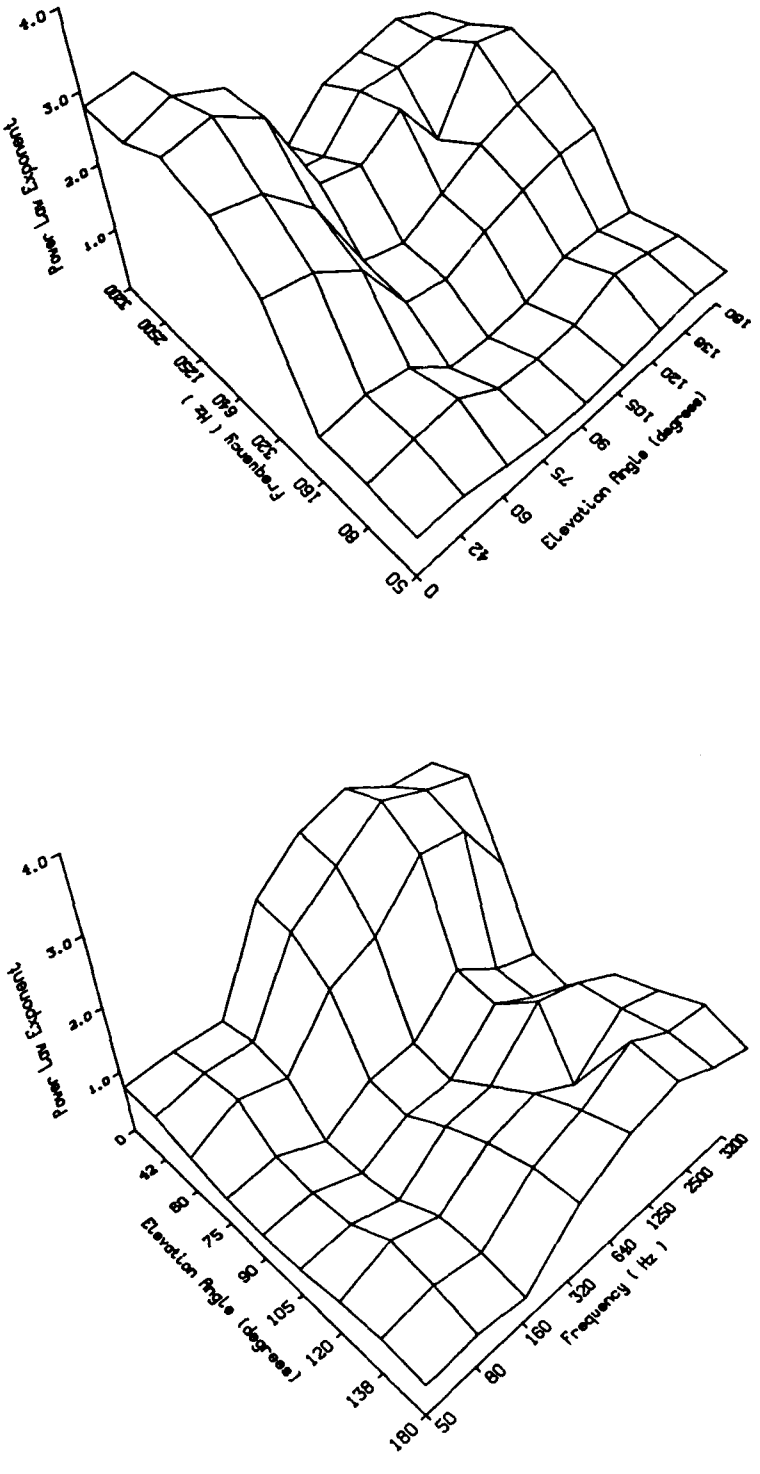

Figure 29. Directional Spectra Wind Speed Power Law Exponent

Note that the calculation of the directional spectra performed in this study assumes that the directional spectra varies slowly relative to the beamformer pattern function mainlobe width. This would not be the case when a strong plane wave is present in the measured pressure field. Thus all of the directional spectra presented in this section have been processed, as discussed in section 4.3, to remove plane wave "contamination." This includes the "common-mode noise," discussed in section 3, which appears in the data as a plane wave at 90°. Directional spectra with all plane waves removed will be labeled as "corrected directional spectra." Displaying the data is difficult because the space of interest has four dimensions, i.e., spectral level, frequency, elevation angle, and wind speed. Our approach will be to show the three-dimensional frequency-elevation angle directional spectra with wind speed as a parameter. Five examples of the data were chosen to represent the range of wind speed data observed. Topographical and surface plots of the figures are shown in figures 30 through 34. Note that the topographical plots are "whitened" in the frequency dimension to reduce the dynamic range but the surface plots are not prewhitened. There are several features of this sequence of figures worth discussing. As the wind speed increases, the energy at frequencies above 300 Hz increases more rapidly than the energy below 300 Hz. Prior to incipient whitecapping, i.e., about 6.5 m/s, the frequency-elevation angle space contains two types of regions. One region has the maximum value indicated as a ridge that peaks at angles nearly the same as in the case prior to the removal of the plane wave. The result acts as though the removal was incomplete. The reason for this is that the component still present after the plane wave removal appears from the beam response and the eigenvector decomposition to be spatially diffuse. This is not a surprising conclusion for either the "escarpment" radiation or the "channel" radiation sources. However, it should not be the case for a "common-mode" noise. Thus we conclude that a spatially diffuse acoustic source is present which at times has frequency high spots that are harmonically related. It was coincidental that the "common mode" noise peaked on this low frequency ridge. As the wind speed increases, the nearly symmetrical pattern previously described is replaced with a nonsymmetrical pattern showing the dominance of the surface-generated acoustic radiation. A striking feature of figures 31 and 32 is the movement of one pattern to the other near 300 Hz. Finally, we note that when

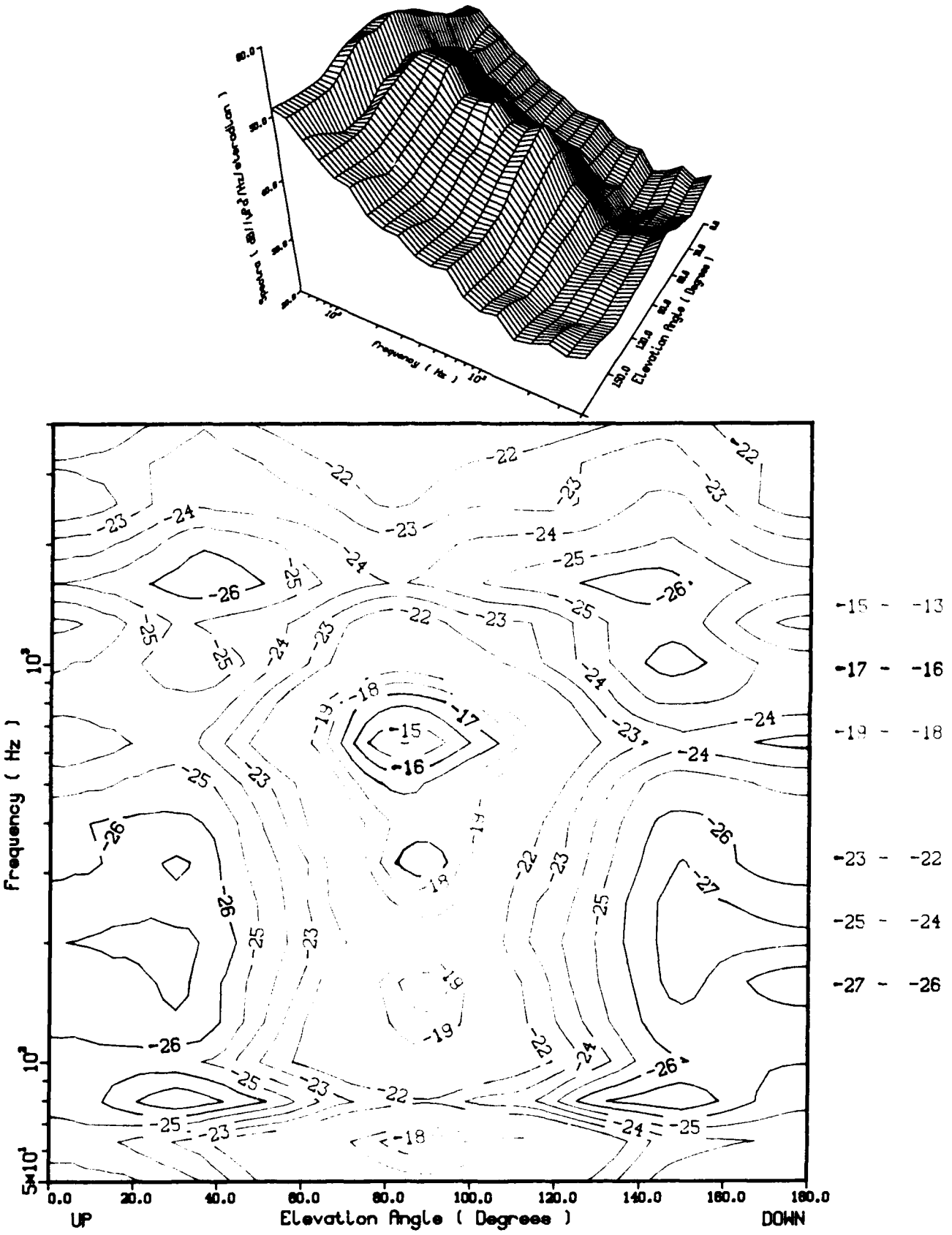

Figure 30. Corrected Directional Spectra Versus Frequency and Elevation Angle for 2.06 m/s Wind Speed

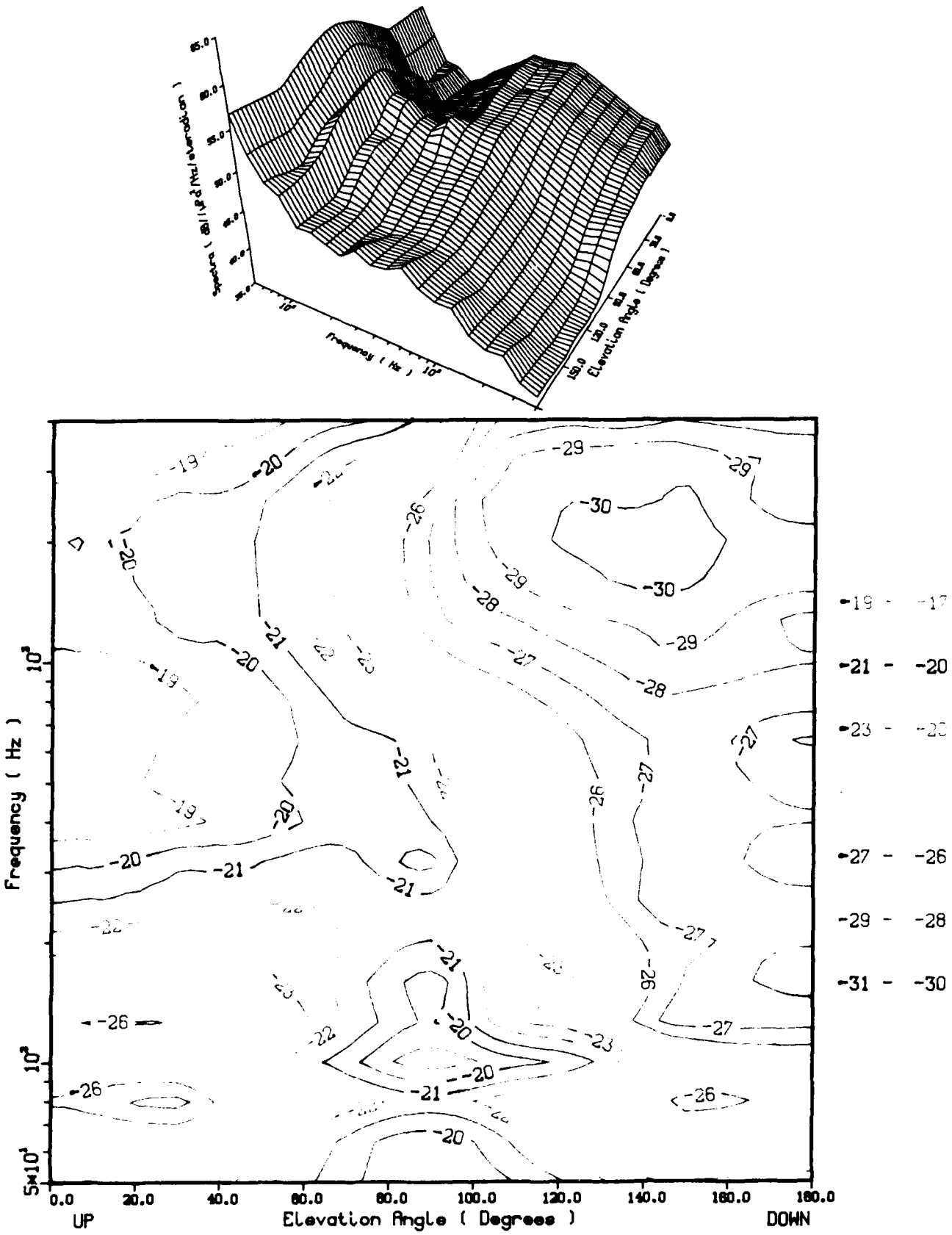

Figure 31. Corrected Directional Spectra Versus Frequency and Elevation Angle for 2.83 m/s Wind Speed

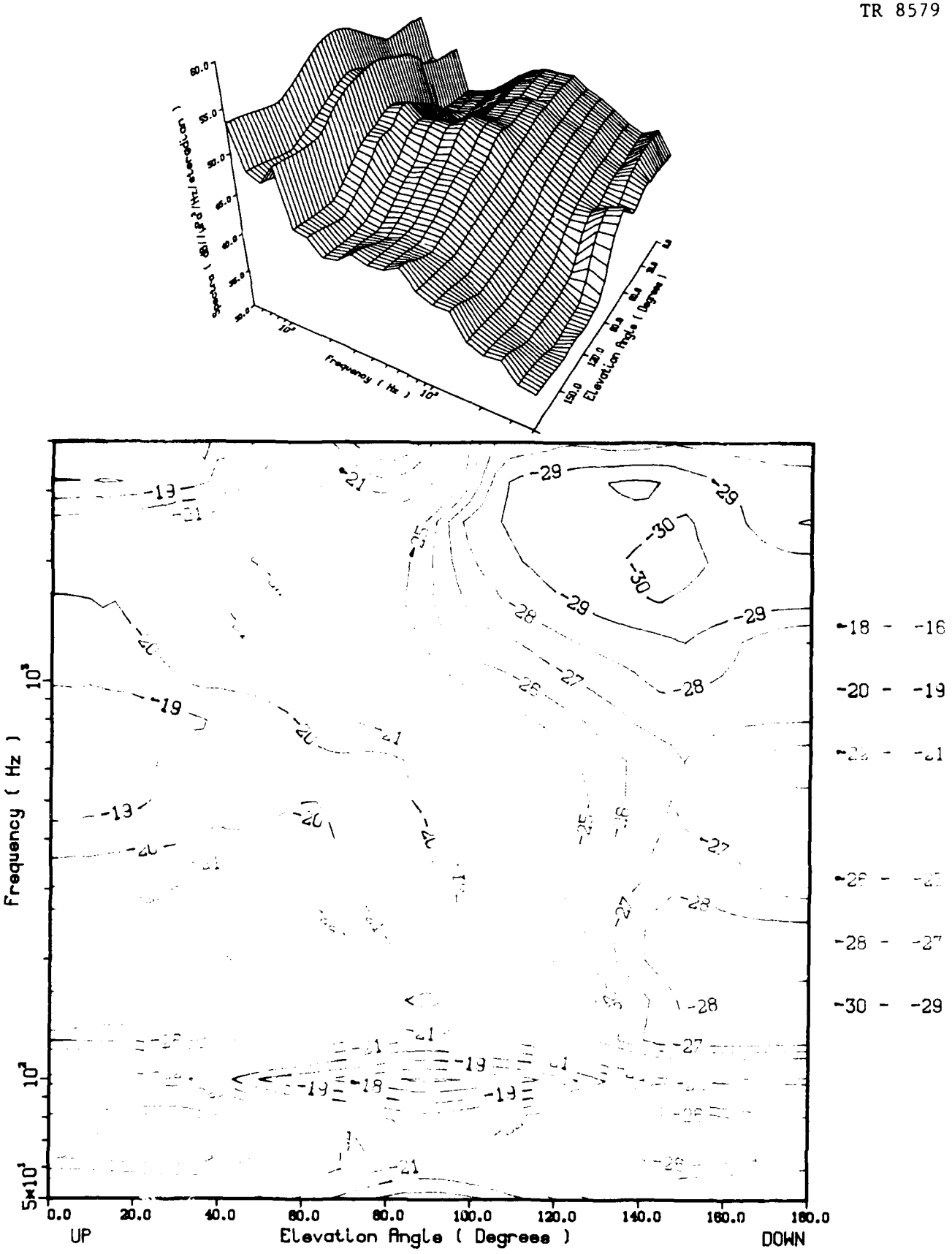

Figure 32. Corrected Directional Spectra Versus Frequency and Direction Angle for 4.37 m/s Wind Speed

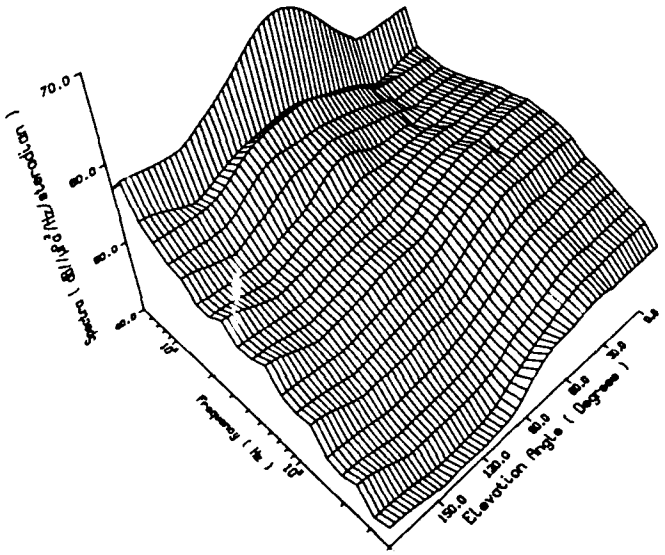

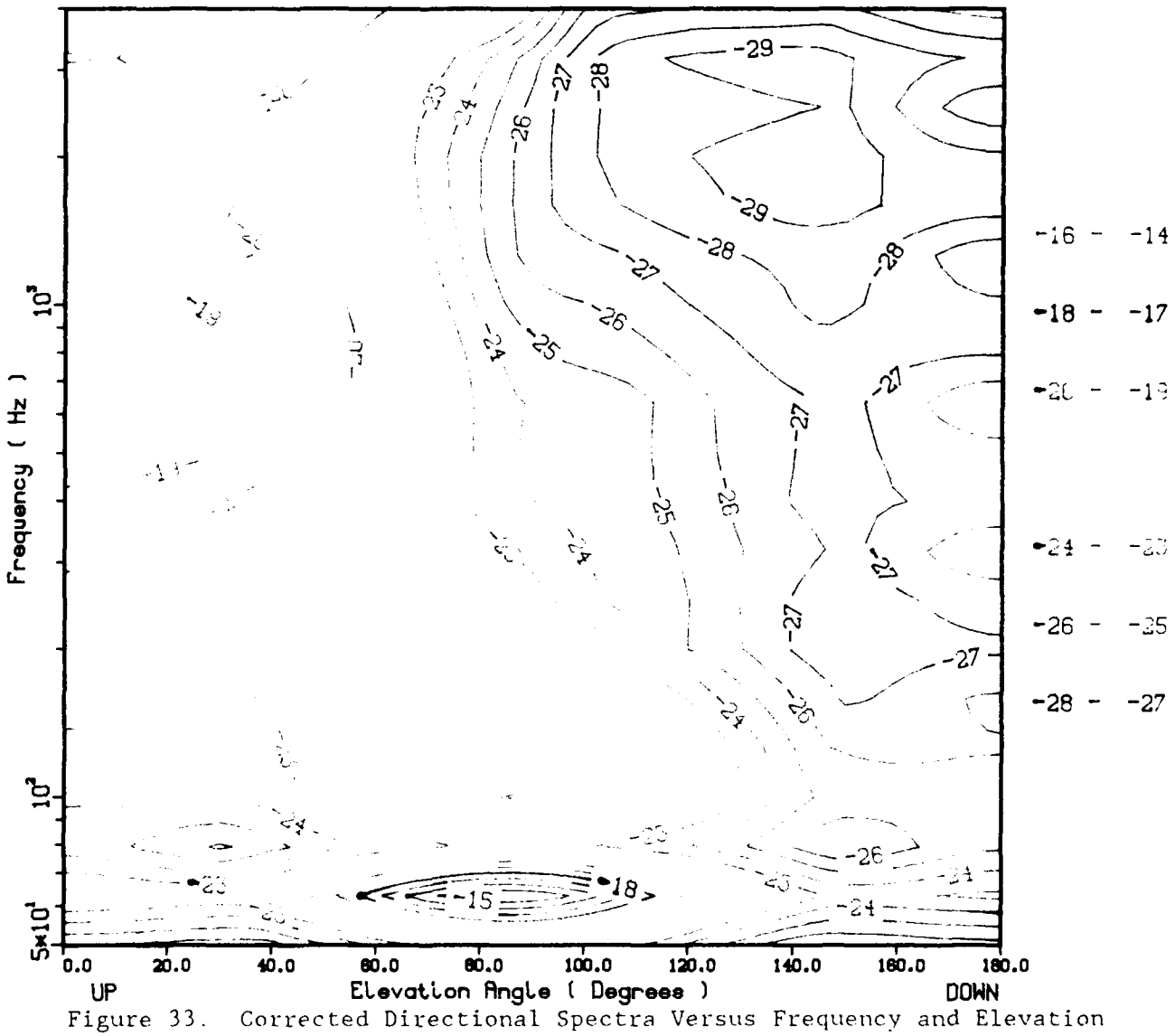

Figure 33. Corrected Directional Spectra Versus Frequency and Elevation Angle for 7.7 m/s Wind Speed

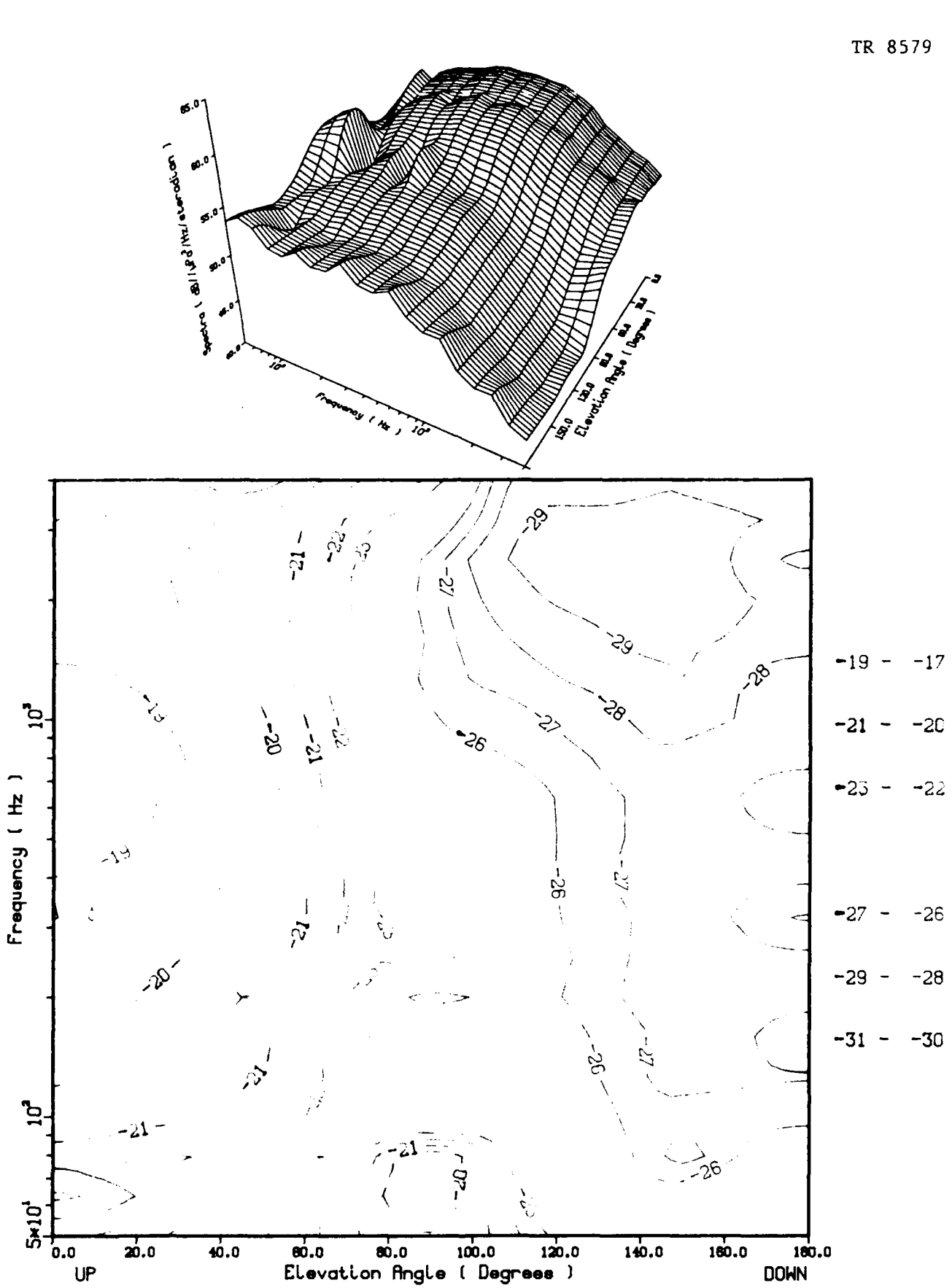

Figure 34. Corrected Directional Spectra Versus Frequency and Elevation Angle for 11.83 m/s Wind Speed

whitecapping is present the asymmetrical pattern dominates nearly the entire two decades of frequency, indicating the efficient sound sources present in the whitecapping process. Thus below 300 Hz the sea surface radiation process is quite different than it is above 300 Hz when whitecaps are not present. However, with whitecapping the mechanisms below and above 300 Hz are very similar.

Figures 35 through 38 illustrate elevation angle "cuts" of the previous three-dimensional surfaces of the corrected directional spectra for selected frequencies. Because the frequencies chosen were always near the frequency for which the hydrophone spacing was one-half wavelength, the resulting spectra is biased by the aliasing error of the array. For this reason the biased values, which are in the vicinity of 180°, have been removed. Data representing different wind speeds are overplotted in each graph. These graphs illuminate the discussions of the previous paragraph. Note in particular the significant change in the downward-propagating energy when whitecaps were present, i.e., wind speed greater than 6.5 m/s, at frequencies less than 300 Hz relative to greater than 300 Hz.

4.5 ANISOTROPIC GAIN

A primary function of hydrophone arrays is the detection and measurement of underwater acoustic radiation. A measure of the spatial gain that one achieves with this structure is found by taking the ratio of the total acoustic sound pressure level to the beamformer output calibrated to properly measure the sound pressure level of a plane wave. This ratio, for a properly designed structure, is of the order of the number of hydrophones at the frequency for which the hydrophones are spaced an acoustic one-half wavelength apart. In the present case the gain is between 8 to 9 dB, depending on the spatial weighting function used. This is the spatial gain of the system in an isotropic ambient field and is referred to as the directivity index. The directivity index is a function of both frequency and beamformer steering angle; however, it is only mildly dependent on these variables, changing by only 3 dB over the 180° steering range and an octave of frequency range. Clearly, the actual spatial gain will depend sensitively on the steered direc-

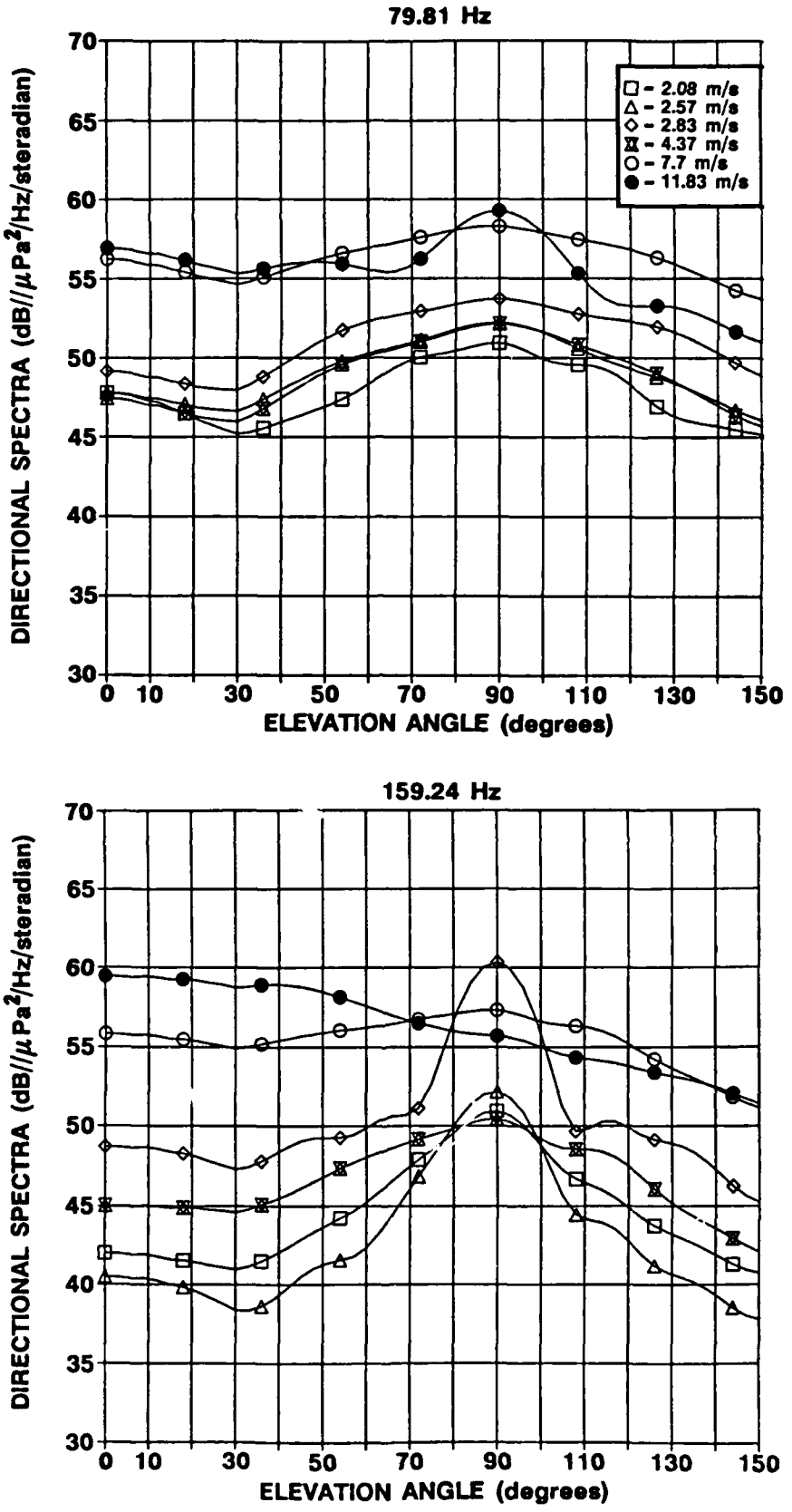

Figure 35. Corrected Directional Spectra Wind Speed Dependence at 79.81 Hz and 159.24 Hz

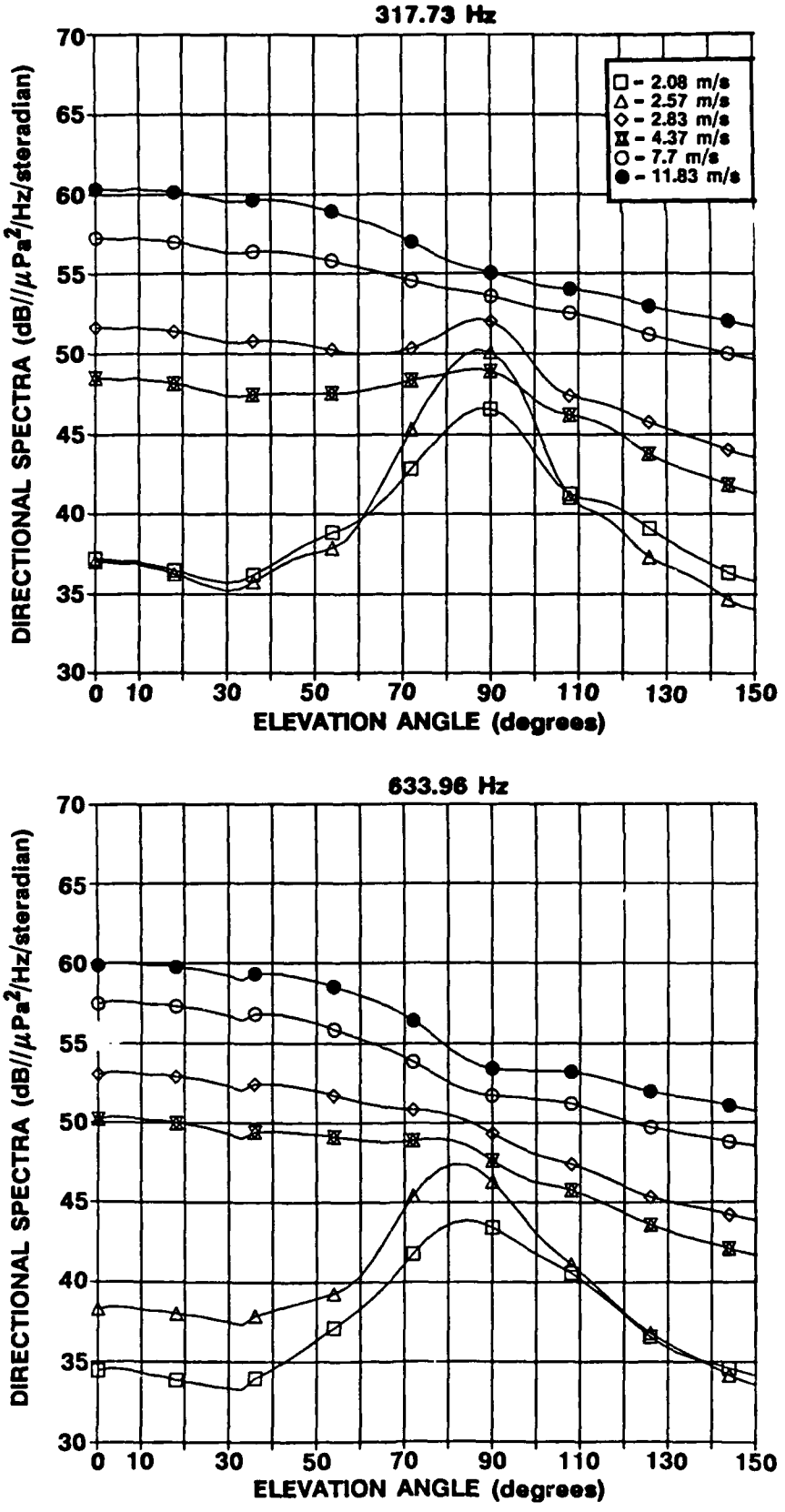

Figure 36. Corrected Directional Spectra Wind Speed Dependence at 317.73 Hz and 633.96 Hz

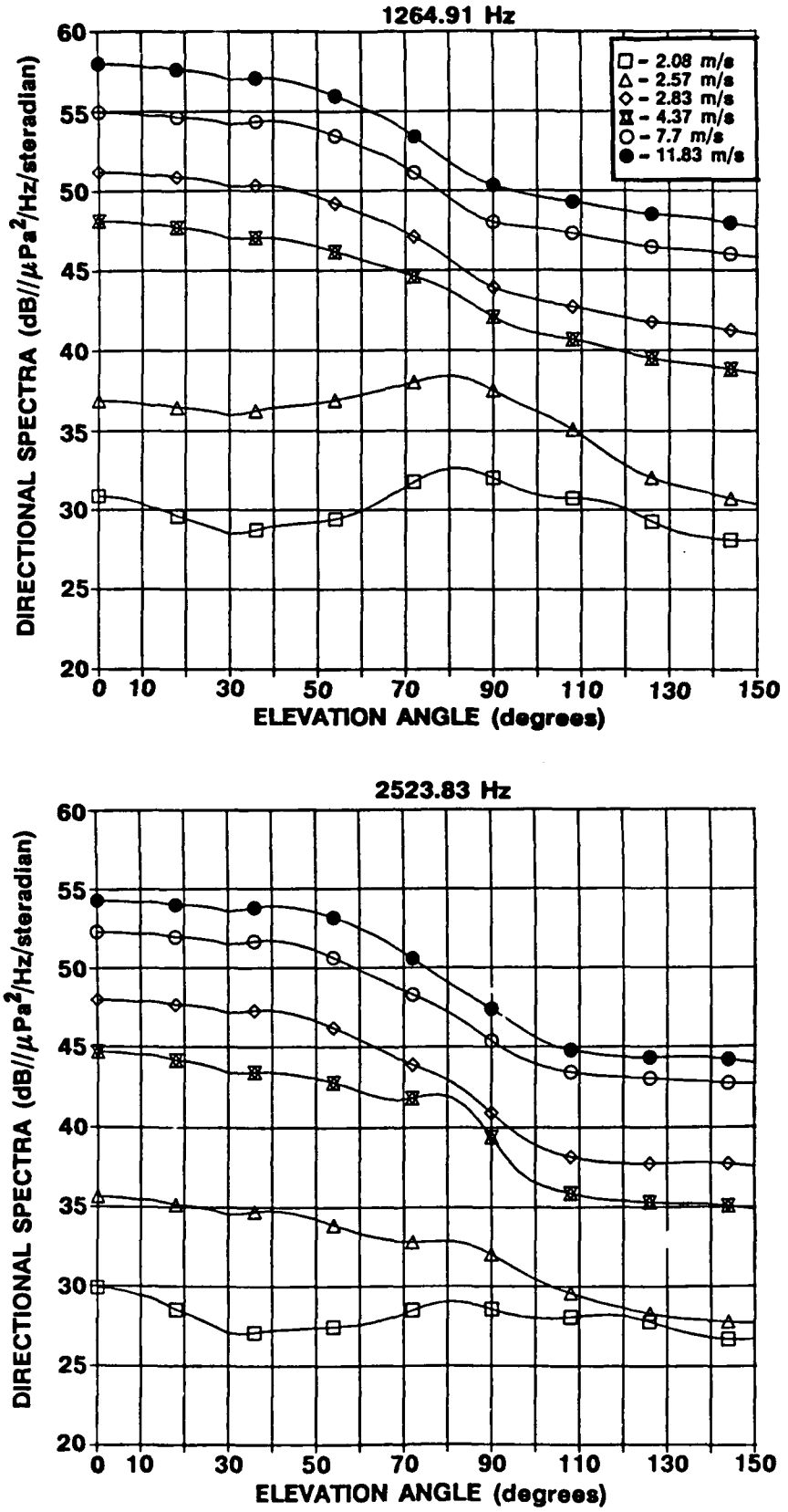

Figure 37. Corrected Directional Spectra Wind Speed Dependence at 1264.91 Hz and 2523.83 Hz

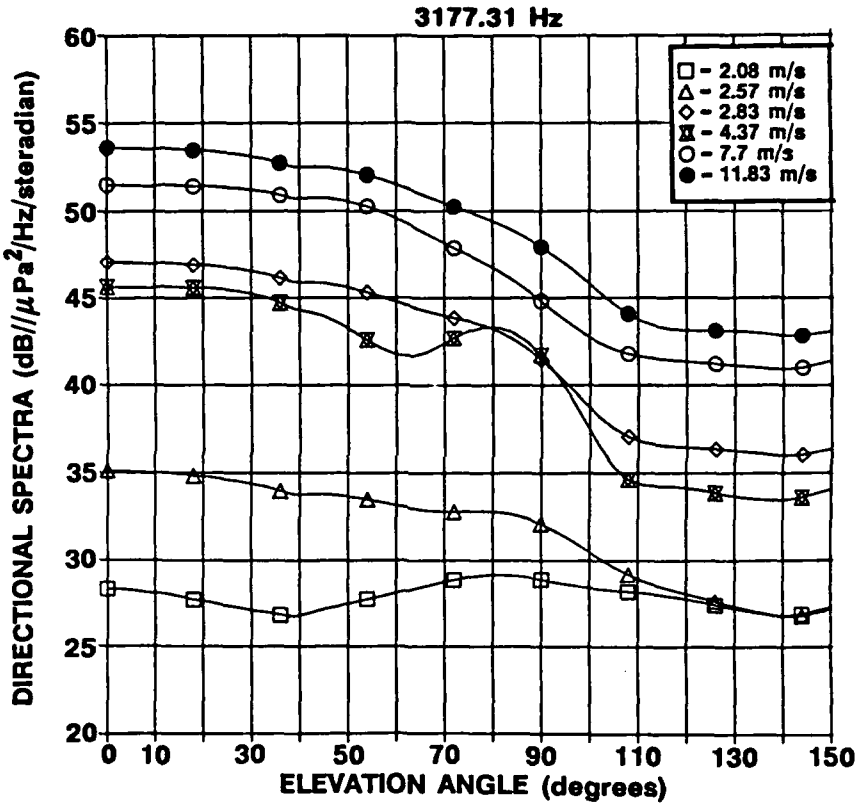

Figure 38. Corrected Directional Spectra Wind Speed Dependence at 3177.31 Hz

tion of the beamformer in an anisotropic acoustic ambient. In this section of the report we separate the spatial gain associated with the anisotropic pressure field by normalizing the measured spatial gain by the calculated directivity index at each frequency. The result of this calculation we term anisotropic gain. Such a presentation amounts to a transform of the data given to another observation space, i.e., directional spectra to anisotropic gain. The independent variables remain the same. Thus the data shown in figures 30 through 38 are shown as anisotropic gains in figures 39 through 47. The figures quantify the obvious; i.e., high spatial gains are found by steering to regions of low acoustic ambient radiation. At low wind speeds this is achieved by steering either above or below the horizontal. As the wind speed increases then, depending on the frequency, gains greater than the directivity index are observed from the horizontal direction on down to 180°. Once the wind speed becomes high enough to establish this asymmetrical pattern, then the anisotropic gain becomes relatively insensitive to further wind speed increases. The increased gain obtained by steering downward is quite significant, i.e., 5 to 6 dB over the 9 dB directivity index. Thus the spatial gain of an 8-hydrophone array exhibits the gain of a 25-hydrophone array.

Start Time	: 10/24/88 03:17	Wind Direction (deg)	:270
Array Depth (m)	: 139.1	Tilt Sensor #1 Angle (deg)	:0.7
Wind Speed (m/s)	: 2.06	Tilt Sensor #2 Angle (deg)	:0.6
Location	: HAUL DOWN	Anisotropic Gain (dB)	
Spatial weighting:	Taylor	Plot pre-whitening	:n

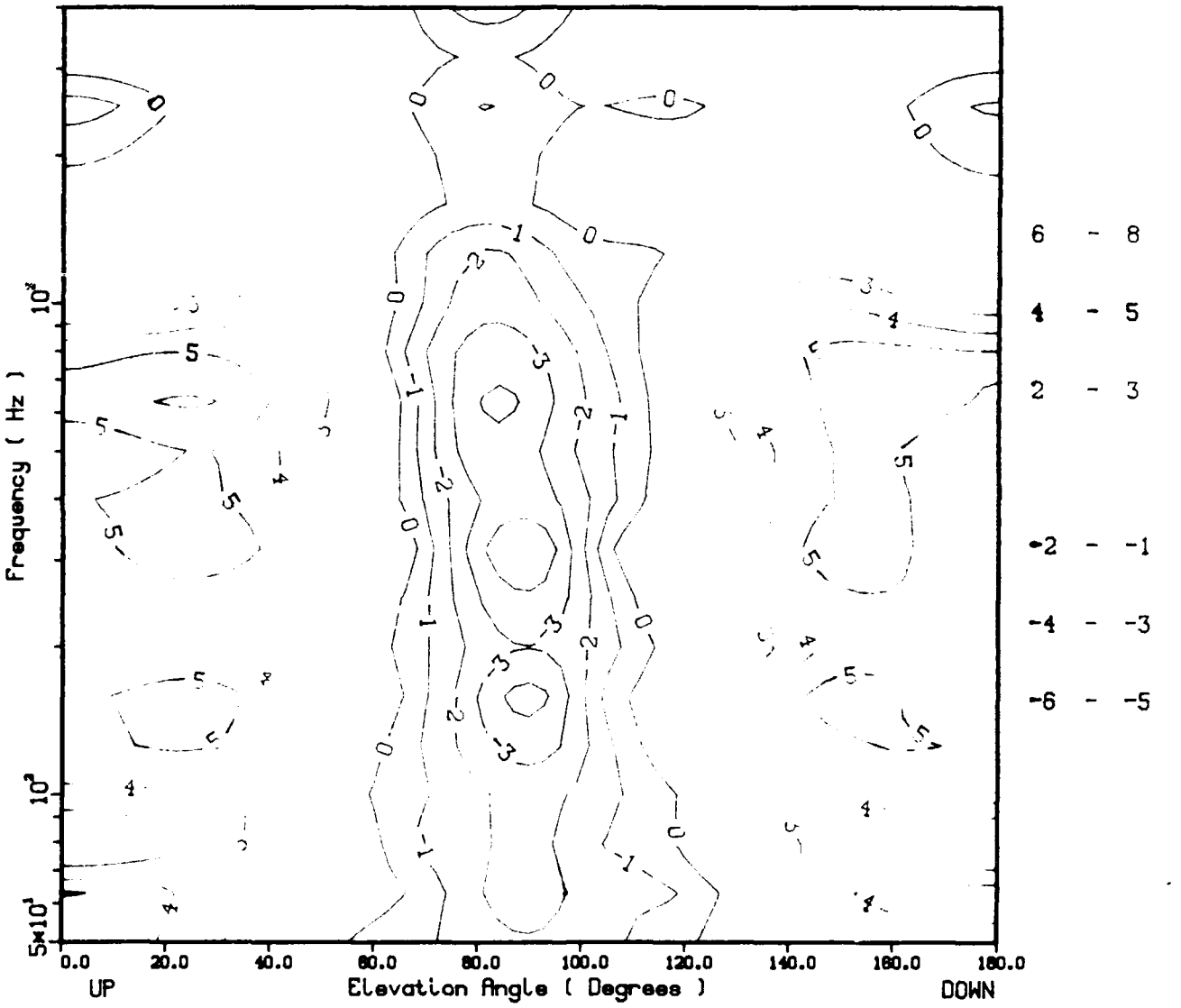

Figure 39 Corrected Anisotropic Gain Versus Frequency and Elevation Angle for 2.06 m/s Wind Speed

Start Time	: 09/27/88 22:44	Wind Direction (deg)	:36.0
Array Depth (m)	: 140.0	Tilt Sensor #1 Angle (deg)	:0.8
Wind Speed (m/s)	: 2.83	Tilt Sensor #2 Angle (deg)	:0.7
Location	: HAUL DOWN	Anisotropic Gain (dB)	
Spatial weighting	: Taylor	Plot pre-whitening	:n

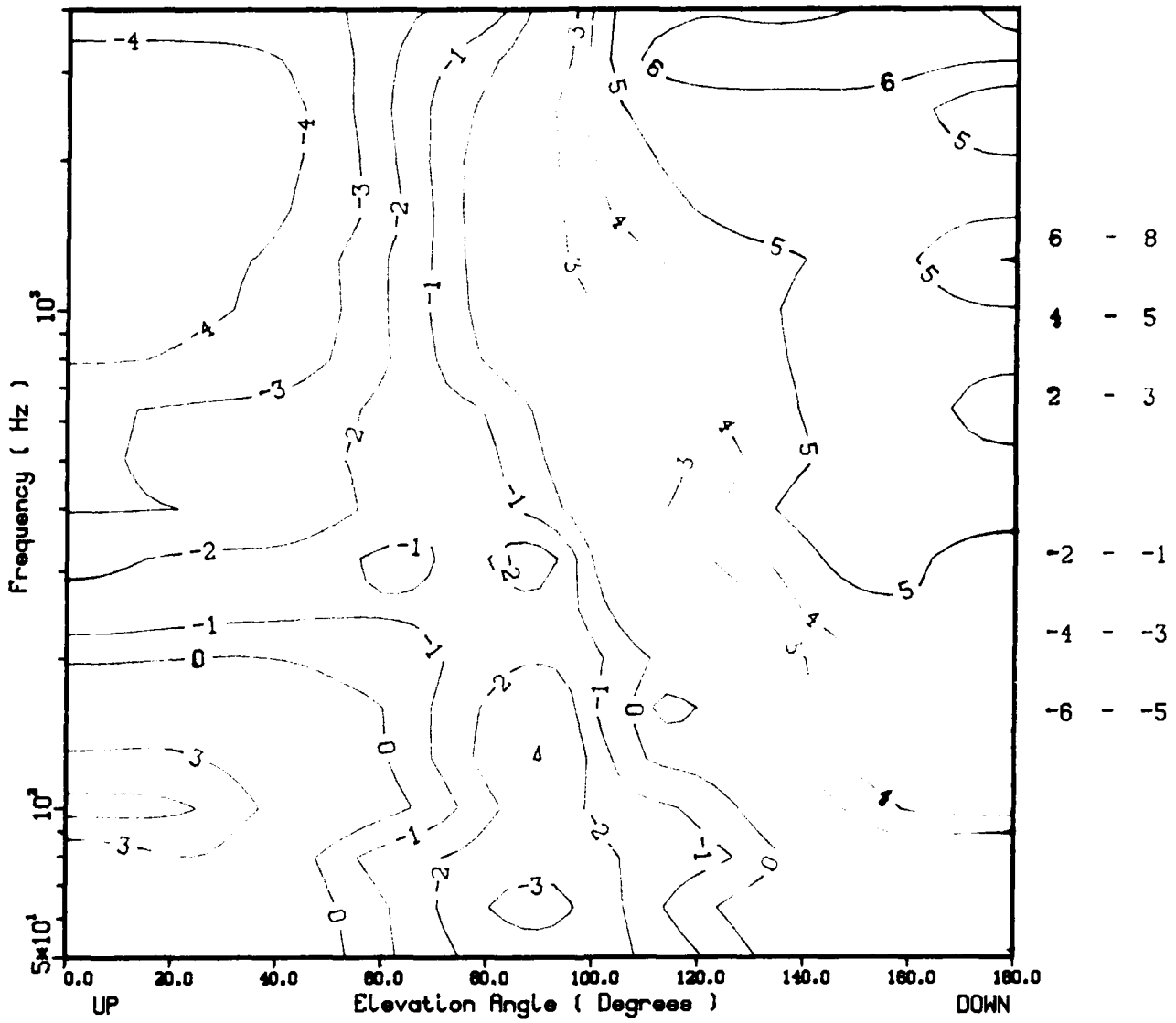

Figure 40. Corrected Anisotropic Gain Versus Frequency and Elevation Angle for 2.83 m/s Wind Speed

Start Time	: 09/29/88 23:06	Wind Direction (deg)	:50
Array Depth (m)	: 142.8	Tilt Sensor #1 Angle (deg)	:0.0
Wind Speed (m/s)	: 4.37	Tilt Sensor #2 Angle (deg)	:1.1
Location	: HAUL DOWN	Anisotropic Gain (dB)	
Spatial weighting	: Taylor	Plot pre-whitening	:n

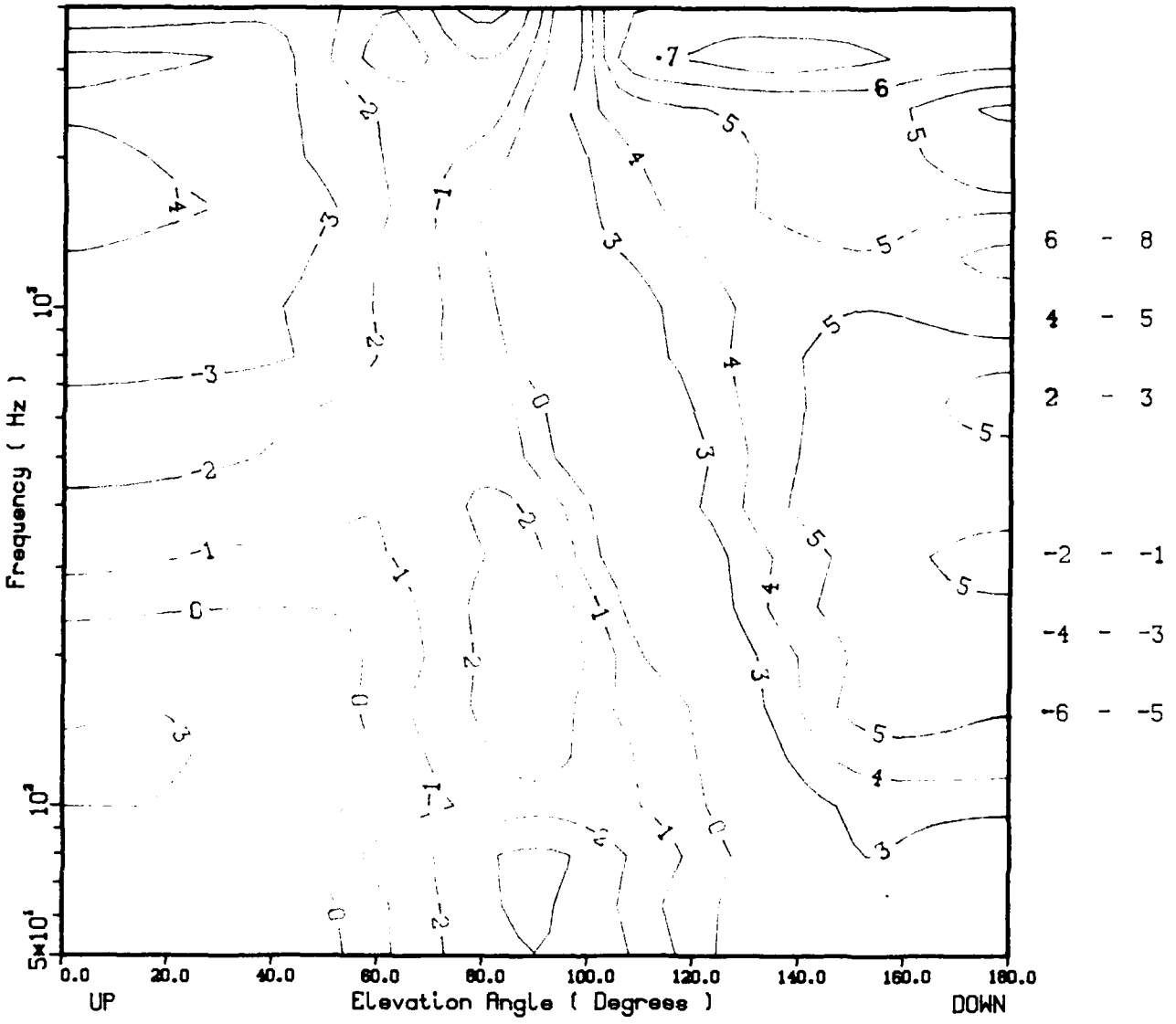

Figure 41. Corrected Anisotropic Gain Versus Frequency and Elevation Angle for 4.37 m/s Wind Speed

Start Time	: 09/09/88 11:30	Wind Direction (deg)	:125
Array Depth (m)	: 156.2	Tilt Sensor #1 Angle (deg)	:0.8
Wind Speed (m/s)	: 7.7	Tilt Sensor #2 Angle (deg)	:0.8
Location	: HAUL DOWN	Anisotropic Gain (dB)	
Spatial weighting	: Taylor	Plot pre-whitening	:n

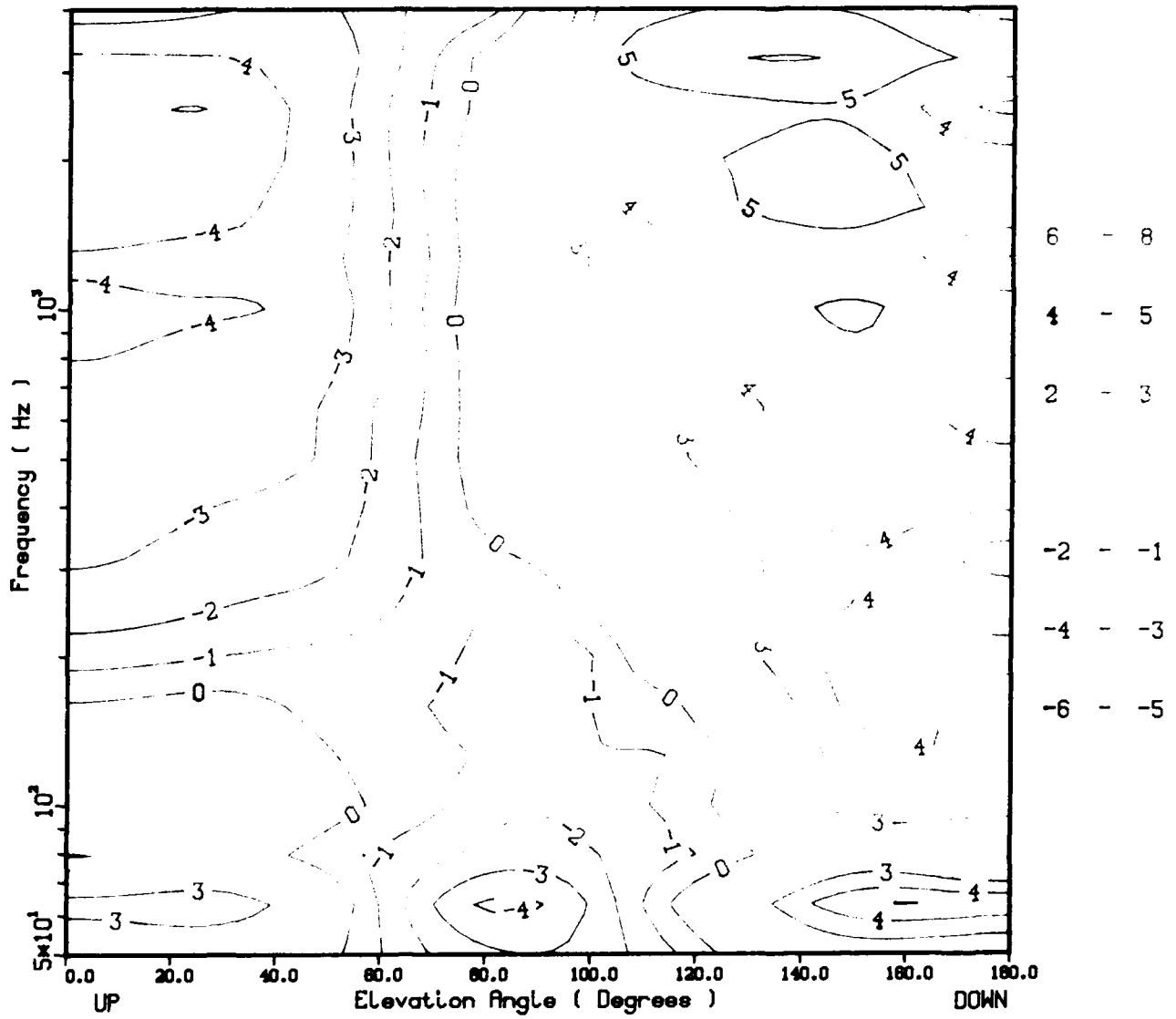

Figure 42. Corrected Anisotropic Gain Versus Frequency and Elevation Angle for 7.7 m/s Wind Speed

Reverse Blank

Start Time	: 10/16/88 01:53	Wind Direction (deg)	:40
Array Depth (m)	: 139.6	Tilt Sensor #1 Angle (deg)	:2.3
Wind Speed (m/s)	: 11.83	Tilt Sensor #2 Angle (deg)	:2.4
Location	: HAUL DOWN	Anisotropic Gain (dB)	
Spatial weighting	: Taylor	Plot pre-whitening	:n

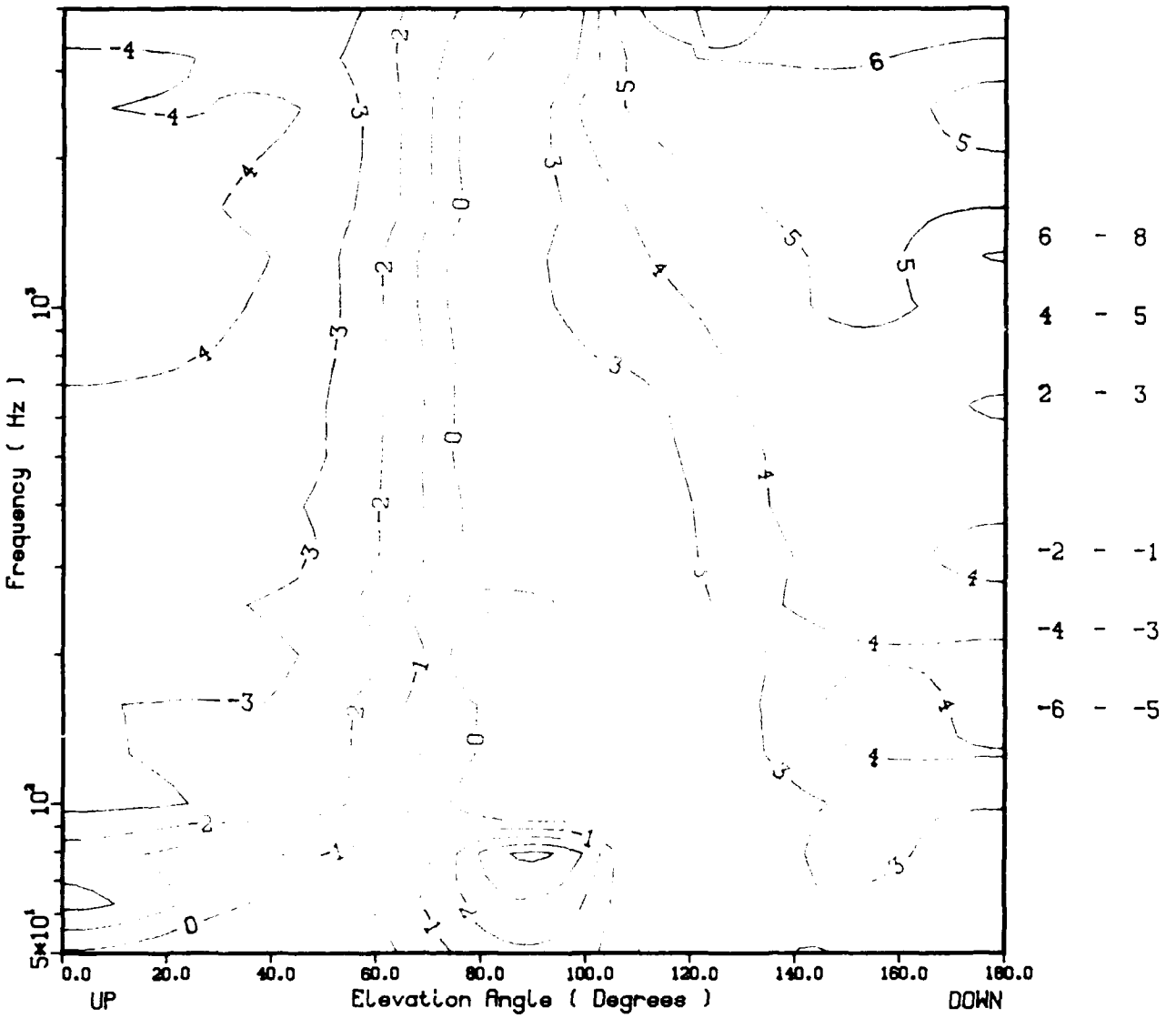

Figure 43. Corrected Anisotropic Gain Versus Frequency and Elevation Angle for 11.83 m/s Wind Speed

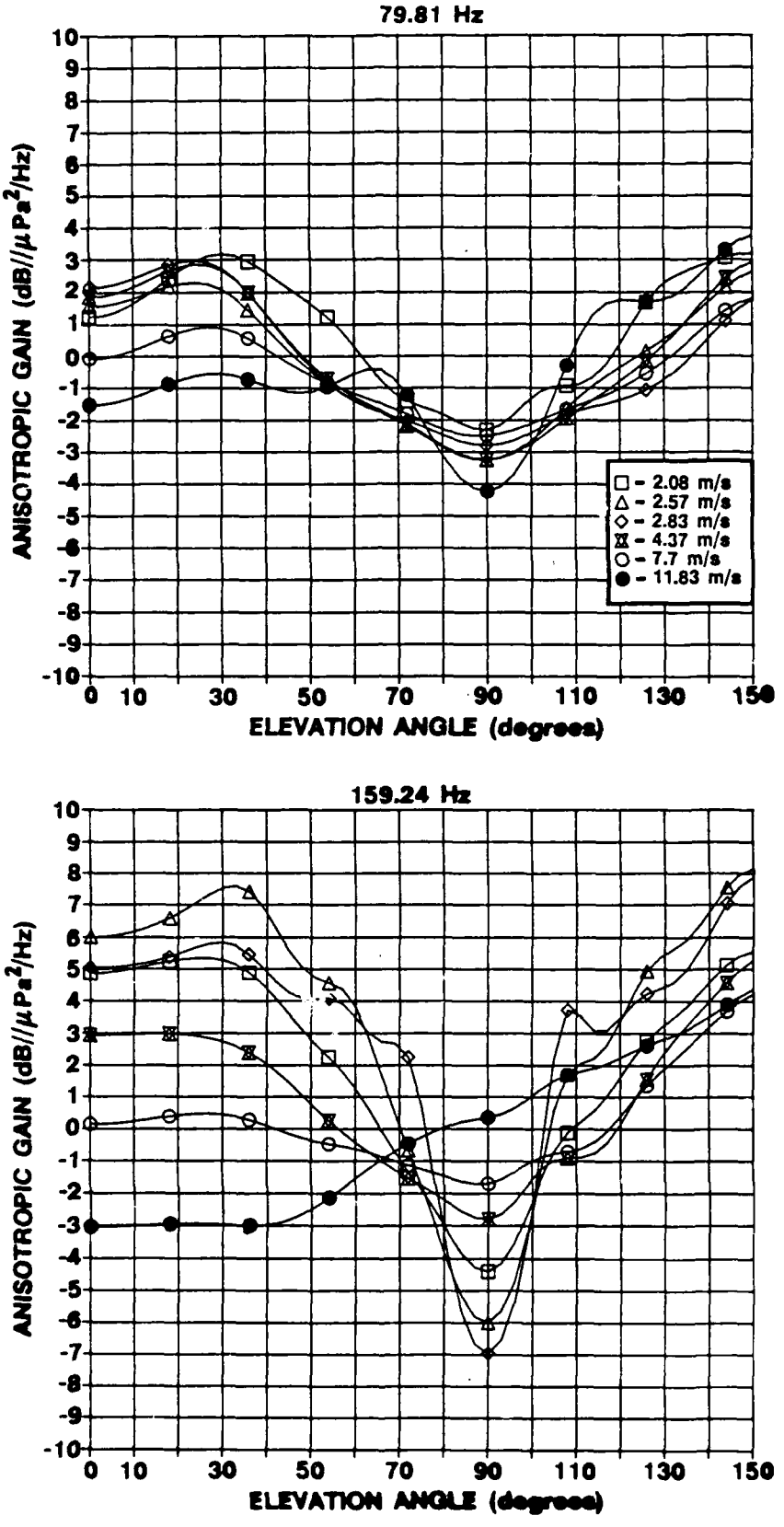

Figure 44. Corrected Anisotropic Gain Wind Speed Dependence at 79.81 Hz and 159.24 Hz

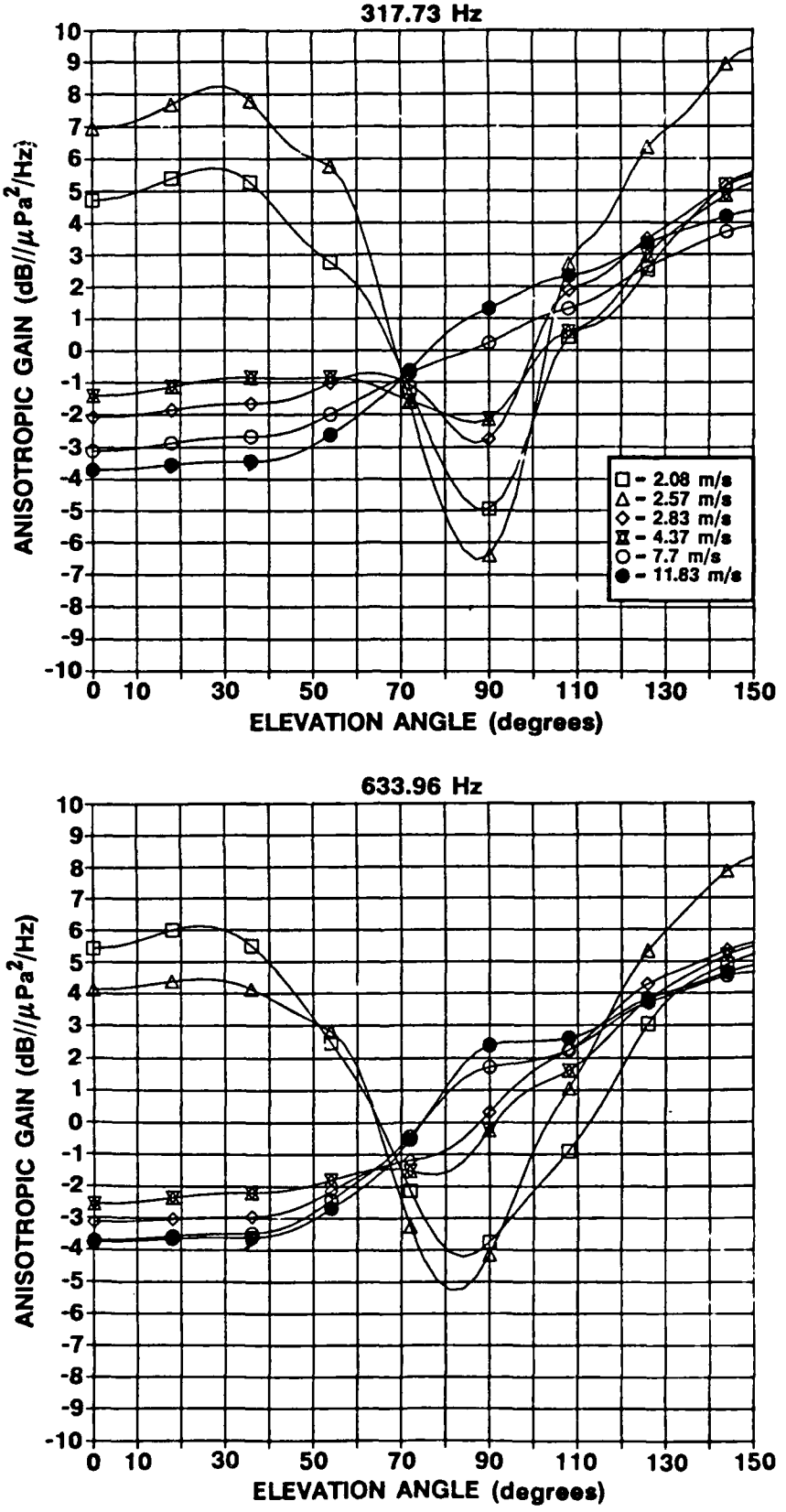

Figure 45. Corrected Anisotropic Gain Wind Speed Dependence at 317.73 Hz and 633.96 Hz

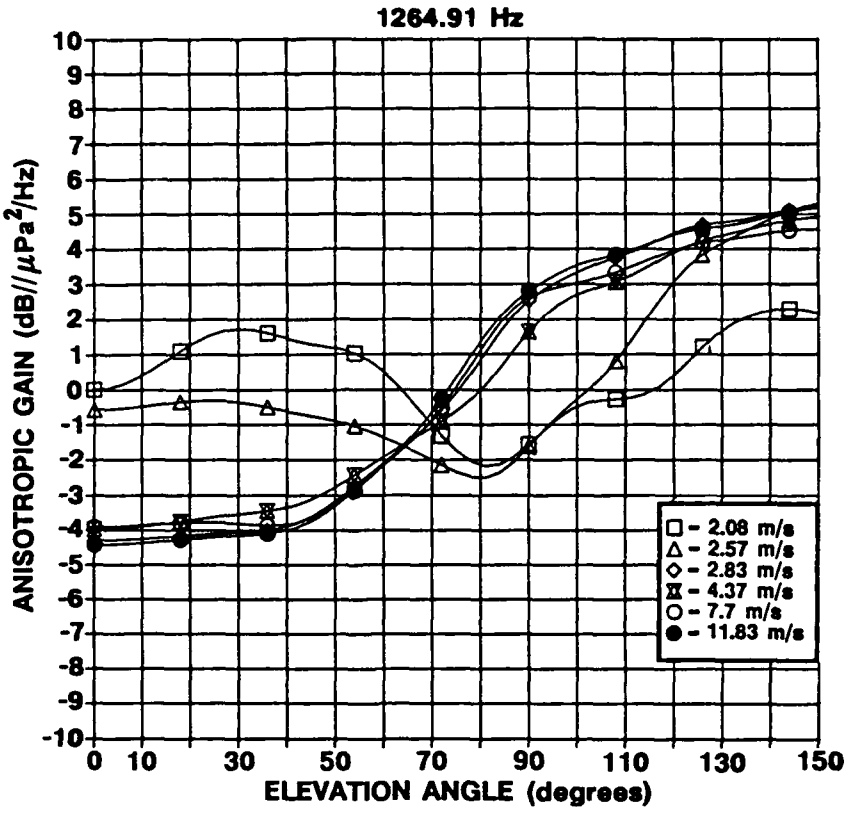

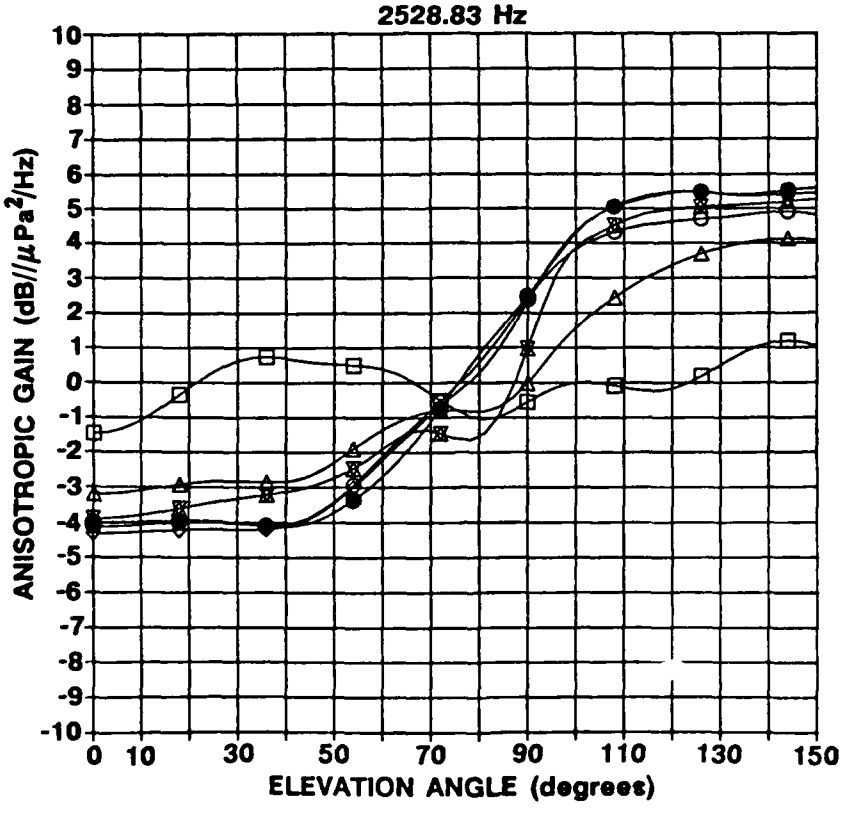

Figure 46. Corrected Anisotropic Gain Wind Speed Dependence at 1264.91 Hz and 2523.83 Hz

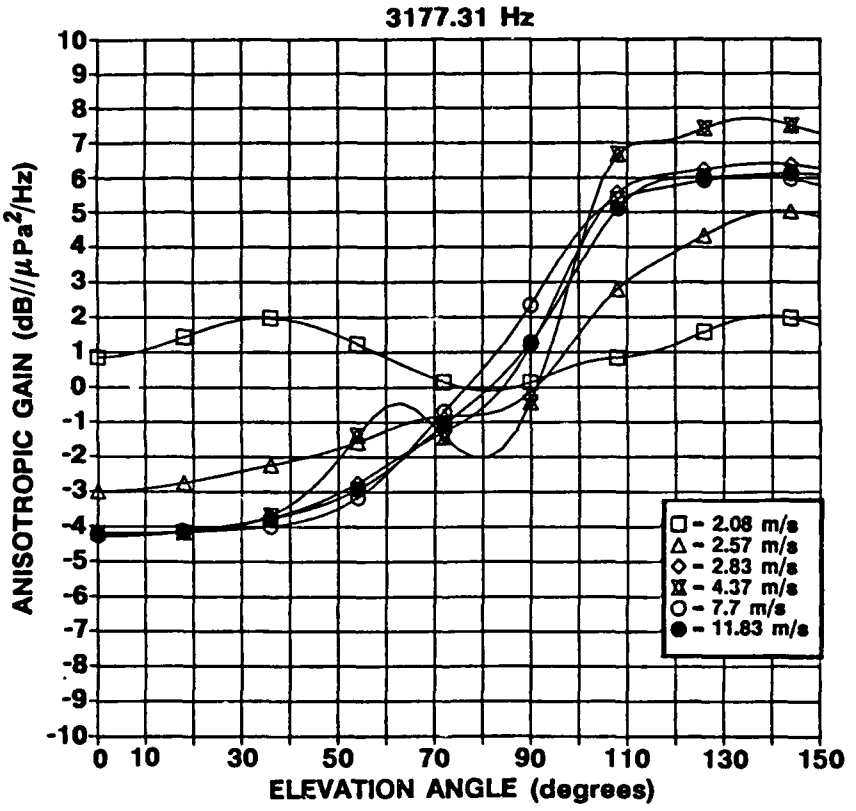

Figure 47. Corrected Anisotropic Gain Wind Speed Dependence at 3177.31 Hz

5.0 SUMMARY

This report documents the data processing techniques and the results of the initial deployment of a wideband (40 to 4000 Hz) vertical acoustic antenna system in The Tongue of the Ocean, The Bahamas, at a site adjacent to the Andros Island eastern escarpment. The instrumentation system consisted of seven octavely nested four-wavelength acoustic antennas covering the above frequency range and a VCR-based subsurface recording system that carried out a programmed sequence of recordings. The purpose of the experiment was the initial field test of a deployable acoustic monitoring system (DAMS). The success of the experiment made available a data set that allowed the examination of the vertical spatial structure of the acoustic ambient of the location. While there were aspects of the data unique to the location, the bulk of the information appears to apply to the more-generic problem of characterizing the directional spectra resulting from a sea surface sound source structure.

The two-month experiment period of September and October 1988 made available 25 data sets that adequately covered the "no whitecaps present" case but only sparsely covered the "whitecaps present" case. The measured total sound pressure levels compared favorably with previous experience, indicating that a unity value of the surface friction velocity nondimensionalized by the minimum phase velocity of the surface capillary-gravity wave field marked a change in the acoustic ambient pressure field caused by incipient whitecapping. The power law fit to the "no whitecaps present" case was on the average only 1.7 relative to the 3.0 reported in reference 19. However, the power law exponent fit to the directional spectra, in the direction of the surface, above 300 Hz varied from 2.8 to 3.1. Upward-propagating energy had exponents that varied from 1 to 2, depending on the elevation angle and frequency. Thus even at frequencies above 300 Hz the sea surface sound was not the only source of acoustic energy present. Below 300 Hz the power law exponent was always less than 1. There appeared to be two reasons for this lack of wind speed dependence. First, this frequency range regularly contained narrowband acoustic energy, presumably the result of industrial and boating activity in the area. Underlying these randomly occurring events was a spatially diffuse acoustic background with a broad maxima in the horizontal direction that exhibited

little wind speed dependence. Second, prior to the onset of whitecapping there was little to no wind speed dependence in the data. Once whitecapping occurred, the levels jumped noticeably. This appears to indicate a difference in the acoustic sea surface source mechanism above and below 300 Hz with no whitecaps present. With whitecaps present, the acoustic source mechanism appeared uniform over the entire two frequency decades of the measurement, exhibiting the usual broad maxima near 500 Hz, which has been attributed to spray impact on the surface.[23]

The measured vertical directional spectra display two patterns in an elevation angle-frequency space. The first pattern consists of a ridge of energy at or near the horizontal direction which drops off, i.e., less energy, monotonically and nearly symmetrically in either the up or down direction. The entire pattern is inversely proportional to frequency. The second pattern is quite nonsymmetrical about the horizontal with a broad maxima in the direction of downward-propagating energy and a minima in the direction of upward-propagating energy. The latter is the familiar pattern associated with a surface layer of independently radiating dipoles. At the lowest wind speeds of about 2 m/s the first pattern extends over the entire frequency range. As the wind speed increases, the second pattern dominates above 300 Hz and the first pattern dominates below 300 Hz. This dual pattern continues until whitecapping commences, at which time the second pattern dominates the entire two frequency decades of the measurement. At low wind speeds, when the first pattern dominates the entire frequency range, the ridge of energy above 500 Hz is centered at 8° above the horizontal. This ridge extends to 4000 Hz. There are two explanations for this energy. First, this is the direction associated with radiation from the top of the escarpment. The frequency spectral shape shows increasing levels from 1500 to 4000 Hz, which is consistent with "snapping shrimp" radiation. This explanation indicates a local sound source. However, it is known that the Tongue of the Ocean acts as waveguide that efficiently propagates energy via a bottom/surface interacting path over a very narrow angular window. Predictions of the center of this elevation angle indicate a narrow peak at about 7° from the horizontal. This has been verified in the data repeatedly by the reception of sonar pulses propagated from more than 40 km away and arriving in the center of the ridge being discussed.

This explanation indicates that long-distance sound sources throughout the "tongue" would communicate with the measurement on this ridge. The actual explanation for this ridge of acoustic energy could be either or both explanations.

The basic measurement of the experiment was the cross-spectral density matrix for each of the seven vertical hydrophone arrays. An eigenvector decomposition of these matrices was performed. There are two basic results of the decomposition. First, the eigenvalues, sorted by magnitude, indicate a uniform distribution of magnitudes except when an independently occurring plane wave is present in the measurement. Second, the eigenbeams, when plotted as a three-dimensional surface versus elevation angle and eigenvalue number, form two patterns consistent with the two directional spectra patterns discussed above. First is a pattern showing a diffuse source peaking in or near the horizontal direction and uniformly decreasing in both the up and down directions. Each eigenbeam contains two peaks, one up and one down. A possible interpretation of this pattern is that the upward- and downward-propagating energy occurs in spatially coherent pairs. The second pattern indicates a spatially diffuse source structure with a maxima for downward-propagating energy and a minima with upward-propagating energy. The uniform distribution of eigenvalues was used to remove contaminating plane waves by adjusting the level of the eigenvalue containing the plane wave to be consistent with the uniform distribution of eigenvalues that would exist in the absence of the plane wave.

Three-dimensional surfaces of the anisotropic gain were plotted as a function of frequency and elevation angle with wind speed as a parameter. Anisotropic gain is defined here as the spatial gain of the vertical hydrophone array relative to the gain of the same array in an isotropic noise field. The results quantified the obvious; i.e., beamformer gains steered in the downward direction can realize significant improvements over the directivity index of that array. In the present case 14 to 15 dB of spatial gain was measured for an array having a 9 dB directivity index. This result in the downward direction was relatively independent of the wind speed.

6.0 REFERENCES

1. H.O. Berteaux, Buoy Engineering, A Wiley-Interscience Publication, John Wiley & Sons, New York, NY, 1976.

2. R.B. Blackman and J.W. Tukey, The Measurement of Power Spectra, Dover Publications, New York, NY, 1958.

3. R.L. Streit, "A Discussion of Taylor Weighting for Continuous Apertures," NUSC Technical Memorandum 851004, Naval Underwater Systems Center, New London, CT, 4 January 1985.

4. T.T. Taylor, "Design of Line-Source Antennas for Narrow Beamwidth and Low Side Lobes," IRE Transactions on Antennas and Propagation, vol. AP-3, January 1955, pp. 16-28.

5. L.R. LeBlanc, "Angular-Spectral Decomposition Beamforming for Acoustic Arrays," IEEE Journal of Oceanic Engineering, vol. OE-9, 1984, pp. 31-39.

6. D.J. Kewley, "Using Eigenvalue Analysis To Identify Interference in Ambient Sea Noise Vertical Directionality Measurements," Journal of the Acoustical Society of America, vol. 75, no. 3, March 1984.

7. W.H. Press, B.P. Flannery, S.A. Teukolsky, and W.T. Vetterling, Numerical Recipes, the Art of Computing, Cambridge University Press, Cambridge, MA, 1986.

8. R.W. Hamming, Numerical Methods for Scientists and Engineers, second edition, Dover Publications, Dover, DE, 1986.

9. J. Stone, "Problems Associated With the Measurement of Ambient Noise Directivity by Means of Linear Additive Arrays," Journal of the Acoustical Society of America, vol. 34, no. 3, March 1962.

10. M.W. Anderson and R.L. Tittle, "Analysis of an Integral Equation Arising From the Investigation of Vertical Directivity of Sea Noise," Journal of the Acoustical Society of America, vol. 45, no. 5, 1969.

11. N. Yen, "Analytical Expansion Technique for Ambient Noise Directionality Determination," Journal of the Acoustical Society of America, vol. 66, no. 2, August 1979.

12. A.H. Nuttall, Estimation of Noise Directionality Spectrum, NUSC Technical Report 4345, Naval Underwater Systems Center, New London, CT, September 1972.

13. G.R. Fox, "Ambient-Noise Directivity Measurements," Journal of the Acoustical Society of America, vol. 36, no. 8, 1964, pp. 1537-1540.

14. E.H. Axelrod, B.A. Schoomer, and W.A. Von Winkle, "Vertical Directionality of Ambient Noise in the Deep Ocean at a Site Near Bermuda," Journal of the Acoustical Society of America, vol. 37, no. 1, 1965, pp. 77-83.

15. V.C. Anderson, "Variation of the Vertical Directionality of Noise With Depth in the North Pacific," Journal of the Acoustical Society of America, vol. 66, no. 5, 1979, pp. 1446-1452.

16. S.C. Wales and O.I. Diachok, "Ambient Noise Vertical Directionality in the Northwest Atlantic," Journal of the Acoustical Society of America, vol. 70, no. 2, 1981, pp. 577-582.

17. Environmental Atlas of the Tongue of the Ocean, Special Publication SP-94, Naval Oceanographic Office, Bay St. Louis, MS, 1967.

18. A.B. Caron and E.S. Sheffield, "AUTEC Ambient Noise Analysis, Descriptions of Data and Analysis," NUSC informal memorandum, Naval Underwater Systems Center, Newport, RI, 13 July 1988.

19. B.R. Kerman, "Underwater Sound Generation by Breaking Waves," Journal of the Acoustical Society of America, vol. 75, 1984, p. 148.

20. V.M. Albers, Underwater Acoustics Handbook, The Pennsylvania State University Press, University Park, PA, 1960.

21. R.M. Kennedy and T.K. Szlyk, "A multipath calculation of surface-generated underwater acoustic vertical directivity," Journal of the Acoustical Society of America, vol. 86, no. 5, November 1989, pp. 1920-1927.

22. R.M. Kennedy, T.K. Szlyk, and S.M. Wentworth, Wind Speed Dependence of Acoustic Ambient Vertical Directional Spectra at High Frequency, NUSC Technical Report 8537, Naval Underwater Systems Center, Newport, RI, August 1989.

23. D. Ross, Mechanics of Underwater Noise, Pergamon Press, Elmsford, NY, 1976.

INITIAL DISTRIBUTION LIST

Addressee	Number of Copies
COMNAVSEASYSCOM (Code 63D) CDR E. Graham	1
(PMS393A) CDR S. Logue	1
(PMS393N) J.H. Fuchs	1
COMNAVAIRSYSCOM (Code 421) T. Ramirez	1
CNA	1
DTIC	12
DTRC (Code 1925) G.M. Jebsen	1
(Code 0100) R.E. Metrey	1
NAVPGSCOL H. Medwin	1
NOAA/Miami H. Bezdek	1
NOSC J. Rohn	1
OCNR (Code 1121GS) O. Brandt	1
(Code 1122ML) M. Briscoe	1
(Code 1125) L.G. Johnson	1
(Code 1125AR) R.F. Obrachta	1
(Code 11250A) M. Orr	1
Applied Measurement Systems, Inc., Hollywood, FL; B.L. Douglass	1
C&N Technology, Inc.; J. Mingrone	1
General Electric Co., Andros Island, Bahamas; L.A. Lindquist	1
GRD Associates, Delray Beach, FL; G.R. Desmarais	1
MPL, Scripps Institution of Oceanography, La Jolla, CA; W. Hodgekist	1
Planning Systems, Inc., New London, CT; W.M. Leen	1
Sawgrass Technical Services, Inc., Davie, FL; T.V. Goodnow	1